Title

The Design and Fabrication of Non-Planar and Solid State Lithium Ion Batteries

Author

Fox, Maggie Taylor

Publication Date

2023

UNIVERSITY OF CALIFORNIA

Los Angeles

The Design and Fabrication of Non-Planar and Solid State Lithium Ion Batteries

A dissertation submitted in partial satisfaction of the
requirements for the degree Doctor of Philosophy
in Materials Science and Engineering

by

Maggie Taylor Fox

2023

ABSTRACT OF THE DISSERTATION

The Design and Fabrication of Non-Planar and Solid State Lithium Ion Batteries

by

Maggie Taylor Fox
Doctor of Philosophy in Materials Science and Engineering
University of California, Los Angeles, 2023
Professor Bruce S. Dunn, Chair

With the continual growth of the Internet of Things and miniaturization of consumer electronics, there is a need to improve the power sources for these technological advancements. Batteries represent a potential power source because of their ability to continuously provide power, however there is a current bottleneck in improving their device performance due to their traditional planar designs. This limitation highlights a shift towards utilizing a nonplanar electrode architecture to improve both energy and power density without sacrificing the improvement of one parameter at the expense of the other. There are several factors to consider when utilizing a nonplanar electrode design including the method of fabrication, microscale considerations (i.e., pore size distribution and tortuosity), and macroscale considerations (i.e., aspect ratio, feature sizes, and distribution of structures). In addition to the constraints on performance with the current electrode design, there are also safety concerns when it comes to other aspects of the battery such as the use of liquid electrolyte.

To address these concerns, this dissertation explores two different fabrication methods designed to create nonplanar 3D architectures. The additive manufacturing technique, Direct Ink Writing, will be used to print lattice designs and verify the effect of some of the macroscale architecture considerations. Building blocks of these structures will also be characterized to identify potential limitations in the electrode design and fabrication process. The other fabrication method is sol-gel processing to create a 3D aperiodic sponge architecture, that can be infiltrated with a conducting medium to form a pseudo-solid cathode. Key synthesis parameters in developing an optimized microstructure for lithium intercalation are identified. Both of these electrodes will be utilized in combination with an ionogel pseudo-solid electrolyte to create 2.5D pseudo-solid lithium ion batteries. The outcome of this research will be to highlight new avenues for non-planar and solid state battery development.

The dissertation of Maggie Taylor Fox is approved.

Aaswath Pattabhi Raman

Yuzhang Li

Ali Mosleh

Bruce S. Dunn, Committee Chair

University of California, Los Angeles

2023

To my family and friends.

Thank you for always believing in me.

“I was taught that the way of progress is neither swift nor easy.”

Marie Skłodowska-Curie

Table of Contents

List of Figures

Chapter 1 Figures

Chapter 2 Figures

<u>Chapter 3 Figures</u>

Chapter 4 Figures

Chapter 5 Figures

List of Tables

Chapter 3 Tables

Chapter 4 Tables

Chapter 5 Tables

Acknowledgments

In graduate school I have grown a lot as a researcher and as a person, I owe a lot of that to my advisor Dr. Bruce Dunn. As an advisor, mentor, sponsor and advocate the number of opportunities to grow and learn that he's afforded to me have been exponential. I can only hope that I will have a fraction of the impact on others throughout my own career that Dr. Dunn has had in his. I know that it's because of all that I've learned throughout my Ph.D. that I have the tools and the courage to pursue the next phase of my career. I am forever grateful to have had him as an advisor.

I also want to take a moment to acknowledge my collaborators both outside of and at UCLA. At Lawrence Livermore National Lab, Dr. Marissa Wood and Dr. Marcus Worsley have been amazing collaborators, I'm glad to have worked with you both. At UCLA, to Dr. Sarah Tolbert, Dr. Laurent Pilon, and Dr. Y. Morris Wang and their groups I have learned a great deal from all of you spanning a variety of different areas and I am grateful that you shared your expertise with me. To my committee Dr. Aaswath Raman, Dr. Yuzhang Li, and Dr. Ali Mosleh, I want to thank you all for your intellectual comments and your constructive criticism.

To my lab mates, you have made day-to-day life in the lab enjoyable and each of you has made an impact on me in different ways. To those that have since graduated: Dr. Chun-Han (Matt) Lai, Dr. Christopher Choi, Dr. Danielle Butts, Dr. Grace Whang, Dr. Patricia McNeil, and Dr. Glareh Natalie Kashanchi thank you for your guidance and mentorship. Chris you were the best mentor I could have asked for. Thank you for always pushing me, I grew in both my knowledge and confidence working with you. Patricia and Natalie the two of you never ceased to amaze me. I am grateful to not only have gotten to learn from the two of you, but to consider you both two of my closest friends that I made during grad school. To those that I still see every day:

Brea Hogan, Henry Choi, Randy Chen, Bintao Hu, Yunkai Luo, Jacky Yu and Makena White thank you for making everyday fun. I've enjoyed our conversations over the years both of the intellectual variety and not, and can't wait to see what you all accomplish next.

To my friends William Albert and Kimberly Chan among so many others, thank you for always being there and helping to provide needed perspective, and a bit of fun.

To my family you have been my biggest supporters and I cannot thank you enough. I know that these last few years have been a lot but you're unwavering support in faith in me that I would accomplish my goals helped me get to the finish line. To my parents John and Debbie, from a young age the two of you have taught me to set my goals high and the importance of resilience on the journey to accomplishing them. Thank you for never letting me think any of my dreams were impossible. To my siblings Molly and John, thank you for always being there. I know having a sibling 3,000 miles away isn't the easiest but you two both made sure I never felt left out. To the rest of my family, there are too many of you to list- I am so grateful to have you all in my life, I know I can always count on all of you to be there for me regardless of the circumstances.

Lastly, to my wonderful partner Dakota, thank you for being there through every step of this journey and for entertaining every crazy idea I've ran by you. Through all this you have been my biggest cheerleader and have kept me grounded when I needed it. I wouldn't have wanted to do this with anyone else by my side.

Finally, I would like to acknowledge the UCLA Cota-Robles Fellowship, the NSF NRT: Graduate Traineeship in Integrated Urban Solutions for Food, Energy, and Water Management (INFEWS)–DGE-1735325, the Department of Energy EERE Advanced Manufacturing Office, and the Office of Naval Research for the financial support during my Ph.D.

Vita

2018	B.S. Chemistry- Materials Binghamton University, State University of New York President's Honors
2021-2022	Adjunct Policy Researcher, RAND Corporation
2019-2023	NSF INFEWS Traineeship
2020	UCLA Leaders in Sustainability Certificate Awarded
2018-2023	UCLA Cota Robles Fellow
2018-2023	Graduate Student Researcher Department of Materials Science and Engineering University of California, Los Angeles

Publications

Fox, M. T.; McNeil, P.; Yu, J.; Zhu, J.; Ramos, E.; Ellis, M.; Wood, M.; Worsley, M.; Wang, Y.M.; Dunn, B.S. Innovative Design and Manufacturing of 2.5D Battery with High Energy and Power Density. *Manuscript in Preparation, 2023.*

McNeil, P.; Guillemin, T.; Fox, M.; Le Bideau, J.; Dunn, B. Characterization of Fragility in Silica-Based Ionogels. *J. Phys. Chem. C* **2022**, acs.jpcc.2c05911. https://doi.org/10.1021/acs.jpcc.2c05911.

Marszewski, M.; Dashti, A.; McNeil, P. E.; Fox, M.; Wall, V.; Butts, D. M.; King, S. C.; Kashanchi, G. N.; Tolbert, S. H.; Dunn, B.; Pilon, L. Elastic and Plastic Mechanical Properties of Nanoparticle-Based Silica Aerogels and Xerogels. *Microporous and Mesoporous Materials* **2022**, *330*, 111569. https://doi.org/10.1016/j.micromeso.2021.111569.

Presentations

Fox, M., McNeil, P., Butts, D., Dunn, B., *Engineering Mesoporous Silica for Superior Optical and Thermal Properties*. Sol Gel Technologies 2022, July 24-29, 2022. (Oral)

Fox, M., *Engineering Mesoporous Silica for Superior Optical and Thermal Properties.* 3M RISE Symposium Invited Talk, Virtual, June 13-15, 2022. (Oral)

Fox, M., McNeil. P., Yu, J., Wang, M., Wood, M., Worsley, M., Dunn, B. *Innovative Design and Manufacturing of 2.5D Battery with High Energy and Power Density.* Vehicles Technology Conference Department of Energy, Washington, D.C. June 21-23, 2022. (Poster)

Chapter 1. Introduction and Motivation

Chapter 1.1. Motivation

For the last few decades, there has been a steady increase in the demand for lithium ion batteries (LIBs) across several industries including mobility, stationary storage, and consumer electronics (Figure 1.1).[1–3] This drive for greater reliance on LIBs has been further supported through decarbonization efforts by the U.S. government, with goals to decarbonize the electric grid by 2035, and to shift the automotive industry to electric vehicles in places like California.[2–5] More broadly, this increase in demand across all sectors can be seen through the growth of the Internet of Things (IoT).[6] The IoT, is a network of devices that collect and share data with other devices. For reliable self-sustained performance, these systems need sufficient, stable and instantaneous energy sources.[6,7] Batteries are a strong candidate for providing power because of their ability to store energy and provide a steady output of power needed for a given device.

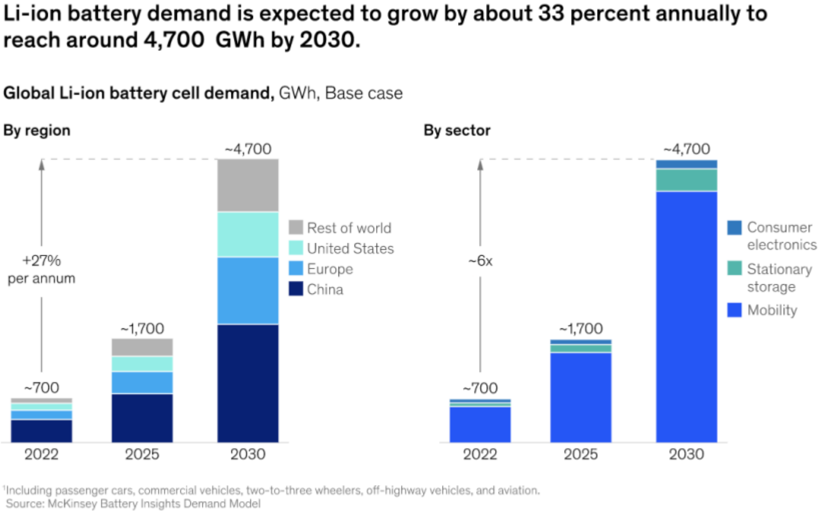

Li-ion battery demand is expected to grow by about 33 percent annually to reach around 4,700 GWh by 2030.

Global Li-ion battery cell demand, GWh, Base case

By region

By sector

[1]Including passenger cars, commercial vehicles, two-to-three wheelers, off-highway vehicles, and aviation.
Source: McKinsey Battery Insights Demand Model

Figure 1.1. Projected demand for lithium globally, and the projected demand by sector. Figure reproduced from ref 1.

With the demand of LIBs projected to grow exponentially in the next decade, the required device performance will vary based on its intended usage. As such, new metrics or standards have been set in various industries to support consumer usage.[1,3] For example, recent goals set by the Department of Energy stipulate that the manufacturing of batteries for electric vehicles need to be cheaper than $100/kWh, have a range of 300 miles and charging times of 15 minutes or less.[2,8] This directly translates to the batteries' energy and power densities respectively. While lithium ion batteries traditionally have a high energy density, they have low power density, leading to longer charging times. Currently, battery performance is limited by the device design, which utilizes planar electrode components. In order to meet these new metrics, changes have to be made to the design of batteries in both the materials being used and their architecture.

In recent years, there has been significant interest in three-dimensional (3D) batteries where the electrodes have a non-planar configuration. The work in this dissertation considers the differences with fundamental electrode designs and its effect on the overall performance of the battery system (Figure 1.2). Any device integration shown in this dissertation will be a 2.5D battery device utilizing a 3D cathode architecture, versus a 2D planar electrode (pressed lithium metal), and separated by a pseudo-solid electrolyte.

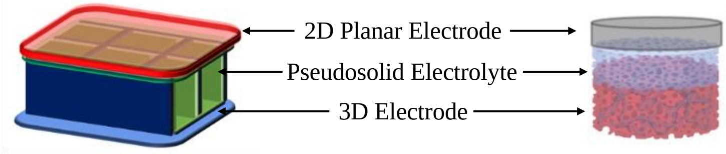

Figure 1.2. Example of 2.5D batteries with (a) a 3D printed electrode and (b) a 3D porous electrode, using a pseudo-solid electrolyte and a 2D planar cathode.

Chapter 1.2. Considerations for Non-Planar and Solid State Batteries

A current bottleneck in battery design is the use of planar electrodes. Typically, in a 2D planar system, thicker electrodes can have higher loading of active material giving larger energy densities, while thin electrodes have high power density, due to shorter diffusion distances.[9] The planar design especially limits micro-battery applications because in a confined areal footprint, either energy or power density is sacrificed. By using a multidimensional battery, the energy and power can be decoupled and the material loading and diffusion distance of Li-ions are more easily manipulated. The shift to non-planar architectures provides a pathway to faster rate capabilities because of the increased electrode/electrolyte interfaces, giving way to better penetration of electrolyte to the electrodes and increased charge/discharge rates.[10,11] A Ragone plot of a planar versus multidimensional electrode below (Figure 1.3) shows the relationship that these different architectures have with energy and power density.

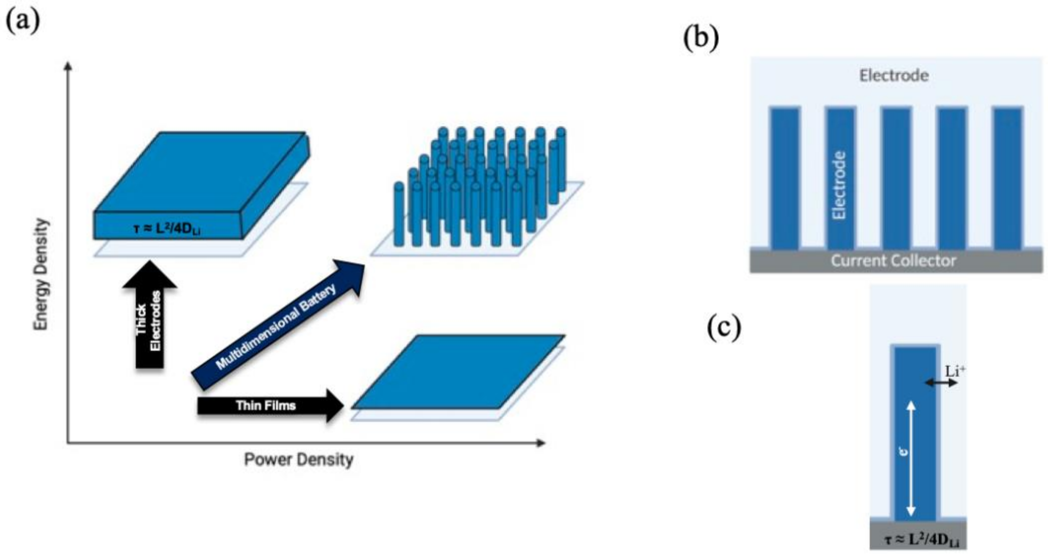

Figure 1.3. (a) Ragone plot of planar and multidimensional electrodes normalized to area. (b) Cross sectional depiction of a multidimensional electrode with a pillar design, and (c) example diffusion distance of the pillar.

Other three dimensional architectures reported in the literature, besides the interdigitated pillar or rod design shown in Figure 1.3, can be used to demonstrate the deconvolution of energy and power density[10,12,13] This includes, but is not limited to, structures based on interdigitated plates, concentric tubes, inverse opals and aperiodic sponges.[14–21] When developing an electrode design, both the anode and cathode need to be taken into consideration to ensure that the architectures are complementary and do not require additional alignment which can limit device fabrication and affect performance. For battery applications in general, certain material characteristics such as high specific capacity (charge stored normalized by mass), a large voltage window between the anode and cathode, and stable reversibility among others are taken into consideration. Additionally, when designing 3D architectures, another important characteristic of the material is having a low volume expansion to prevent mechanical failure from expansion and contraction during charging and discharging processes which occur in a battery.[21,22]

There are several means of fabricating 3D electrode architectures, however many microfabrication techniques are not trivial and have large startup costs. Some fabrication techniques include vat photopolymerization, photolithography, fused deposition modeling, and stereolithography. However, for manufacturing purposes, we not only want to keep the cost of manufacturing low but also have a large range of materials compatible with the technique.[11,22–25] With those considerations, Direct Ink Writing (DIW) will be the manufacturing technique used in some of this work. DIW is a continuous printing process which has shown promise for large scale processing while maintaining lower production costs and can be used with a variety of materials.

An alternative cost-effective scalable technique is sol-gel processing. In sol-gel processing, a precursor and catalyst form a colloidal solution which then aggregates to form a gel network.[26,27] While this technique is typically followed by additional processing and used for general material synthesis, it can also be used to create a highly porous gel network with an aperiodic sponge-like structure. An example of this is with ionogels which are pseudo-solid electrolytes.[28] This synthesis can be used for a variety of cathode materials—most commonly with transition metal oxides.

Another consideration with battery design is the electrolyte. In traditional batteries a liquid electrolyte is used to enable ion transport. These electrolytes, while they have good reported wetting and ionic conductivities, also have low physiochemical stability and flashpoints—leading to safety concerns. To improve safety, solid state batteries have been an area of interest. However, solid state electrolytes typically have lower conductivities and experience higher device resistance. Lastly, in conjunction with a non-planar electrode, there are manufacturing difficulties when using solid state electrolytes such as void formation and mechanical stress on the 3D architectures. A well-studied option has been to use a pseudo-solid electrolyte, like an ionogel. Here, the use of sol-gel processing to create a silica network that serves as a host medium for an ionically conducting medium, such as an ionic liquid electrolyte (ILE), allows for the sol to be used to coat any non-planar structures before gelation of the silica network. In this case silicon alkoxide precursors are used to form an ultra-porous network via an acid/base catalyzed reaction.[28] ILEs can then be infiltrated throughout the silica matrix to make it ionically conducting. While silica is electronically insulating, the high porosity of the gel network lets the electrolyte flow easily, allowing for the characteristics of the liquid electrolyte to still be used while encapsulated in the solid medium.[28–32] In this work, ionogels will be used as the electrolyte when discussing the fabrication of full devices.

Chapter 1.3. References

(1) *Battery 2030: Resilient, Sustainable, and Circular*; McKinsey & Company. https://www.mckinsey.com/industries/automotive-and-assembly/our-insights/battery-2030-resilient-sustainable-and-circular.

(2) DOE. Batteries, Charging and Electric Vehicles. https://www.energy.gov/eere/vehicles/batteries-charging-and-electric-vehicles.

(3) Castelvecchi, D. Electric Cars and Batteries: How Will the World Produce Enough? *Nature* **2021**, *596*, 336–339.

(4) Lopez, N. Rate to Zero: Can California's Power Grid Handle a 15-Fold Increase in Electric Cars? https://calmatters.org/environment/2023/01/california-electric-cars-grid/.

(5) *Grid Decarbonization*. Paving the way to a decarbonized power grid. https://www.siemens-energy.com/global/en/offerings/power-transmission/innovation/grid-decarbonization.html#:~:text=A%20decarbonized%20grid%20is%20crucial,efficiency%20as%20well%20as%20stability.

(6) Li, S.; Xu, L. D.; Zhao, S. The Internet of Things: A Survey. *Inf Syst Front* **2015**, *17* (2), 243–259. https://doi.org/10.1007/s10796-014-9492-7.

(7) Xu, L. D.; He, W.; Li, S. Internet of Things in Industries: A Survey. *IEEE Trans. Ind. Inf.* **2014**, *10* (4), 2233–2243. https://doi.org/10.1109/TII.2014.2300753.

(8) *VTO web page*. Vehicles Technology Office: Batteries, Charging and Electric Vehicles. https://www.energy.gov/eere/vehicles/batteries-charging-and-electric-vehicles.

(9) Ashby, D. S.; Choi, C. S.; Edwards, M.; Talin, A. A.; White, H. S.; Dunn, B. S. High-Performance Solid-State Lithium-Ion Battery with Mixed 2D and 3D Electrodes. *ACS Applied Energy Materials* **2020**, *3*, 8402–8409.

(10) Long, J. W.; Dunn, B.; Rolison, D. R.; White, H. S. 3D Architectures for Batteries and Electrodes. *Adv. Energy Mater.* **2020**, *10* (46), 2002457. https://doi.org/10.1002/aenm.202002457.

(11) Pang, Y.; Cao, Y.; Chu, Y.; Liu, M.; Snyder, K.; MacKenzie, D.; Cao, C. Additive Manufacturing of Batteries. *Adv. Funct. Mater.* **2020**, *30* (1), 1906244. https://doi.org/10.1002/adfm.201906244.

(12) Long, J. W.; Dunn, B.; Rolison, D. R.; White, H. S. Three-Dimensional Battery Architectures. *Chem. Rev.* **2004**, *104* (10), 4463–4492. https://doi.org/10.1021/cr020740l.

(13) Narita, K.; Saccone, M. A.; Sun, Y.; Greer, J. R. Additive Manufacturing of 3D Batteries: A Perspective. *Journal of Materials Research* **2022**, *37* (9), 1535–1546. https://doi.org/10.1557/s43578-022-00562-w.

(14) Arthur, T. S.; Bates, D. J.; Cirigliano, N.; Johnson, D. C.; Malati, P.; Mosby, J. M.; Perre, E.; Rawls, M. T.; Prieto, A. L.; Dunn, B. Three-Dimensional Electrodes and Battery Architectures. *MRS Bull.* **2011**, *36* (7), 523–531. https://doi.org/10.1557/mrs.2011.156.

(15) Pearse, A.; Schmitt, T.; Sahadeo, E.; Stewart, D. M.; Kozen, A.; Gerasopoulos, K.; Talin, A. A.; Lee, S. B.; Rubloff, G. W.; Gregorczyk, K. E. Three-Dimensional Solid-State Lithium-Ion Batteries Fabricated by Conformal Vapor-Phase Chemistry. *ACS Nano* **2018**, *12* (5), 4286–4294. https://doi.org/10.1021/acsnano.7b08751.

(16) Lai, J.; Nsabimana, A.; Luque, R.; Xu, G. 3D Porous Carbonaceous Electrodes for Electrocatalytic Applications. *Joule* **2018**, *2* (1), 76–93. https://doi.org/10.1016/j.joule.2017.10.005.

(17) Saleh, M. S.; Li, J.; Park, J.; Panat, R. 3D Printed Hierarchically-Porous Microlattice Electrode Materials for Exceptionally High Specific Capacity and Areal Capacity Lithium Ion

Batteries. *Additive Manufacturing* **2018**, *23*, 70–78. https://doi.org/10.1016/j.addma.2018.07.006.

(18) Roberts, M.; Johns, P.; Owen, J.; Brandell, D.; Edstrom, K.; El Enany, G.; Guery, C.; Golodnitsky, D.; Lacey, M.; Lecoeur, C.; Mazor, H.; Peled, E.; Perre, E.; Shaijumon, M. M.; Simon, P.; Taberna, P.-L. 3D Lithium Ion Batteries—from Fundamentals to Fabrication. *J. Mater. Chem.* **2011**, *21* (27), 9876. https://doi.org/10.1039/c0jm04396f.

(19) Chu, T.; Park, S.; Fu, K. (Kelvin). 3D Printing-enabled Advanced Electrode Architecture Design. *Carbon Energy* **2021**, *3* (3), 424–439. https://doi.org/10.1002/cey2.114.

(20) Egorov, V.; Gulzar, U.; Zhang, Y.; Breen, S.; O'Dwyer, C. Evolution of 3D Printing Methods and Materials for Electrochemical Energy Storage. *Adv. Mater.* **2020**, *32* (29), 2000556. https://doi.org/10.1002/adma.202000556.

(21) Sun, K.; Wei, T.-S.; Ahn, B. Y.; Seo, J. Y.; Dillon, S. J.; Lewis, J. A. 3D Printing of Interdigitated Li-Ion Microbattery Architectures. *Adv. Mater.* **2013**, *25* (33), 4539–4543. https://doi.org/10.1002/adma.201301036.

(22) Lyu, Z.; Lim, G. J. H.; Koh, J. J.; Li, Y.; Ma, Y.; Ding, J.; Wang, J.; Hu, Z.; Wang, J.; Chen, W.; Chen, Y. Design and Manufacture of 3D-Printed Batteries. *Joule* **2021**, *5* (1), 89–114. https://doi.org/10.1016/j.joule.2020.11.010.

(23) Chandrasekaran, S.; Yao, B.; Liu, T.; Xiao, W.; Song, Y.; Qian, F.; Zhu, C.; Duoss, E. B.; Spadaccini, C. M.; Li, Y.; Worsley, M. A. Direct Ink Writing of Organic and Carbon Aerogels. *Mater. Horiz.* **2018**, *5* (6), 1166–1175. https://doi.org/10.1039/C8MH00603B.

(24) Zhu, C.; Liu, T.; Qian, F.; Han, T. Y.-J.; Duoss, E. B.; Kuntz, J. D.; Spadaccini, C. M.; Worsley, M. A.; Li, Y. Supercapacitors Based on Three-Dimensional Hierarchical Graphene

Aerogels with Periodic Macropores. *Nano Lett.* **2016**, *16* (6), 3448–3456. https://doi.org/10.1021/acs.nanolett.5b04965.

(25) Qi, Z.; Ye, J.; Chen, W.; Biener, J.; Duoss, E. B.; Spadaccini, C. M.; Worsley, M. A.; Zhu, C. 3D-Printed, Superelastic Polypyrrole–Graphene Electrodes with Ultrahigh Areal Capacitance for Electrochemical Energy Storage. *Adv. Mater. Technol.* **2018**, *3* (7), 1800053. https://doi.org/10.1002/admt.201800053.

(26) Brinker, J.C., S., G. W. *Sol-Gel Science: The Physics and Chemistry of Sol-Gel Processing*; Academic Press, Inc., 1990.

(27) Levy, D., Z., M. *The Sol-Gel Handbook: Synthesis, Characterization, and Applications*; Wiley-VCH: Weinheim, Germany, 2015.

(28) Ashby, D. S.; DeBlock, R. H.; Lai, C.-H.; Choi, C. S.; Dunn, B. S. Patternable, Solution-Processed Ionogels for Thin-Film Lithium-Ion Electrolytes. *Joule* **2017**, *1* (2), 344–358. https://doi.org/10.1016/j.joule.2017.08.012.

(29) McNeil, P.; Guillemin, T.; Fox, M.; Le Bideau, J.; Dunn, B. Characterization of Fragility in Silica-Based Ionogels. *J. Phys. Chem. C* **2022**, acs.jpcc.2c05911. https://doi.org/10.1021/acs.jpcc.2c05911.

(30) Ashby, D. S.; DeBlock, R. H.; Choi, C. S.; Sugimoto, W.; Dunn, B. Electrochemical and Spectroscopic Analysis of the Ionogel–Electrode Interface. *ACS Appl. Mater. Interfaces* **2019**, *11* (12), 12088–12097. https://doi.org/10.1021/acsami.9b00093.

(31) Mitra, S.; Cerclier, C.; Berrod, Q.; Ferdeghini, F.; de Oliveira-Silva, R.; Judeinstein, P.; le Bideau, J.; Zanotti, J.-M. Ionic Liquids Confined in Silica Ionogels: Structural, Thermal, and Dynamical Behaviors. *Entropy* **2017**, *19* (4), 140. https://doi.org/10.3390/e19040140.

(32) Dutta, A.; Mishra, D. K.; Kundu, D.; Mahanta, U.; Jiang, S. P.; Silvester, D. S.; Banerjee, T. Examining the Electrochemical Nature of an Ionogel Based on the Ionic Liquid [P_{66614}][TFSI] and TiO_2: Synthesis, Characterization, and Quantum Chemical Calculations. *Ind. Eng. Chem. Res.* **2022**, *61* (25), 8763–8774. https://doi.org/10.1021/acs.iecr.2c00550.

Chapter 2. Electrochemical Characterization Techniques

Electrochemical Energy Storage (EES) Systems, such as batteries, utilize chemical energy and convert it to electrical energy. There are a variety of techniques used to study EES systems that can explain the behavior of a given device. Electrochemical cells are made of an anode, cathode and separated by an electrolyte. Each side of the cell is its own half-cell where at the anode and cathode sides an oxidation or reduction reaction occurs.[1,2]

These processes can be described by thermodynamics, where Gibbs free energy can be used to derive equations such as the Nernst Equation[3]:

$$E = -\frac{\Delta G^\circ}{nF} - \frac{RT}{nF} lnK = E^\circ - \frac{RT}{nF} lnK \qquad (Eqn.\ 2.1)$$

In addition to thermodynamics, kinetics also need to be favorable. When connected in a circuit, a battery has current that flows throughout to make it kinetically controlled. Additional energy is put into the system, the battery, to promote a reaction by overcoming a kinetic barrier. The energy needed to overcome the kinetic barrier is the overpotential.[1,2,4] Various techniques have been accepted by the battery community as a means of gaining more insight into the ongoing mechanisms inside the battery. Electrochemical testing is not limited to those mentioned here. Rather, these are the ones most commonly used in this dissertation.

Chapter 2.1 Galvanostatic Charge/Discharge Cycling

Galvanostatic Cycling (GV) is a commonly used technique to characterize the battery which involves charging and discharging the battery within a given voltage window at a constant current.[1] In a half-cell, this experiment reports the charge (mAh) of the electrode of interest normalized to the mass of the active material (specific capacity: mAh g^{-1}), or the electrode areal footprint (areal capacity: mAh cm^{-2}).

GV data is reported in terms of a charge rate or a C-rate that describes how long the battery takes to complete a charge or discharge. C-rates (mA) can be determined by taking the calculated maximum capacity and dividing that by the time to charge/discharge in hours. The resulting C-rates can then be reported as values such as C/10, 1C, or 5C, etc. to represent charging at 10 hours, 1 hour, or 12 minutes respectively. At slower C-rates, there are typically small deviations in overpotentials and specific capacities close to the theoretical value for the active material are achieved. At the faster rates, there are typically limitations in the kinetics, and the system sees a decrease in capacities, and increases in polarization. The decreases in capacity come from faster charging and discharging rates not allowing for as many redox reactions to occur due to limitations in diffusion and ionic transport in the electrolyte. The increases in polarization can occur from other processes such as ohmic drops (internal resistance), polarization of the activation energy, and concentration polarizations (Figure 2.1.).[5,6]

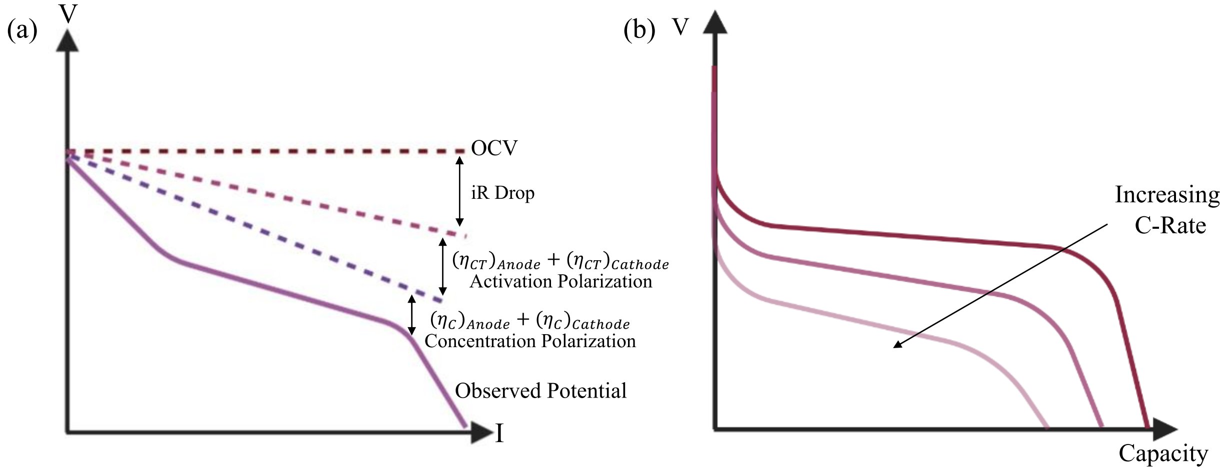

Figure 2.1. (a)Polarization curve (IV) for a battery material with contributing factors indicated for decreases in the cell potential at increasing currents (C-rates). Factors that lead to decreases in potential include ohmic drops, activation polarization, and concentration polarizations. (b) Resulting discharge from an increase in current density or C-rate. [Modified from reference [6]]

Lastly, one of the more commonly reported metrics for this test is the coulombic efficiency (CE), which describes the ability for a battery to recover the capacity achieved during charging. High CEs of almost or at 100% are needed for batteries to function over a number of cycles. Decreases in coulombic efficiency can be indicative of degradation in the battery such as formation of a solid electrolyte interphase (SEI) layer.

Chapter 2.2. Electrochemical Impedance Spectroscopy

Electrochemical Impedance Spectroscopy (EIS) has long been used to distinguish a variety of processes that happen within an electrochemical energy storage system. Parameters include electrolyte resistance, bulk diffusion, and charge transfer resistance within an electrode among others.[7–9] EIS reports the instantaneous current response based on an oscillating voltage at a given voltage and frequency to give an impedance value. Impedance is a resistance vector and can be related to the current and voltage response by Ohm's Law.[1,8] The reason that impedance is used instead of Ohm's law is because EES is often characterized by a non-ideal resistor.

The potential curve over the period of oscillation is represented as a function of time in terms of angular frequency (Eqn. 2.2.) and the current as a function of time in terms of angular frequency and peak phase shift (Eqn. 2.3., Figure 2.2.):

$$e_t = Esin(\omega t) \qquad (Eqn.\ 2.2)$$

$$i_t = Isin(\omega t + \phi) \qquad (Eqn.\ 2.3)$$

where ω is angular frequency or $2\pi f$. Then using Ohm's law along with the potential and current corrections over a given frequency range, the resistance at a given frequency (i.e., impedance) can be calculated:

$$Z = \frac{V}{I} = \frac{e_t}{i_t} = \frac{Esin(\omega t)}{Isin(\omega t+\phi)} = Z_o\,\frac{sin(\omega t)}{sin(\omega t+\phi)} \qquad (Eqn.\ 2.4)$$

This data is then commonly represented in one of two ways: either a Bode or Nyquist plot (Figure 2.2.). The Bode plot shows the relationship of the measured phase shift and resulting impedance value at a given frequency. This is helpful to understand what is happening at an exact frequency value. On the other hand, a Nyquist Plot shows the impedance vector broken down into Z_{Im} and Z_{Re} or the imaginary and real components. The imaginary component indicates how reactive or how well it can store energy while the real component indicates how well the system resists the flow of current.[1,7,8]

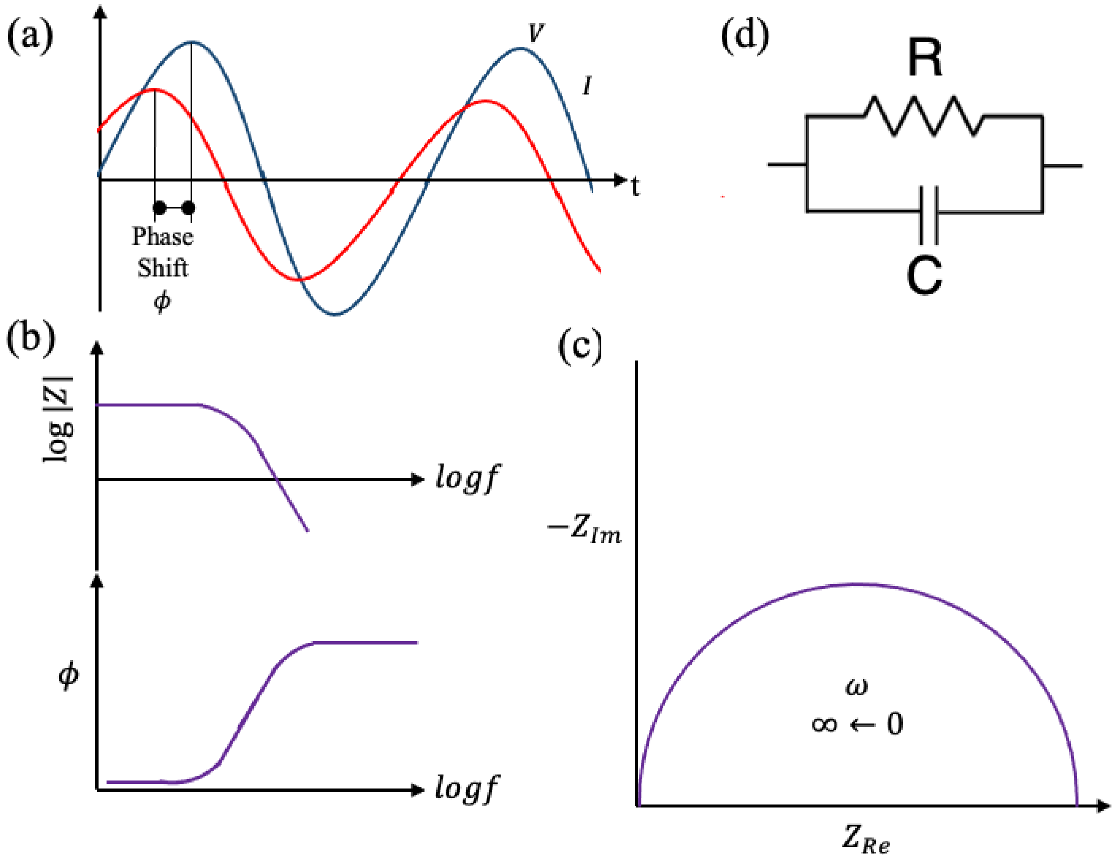

Figure 2.2. (a) Potential and Current response versus time, the phase shift of the peak current and potential is indicated. A representative (b) Bode plot, and (c) Nyquist plot for a (d) resistor and capacitor in parallel. For the Nyquist plot, the frequency range increases closer to the origin.

Figure 2.2. shows a simple circuit where at low frequencies current goes through the resistor element, while at the high frequencies, the current goes through the capacitor. Circuits, and the resulting Nyquist plot do get more complex depending upon the nature of the system. For example, for electrolyte resistance in a given system, the Nyquist plot could show a semicircle shifted to the lower frequency range, and have an initial non-zero point on the real axis. This non-zero value can be representative of initial electrolyte resistance. Then the following

semicircle describes the element the current travels through in the same way described in Figure 2.2, giving a capacitive or more kinetically controlled response.

When considering other materials, such as redox active materials in the presence of electrolyte, the Nyquist plot is represented by a Randles Circuit. The Randles Circuit describes a system that at high frequencies shows a semicircle followed by a tail at lower frequency ranges, shown in Figure 2.3. In the representative Nyquist plot, the initial value R_1 is the solution resistance, and R_2 the charge transfer resistance. At higher frequencies, there is a more capacitive dominated mechanism (kinetic control), followed by a region of mixed capacitive and diffusion controlled behavior. At the lowest measured frequencies, the impedance indicates there is mass transfer or diffusion control, indicated by the Warburg tail (Warburg Impedance element in the circuit). Values such as diffusion coefficients or the kinetic rate of reaction can be calculated from information deduced by the Warburg tail. Analysis of Nyquist plots will be done in chapters 3, 4, and 5.

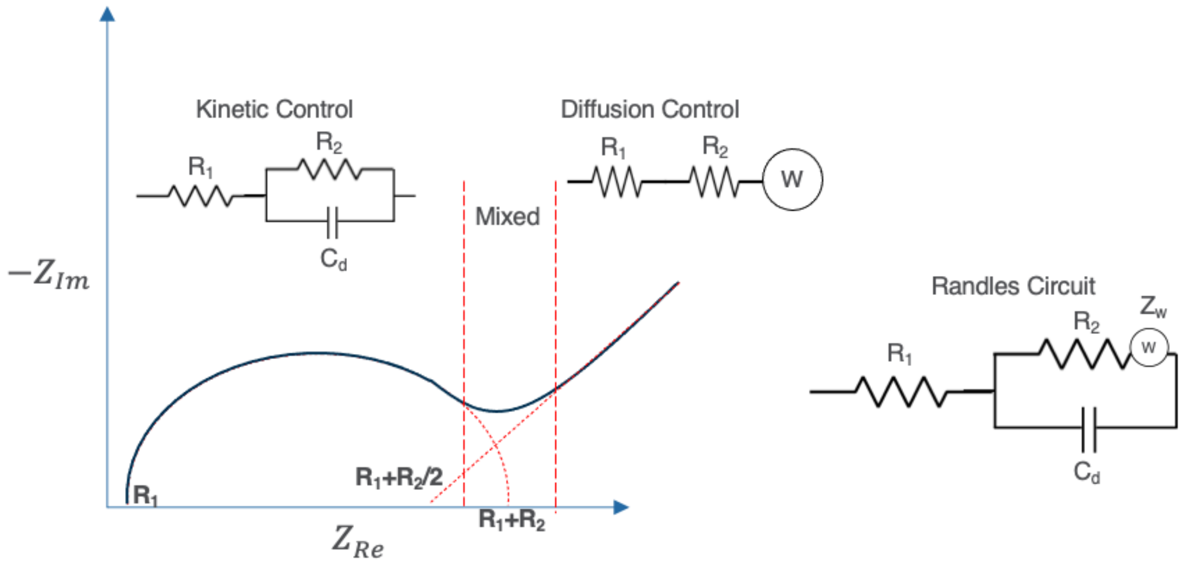

Figure 2.3. Representative Nyquist plot of a Randles Equivalent Circuit (circuit noted for all frequencies). Here, at higher frequencies the system is dominated by kinetic control, and towards lower frequencies diffusion/mass transfer control.

Chapter 2.3 Galvanostatic Intermittent Titration Technique

A technique used to calculate the kinetics of the battery system is the Galvanostatic Intermittent Titration Technique (GITT). The technique utilizes pulses of current for a period of time followed by a relaxation period. The voltage responses during the charging and relaxation periods can give insight into the operation of the battery system.[10,11]

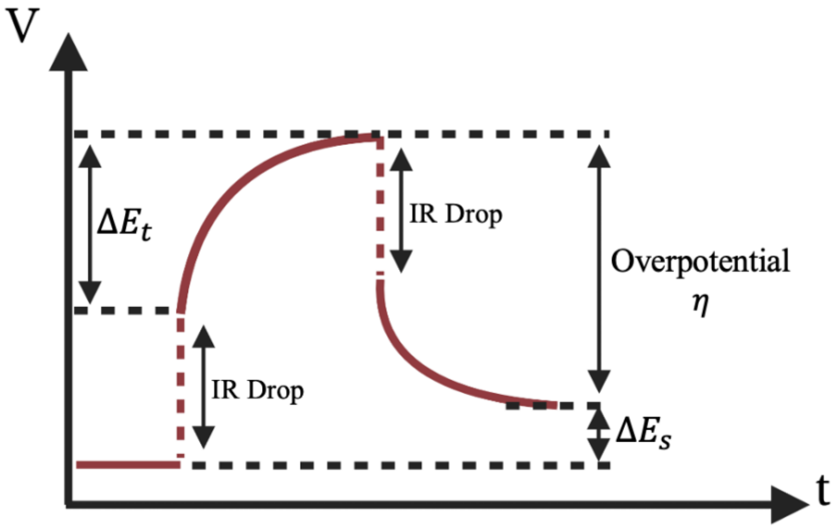

Figure 2.4. Representative GITT spectra showing an initial potential (OCV), and after an applied current the potential increases until it plateaus (ΔE_t). After a defined period of applied current, there is a relaxation period followed by an initial iR drop and potential equilibrates. The difference between the initial OCV and the potential after the relaxation period is ΔE_s, and the overpotential represented by the peak potential and the equilibrate potential. [Modified from reference [10]].

In a half-cell arrangement, GITT can be used to calculate both the overpotential and the internal resistance at the electrode being studied. In this measurement the overpotential (η) is determined by the measured potential at the end of the charging period, before current is stopped, and the potential at the end of the relaxation period when no current is flowing (open circuit voltage).[10–12] From here, the internal resistance can be calculated by dividing the overpotential by the applied current.

$$Internal\ Resistance\ (\Omega) = \frac{\eta}{|I|} \qquad (Eqn.\ 2.5)$$

Other information including the kinetics and thermodynamics of the system can be determined. An example is the open circuit voltage (OCV), being the Gibbs free energy at thermodynamic equilibrium ($\Delta G°(x)$):

$$OCV = \Delta G°(x) = -\frac{\mu_{Li}^{Cathode}(x) - \mu_{Li}^{Anode}(x)}{e} \qquad (Eqn.\ 2.6)$$

Where e is the electronic charge, and μ is the chemical potential at either the anode or cathode.[3,10,13] Additionally, the measurement can be used to calculate the diffusion coefficient that can be obtained by Fick's first law[4]:

$$J_o = I_o = \left(-D_o \frac{\partial c_{Li}}{\partial x}|_{x=0}\right) S z_{Li} q \qquad (Eqn.\ 2.7)$$

Fick's first and second law of diffusion can be used to derive an equation for the diffusion coefficient of lithium:

$$D = \frac{4}{\pi\tau}\left(\frac{m_B V_m}{M_B S}\right)^2 \left(\frac{\Delta E_S}{\Delta E_t}\right)^2 \ for \ \left(t \ll \frac{L^2}{D}\right) \qquad (Eqn.\ 2.8)^{10}$$

V_m and M_B *are* the molar volume and molecular weight of the electrode material. Respectively, E_s is the difference in the open circuit potentials before the charging and relaxation period, E_t is the initial potential drop after current is stopped. Lastly m_B, S, an*d* τ are representative of the electrode mass, area and the time increments for charging/relaxation periods. Using this method, the diffusion coefficient can be calculated at potentials across the entire studied potential window. Major changes in the value for the diffusion coefficient can be representative of another process happening at that potential where the change occurs.

Chapter 2.4. References

(1) Bard, A. J.; Faulkner, L. R.; White, H. S. *Electrochemical Methods: Fundamentals and Applications*, Third.; Wiley-VCH, 2022.

(2) Goodenough, J. B.; Park, K.-S. The Li-Ion Rechargeable Battery: A Perspective. *J. Am. Chem. Soc.* **2013**, *135* (4), 1167–1176. https://doi.org/10.1021/ja3091438.

(3) Gao, J.; Shi, S.-Q.; Li, H. Brief Overview of Electrochemical Potential in Lithium Ion Batteries. *Chinese Phys. B* **2016**, *25* (1), 018210. https://doi.org/10.1088/1674-1056/25/1/018210.

(4) Porter, D. A.; Easterling, K. E. *Phase Transformations in Metals and Alloys*, Second.; Chapman & Hall, 1992.

(5) Doyle, M.; Fuller, T.; Newman, J. Modeling of Galvanostatic Charge and Discharge of the Lithium/Polymer/Insertion Cell. *Journal of The Electrochemical Society 140* (6), 1526–1533.

(6) Saha, B.; Goebel, K. Modeling Li-Ion Battery Capacity Depletion in a Particle Filtering Framework. **2009**.

(7) Lazanas, A. Ch.; Prodromidis, M. I. Electrochemical Impedance Spectroscopy─A Tutorial. *ACS Meas. Sci. Au* **2023**, *3* (3), 162–193. https://doi.org/10.1021/acsmeasuresciau.2c00070.

(8) Browne, W. *Electrochemistry*; Oxford University Press: New York, New York, 2018.

(9) Fisher, A. C. *Electrode Dynamics*; Oxford University Press, 1996.

(10) Kim, J.; Park, S.; Hwang, S.; Yoon, W.-S. Principles and Applications of Galvanostatic Intermittent Titration Technique for Lithium-Ion Batteries. *J. Electrochem. Sci. Technol* **2022**, *13* (1), 19–31. https://doi.org/10.33961/jecst.2021.00836.

(11) Zhu, Y.; Wang, C. Galvanostatic Intermittent Titration Technique for Phase-Transformation Electrodes. *J. Phys. Chem. C* **2010**, *114* (6), 2830–2841. https://doi.org/10.1021/jp9113333.

(12) Olson, J. Z.; López, C. M.; Dickinson, E. J. F. Differential Analysis of Galvanostatic Cycle Data from Li-Ion Batteries: Interpretative Insights and Graphical Heuristics. *Chem. Mater.* **2023**, *35* (4), 1487–1513. https://doi.org/10.1021/acs.chemmater.2c01976.

(13) Chen, L.-Q. Chemical Potential and Gibbs Free Energy. *MRS Bull.* **2019**, *44* (7), 520–523. https://doi.org/10.1557/mrs.2019.162.

Chapter 3. Fabrication of Non-Planar Cathodes via Direct Ink Writing

The need for improved energy and power density in micro-batteries highlights a shift towards utilizing nonplanar electrode architectures. Differences in geometry- spacing/pitch length, aspect ratio, and proportion of printed features can dictate device performance metrics such as areal capacity and rate capability. Additive manufacturing processes including direct ink writing, are more cost effective than traditional microfabrication techniques and allow for versatility in printed structure in terms of design, while maintaining a high resolution. While 3D electrodes have shown improved energy and power densities, they do come with shortcomings in terms of fabrication, particularly in regard to alignment of the two 3D electrodes. Instead, the present work will aim to improve device performance by utilizing a 3D cathode structure in a 2.5D battery. A 2.5D battery utilizes a 2D planar electrode versus a 3D one, minimizing manufacturing defects during device fabrication. Among the accomplishments described in this chapter are the development of optimized lattice electrodes and areal capacities as high as 4.6mAh/cm^2 for a lattice with an aspect ratio of 3. Further testing was done to fully integrate the 3D architecture into a 2.5D device. Areal capacities of 1.2mAh/cm^2 were demonstrated for the full device.

Chapter 3.1. Introduction

Over the past few decades, there has been a steady increase in the demand for lithium ion batteries across several industries including mobility, stationary storage and consumer electronics.[1] More broadly, this increased demand across all sectors can be seen through the growth of the Internet of Things (IoT).[2,3] The IoT is a network of devices that collect and share data with other devices, with the addition of new devices in network projected to be a billion per year.[2] As these devices have gotten smaller, powering them efficiently has been a continued problem.

Because most of the IoT technology relies on being able to continuously process new information and provide a means of communication, a system that can enable high-energy and power output at the microscale is necessary. There have been advances in microscale power systems that would enable the necessary metrics for IoT technology, however, many experience fluctuations in power output because of their reliance on environmental means of deriving its power.[2,4,5] Batteries, more specifically micro-batteries, are strong candidates to be the power sources for these devices because of their ability to store energy and provide a steady output of power needed for a given device.[2] Lithium Ion Batteries (LIBs) are known for their high energy density but tend to lack the power density required for future consumer electronics, especially with regard to fast charging and discharging. These devices typically use planar electrodes in their design, leading to bottlenecks with electrochemical performance.

In a 2D planar system, thicker electrodes have higher loadings of active material giving larger energy densities, while thin electrodes have high power densities due to shorter diffusion distances.[6] The planar design in particular limits micro-battery application because in a confined areal footprint, either energy or power density is sacrificed. As such, there has been a shift seen in battery research from the traditional 2-dimensional planar battery electrodes to non-planar electrode architectures.[7–9] The move to non-planar architectures provides a pathway to faster rate capabilities because of the increased electrode/electrolyte interfaces giving way to lower local current density, better penetration of electrolyte to the electrodes and increased charge/discharge rates. However, the fabrication of 3D batteries is not trivial, and many use microfabrication techniques that are not cost effective. Here, we use an additive manufacturing (AM) method, Direct Ink Writing (DIW), to print 3D architectures. DIW is a method that allows for high volume and precision, with rapid, repeatable results.[11–14] Inks developed for DIW need to have shear yield stress and viscosities that enable for flowability of the ink while maintaining the printed shape. These ink metrics ensure high printing resolution, adhesion of printed structures, and uniformity of the electrode.

The 3D electrode architecture will then be integrated into a 2.5D micro-battery device. In a 3D battery, while there is improved energy and power density as mentioned above, the fabrication of these batteries tends to not be cost effective and defects that are prone to happen during manufacturing diminish their performance. Through this project, we will take advantage of the performance seen in 3D battery designs by slightly modifying the battery structure to help with cost and manufacturing. Previous work in this area demonstrated the development of a 2.5D battery structure.[6] The 2.5D battery would mean that instead of two electrodes of 3D vertical arrays, there would only be one (here the cathode) and the other electrode would be planar—removing the alignment step necessary in 3D batteries.

For non-planar architectures, by balancing line dimensions, height, aspect ratio, and pitch (distance between lines), it is possible to increase both energy and power density (area normalized) relative to conventional batteries with planar geometry. Because of the effective use of the "z" direction, 3D batteries have relatively small footprints and thus are being actively investigated for applications where compact designs are beneficial.[7,15,16] The focus of this work is on optimizing a 3D lattice cathode architecture for improved electrochemical performance, using lithium iron phosphate (LFP) as the active material, a common cathode material that possesses an olivine structure. The LFP olivine phase is made up of LiO_6, FeO_6 octahedra, and PO_4 tetrahedra that help to form channels in the [010] direction for lithium ion transport. The benefit of this structure during charging and discharging is its stability during cycling and minimal volume expansion, reported to be about 6.7%, appropriate for use in a non-planar architecture.[17–19] Materials that have low volume expansion during charging/discharging processes are ideal for non-planar applications as they minimize the mechanical stress experienced in the device.[14,20]

In designing different electrode architectures, to ensure that the electrochemical behavior in terms of energy, power density and rate capability are being characterized effectively, a baseline means of comparison needs to be established. In this work areal solid fraction (ASF), and area enhancement or enlargement factor (AEF) will be used. ASF, uses a top-down approach, neglecting height, and is a ratio of covered area vs the total areal footprint.

$$ASF = \frac{Covered\ Area}{Total\ Areal\ Footprint} = \frac{l^2-(n-1)^2s^2}{l^2} \qquad (Eqn.\ 3.1.)$$

Where *l* is the length of the electrode, *n* is the number of printed lines, and *s* the lattice spacing. The unitless value gives an indication on how open the 3D electrode structure is. In literature, this value is typically used to describe the device as a whole, but since this work focuses on the cathode, and testing is done in a half cell arrangement, it will just be used in reference to the 3D electrode.[11] AEF- area enlargement or enhancement factor describes the increase in accessible surface area when switching from a 2D planar design to a 3D architecture.[21–23] AEF gives a non-unit metric to compare the differences in the increased surface area of the architecture. With this value, lattices with a variety of different dimensions can be compared. These dimensions include variations in height and will more accurately be able to describe differences in aspect ratio. For this project, we used using a square lattice or grid design, so the calculation for AEF is as follows, where *h* is the electrode height:

$$AEF = \frac{Electrode\ Surface\ Area}{Total\ Areal\ Footprint} = \frac{l^2+4(n-1)^2(s*h)-(n-1)^2s^2}{l^2} \qquad (Eqn.\ 3.2.)$$

Other studies reported in literature have compared the efficacy of different additive manufacturing methods, and geometries.[11,24]

The present study manipulates line dimension, lattice spacing, and height of a 3D architecture to assist in electrode design by effectively using area and volume for a given electrode. This work will explore the effect of these aspects of electrode design for an optimized 3D cathode as well initial integration into a 2.5D device.

Chapter 3.2. Experimental Methods

Tape Cast Electrodes

For tape-cast electrodes, Lithium Iron Phosphate (LFP; American Elements) was prepared as a conventional electrode, where LFP was mixed with C65 carbon black and poly(vinylidene fluoride) (PVdF) in N-methyl-2-pyrrolidone (NMP) solution to form a uniform slurry. The formed slurry was cast onto an aluminum foil current collector using a doctor blade and dried in a vacuum oven at 110°C. Electrodes were then cut into 0.785cm^2 discs with loading from 1-2mg/cm^2 active material and thickness of $15\mu m$. Electrodes were then assembled in an argon-filled glove box into a half cell arrangement using a coin-cell with a lithium counter electrode and 1M $LiClO_4$ in EC:DMC (1:1 by volume) electrolyte.

Direct Ink Writing 2D and 3D Electrodes

Ink development and printing was led by Marissa Wood at Lawrence Livermore National Lab. Ink for printing 2D and 3D electrodes was prepared from a mixture of LFP, C65, and PVdF in a NMP solution mixed using a Thinky Mixer. Prepared inks were loaded into a syringe with a 200μm nozzle, and electrodes printed with a Hyrel Printer. 2D electrodes were printed using a

200µm nozzle to cover a 1cmx1cm area. 3D printed lattices were printed with either a 200 or 250µm nozzle and line spacing between 100-800µm to cover a 1cmx1cm area, with 1-5 layers of printed material. Electrode structures were printed onto carbon coated aluminum foil or glass. All printed electrodes were dried by covering with a petri dish in ambient conditions. Once dried, printed electrodes were further dried in a vacuum oven for 1 hour at 110ºC before assembling into a 2032 coin cell or flooded cell for electrochemical testing.

Microstructure Characterization of Printed Electrodes

Scanning Electron Microscopy (SEM) was done using an FEI Nova 230 Nano scanning electron microscope. Both planar and cross-section of tape cast and printed electrodes SEM images were obtained. SEM images were used to qualitatively determine the porosity of prepared electrodes using ImageJ analysis. N_2 adsorption testing was performed using a Micromeretics ASAP 3500 instrument to characterize the size distribution for internal pores of the printed lattices. Samples were heated at 110°C for two hours to remove any water before testing. BET surface areas were calculated, and BJH pore size distributions determined from isotherm data.

Electrochemical Testing

For tape-cast electrodes, electrochemical characterization was done on the assembled coin-cells. With printed electrodes, electrochemical testing was done in an assembled coin-cell or flooded cell with a lithium metal counter and reference electrode. All testing in a flooded cell was done in an argon-filled glove box. Cyclic voltammetry (CV) and galvanostatic charge-discharge (GV) measurements were made from 2.8-4V (vs. Li/Li+), and electrochemical impedance spectroscopy (EIS) measurements using a VMP potentiostat/galvanostat (Bio-Logic) or a Solatron Impedance Analyzer. Conductivity measurements were done using impedance spectroscopy on a Solatron. To determine electronic conductivity, samples were printed on glass slides and silver contacts were painted on to serve as contacts for testing. For ionic conductivity, samples were tested in a flooded three neck arrangement. The resistance and conductivity were then determined from the data in a Nyquist plot.

Chapter 3.3. Results and Discussion

For inks developed for DIW application, there are baseline mechanical properties for ink metrics to ensure their flowability while being able to maintain shape. Beyond studies of ink composition at UCLA, ink development and printing was led by collaborators at Lawrence Livermore National Laboratory. The developed inks demonstrated thixotropic or shear-thinning behavior, where viscosity decreases over time at a constant shear rate.[25,26] Viscosity measurements were taken of all developed inks to compare printability and their electrochemical properties. Two inks (LLNL1 and LLNL2) with comparable rheological properties and different active material content were developed and tested to determine specific capacity and coulombic efficiency (Figure 3.1).

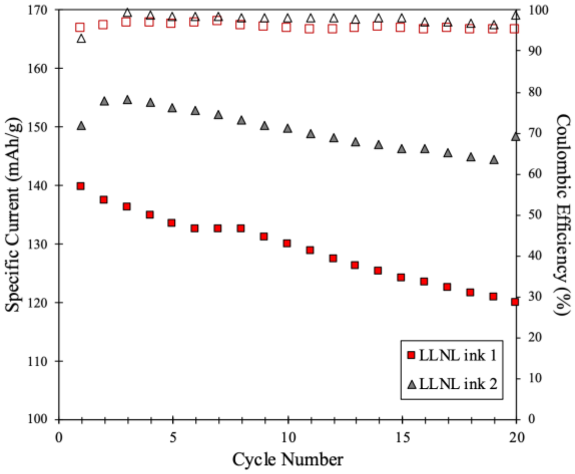

Figure 3.1. Comparison of specific capacity for LLNL Ink 1 and Ink 2 over 20 cycles and their coulombic efficiencies.

LLNL1 had a composition of 85% LFP and 7.5% of both carbon and PVdF, LLNL2 had 82.5% LFP to 8.75% of both carbon and PVdF by weight. Based on the cycling data, it was determined that while both had similar coulombic efficiencies over the tested cycles of at least 95%, LLNL2 maintained 94% of its capacity over 20 cycles while LLNL1 maintained 85% at a rate of C/10. Based on these findings, all lattices were made with LLNL2 ink.

Designing the Electrode- Considerations for Geometry

A baseline was created to compare electrodes made via a tape cast method to electrodes printed with DIW both in a 2D planar and 3D printed lattice geometry. Testing at various charge rates showed that the printed inks and slurry compositions have similar electrochemical properties to one another, and differences can be attributed to electrode geometry.

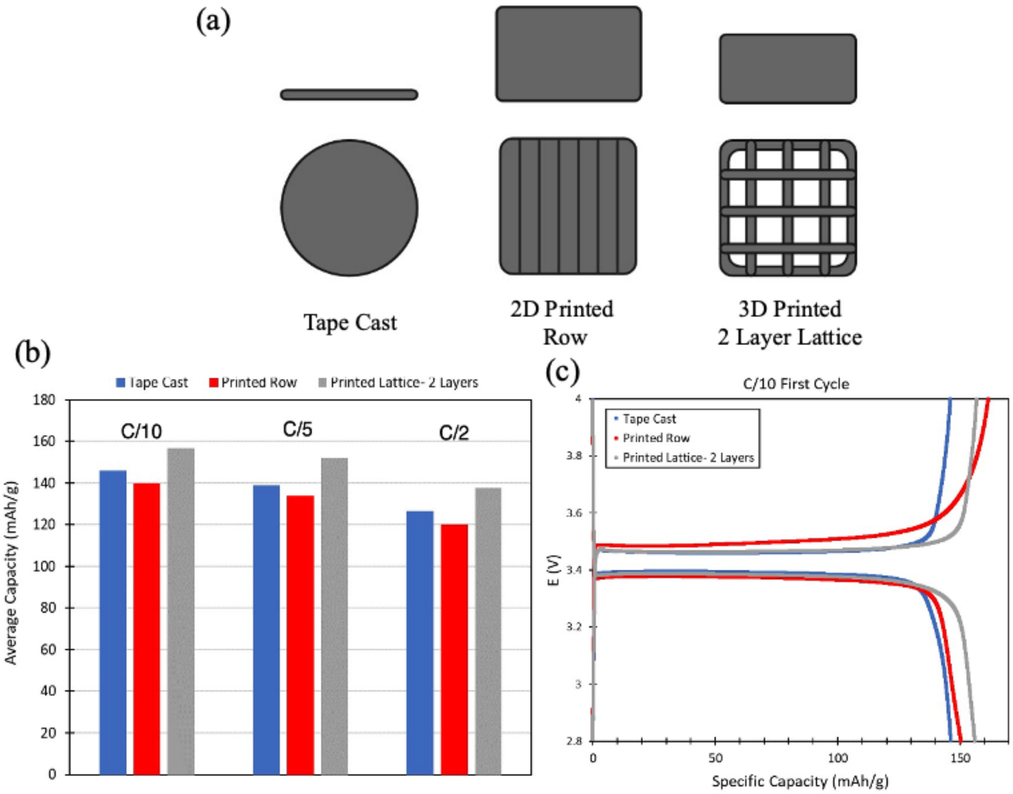

Figure 3.2. (a) Depiction of a tape cast, 2D printed planar, and 3D printed 2 layer lattice electrodes. (b) Specific Capacity of electrode structures at various rates. (c) First cycle specific capacity of 3 electrode architectures at C/10 rate.

The 2D printed row electrode and 3D printed lattice both have similar thicknesses of 150μm and 110μm respectively and loadings of 14mg/cm^2 versus 10mg/cm^2. Comparing the 2D printed electrode to the more open 3D printed structure, the 3D structure has a higher coulombic efficiency on the first cycle charge/discharge curve, higher specific capacity and also has a lower overpotential. This is shown by a smaller voltage separation between the charging and discharging curves, as well as a longer plateau region before sharply discharging at the knee. Having a well-defined knee indicates that there is less internal resistance compared to the 2D printed row.[27] An increased overpotential in the charging curve of the printed row can be seen.

Beyond charging at a rate of C/10, rates up to C/2 were tested and a higher maintained capacity at fast charging rates is shown in Figure 3.2. for the 3D lattice versus both the 2D printed and tape cast electrodes, where 88% of the capacity was maintained. The metrics ASF and AEF can be used to form an additional basis of comparison for these different structures. For ASF and AEF the 2D printed row has values of 1 for both, as the entire areal footprint here is covered. Comparatively, the 3D printed lattice demonstrates an ASF of 0.60, meaning 40% of the structure is open, and an AEF of 1.87 showing an increase in internal surface area as compared to the 2D printed lattice and tape cast electrode. From this, it can be determined that having a larger thickness will not impede device performance if there is a shorter diffusion pathway available, i.e., the open area given in a 3D lattice.

Table 3.1. Summary of a tape cast, 2D printed planar electrode, and a 3D printed lattice, comparing gravimetric and areal capacities.

Electrode Type	Loading (mg/cm^2)	Thickness (μm)	Areal Footprint (cm^2)	ASF	AEF	Gravimetric Capacity (mAh/g)	Areal Capacity (mAh/cm^2)
Tape Cast	2	15	0.785	1	1	145	0.29
2D Printed Row	14	150	1	1	1	140	1.96
3D Printed Lattice (2 Layers)	10	110	1	0.6	1.87	157	1.57

By modifying various aspects of the initial lattice design, metrics such as areal capacity, areal energy density and power density can be improved. In 3D battery architectures made via DIW, some ways to change the printed structure include the spacing between printed structures, the pitch, height, width of the printed line, and the aspect ratio (Figure 3.3.).[20,23] Aspect ratio is the ratio of the width of a feature to its height:

$$Aspect\ Ratio = \frac{Width}{Height} \qquad (Eqn.\ 3.3.)$$

As mentioned previously, when changing multiple aspects of the architecture, it is more difficult to have a baseline for their comparisons which is why comparison metrics such as ASF and AEF will be used to compare a 2D and 3D architecture (Table 3.1).

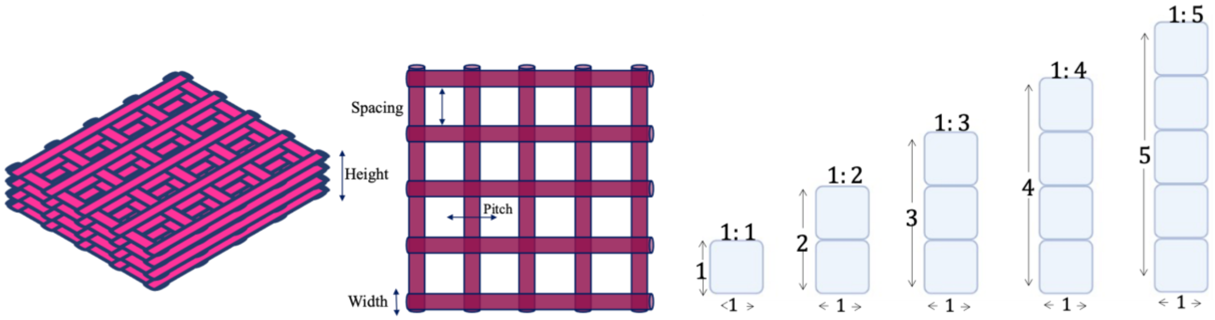

Figure 3.3. Geometry considerations when developing 3D architectures. (a) Representation of printed lattice, with architecture components identified, and (b) studied aspect ratios shown for 1:1 up to 1:5.

In addition to studying the effects of the overall geometry on electrochemical performance of the electrodes, microstructure of the electrode is also taken into consideration. However, because the same ink was used in the printing of all the electrodes, the pore structure was determined to be similar if not the same as one another by testing via nitrogen porosimetry. Nitrogen porosimetry is important to understand the pore size distribution (PSD) of the printed inks- for the mesopore regime in order to compare the lattices by another measure. BET data shows that the inks have the same pore size, and comparable surface areas, regardless of how much ink is printed. Therefore, just the printed geometry can be compared for the electrochemical data.

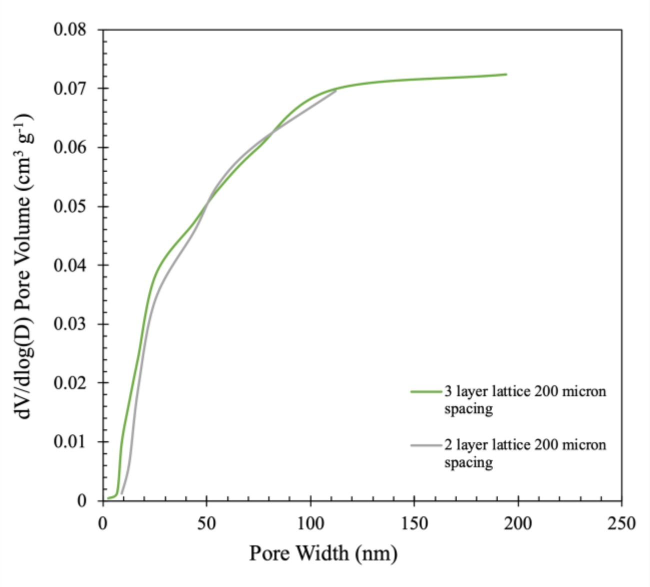

Figure 3.4. Pore size distribution for lattices printed with a 200μm nozzle and 200μm spacing with 2 or 3 layers.

Effect of Changing Pitch Length

One of the ways to modify the architecture is the pitch between features or spacing between the 3D features. The smaller the pitch, the higher the loading of active material as well as the AEF and ASF. However, it is important to note that the limit of how small the pitch length/spacing can be is determined by the smallest feature that can be resolved with the ink being used for printing. In this case, because a $200\mu m$ nozzle is being used for printing, the smallest spacing that can be clearly resolved is $100\mu m$, or one half the diameter of a lattice line. From this limiting size, the spacing can then be increased to $200\mu m$, $400\mu m$, and $600\mu m$ or 1:1, 2:1, and 3:1 ratio of the spacing to the diameter of the printed line.

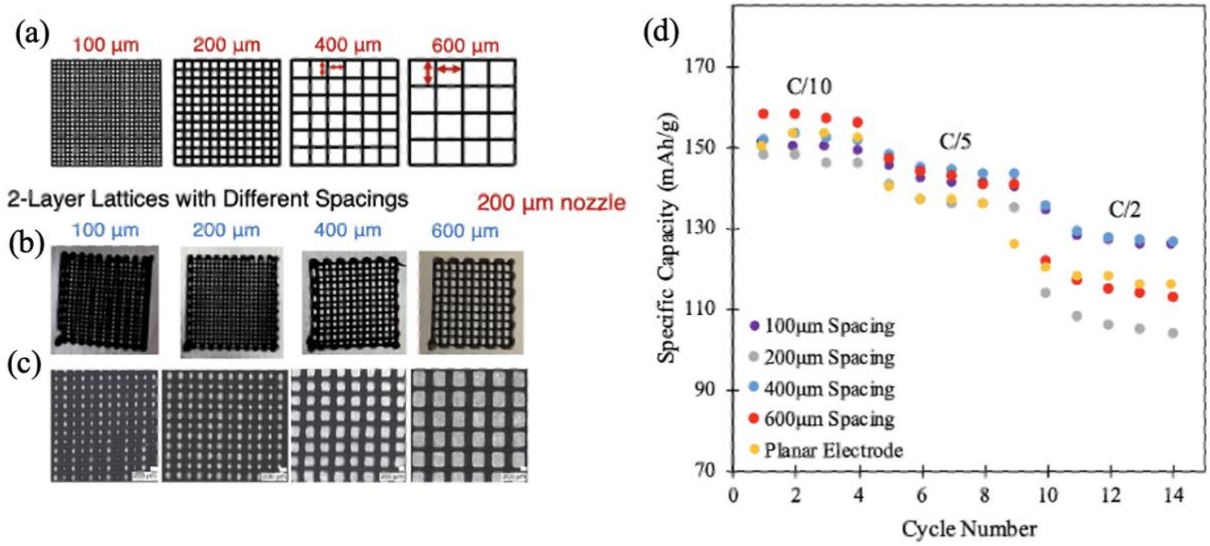

Figure 3.5. Lattices printed with a 200micron nozzle (a) initial renditions, (b) images, and (c) optical microscope images of lattices with 100, 200, 400, and 600μm spacing. (d) Measured specific capacity at rates of C/10, C/5, C/2 and C for all lattices and a 2D Planar Electrode

As shown in Figure 3.5, regardless of spacings, all lattices and the planar electrode have similar capacities at the slowest charge rate. At C/10, values are in the range of 150-155mAh/g or 88-91% of the theoretical specific capacity of LFP (170mAh/g). However, at faster charging rates there is a greater decrease in capacity for the 2D planar electrode and the 200μm, and 600μm spacing lattices. From the charging rate of C/10 to C/2 the 600μm spacing lattice and the planar lattice decreased capacity by 57%. Diffusion lengths, here the lattice spacing, become too great when more than twice the line width, and greater decreases in capacity are seen at faster charging rates. Electrochemical impedance comparisons (Figure 3.6) show a somewhat higher charge transfer resistance for the lattice with 200μm spacing compared to the 100μm and 400μm.

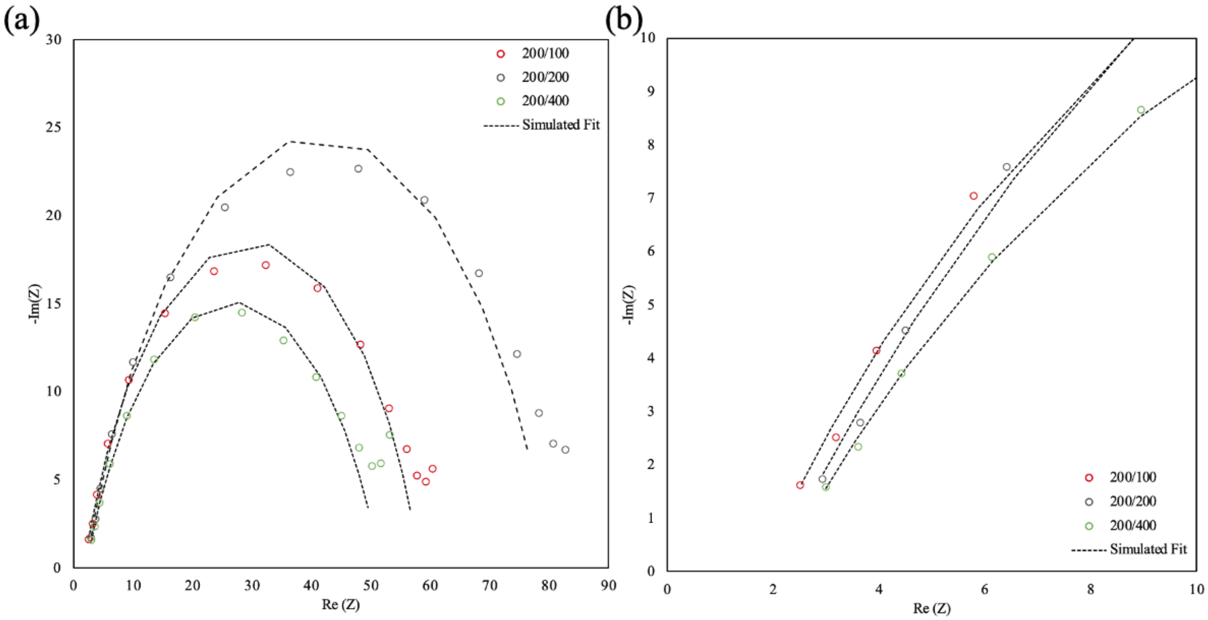

Figure 3.6. (a)Nyquist Impedance with a simulated fit for printed lattices with 100, 200, and 400µm spacing, (b) origin of Nyquist impedance.

Changing Proportions of lines –200µm vs 250µm nozzles

Loading of active material in the same areal footprint can be further increased by increasing the size or width of printed lines (Figure 3.3) while keeping other lattice proportions such as spacing and number of layers unchanged. The width of printed lines was enlarged from 200µm to 250µm by increasing the size of the printer nozzle. The lattice spacings used in the initial set of printed lattices allows for diffusion distances to remain low but with an increased areal capacity due to the higher loadings in the fixed areal footprint.

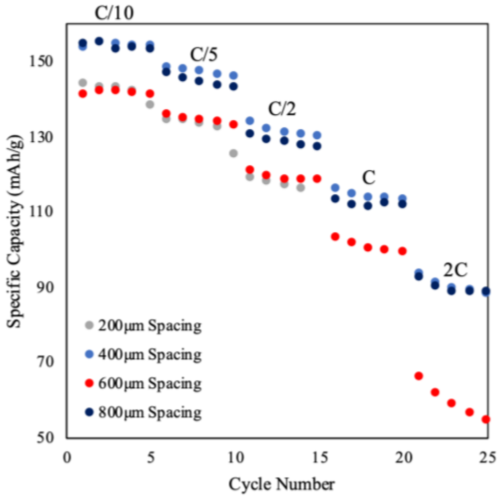

Figure 3.7. Measured specific capacity at rates of C/10, C/5, C/2, C and 2C for all lattice spacings printed with a 250µm nozzle.

The resolution of the printed lattices was not as high with the large nozzle as with the smaller printer nozzle leading to a limit on the separation distance between lattice lines and the number of layers that could be printed. For a 250µm nozzle, the limitation was 200µm spacing or a 0.8:1 ratio for lattice spacing to line width. Other lattice spacings printed were 400µm (1.6:1), 600µm (2.4:1), and 800µm (3.2:1). Despite the poorer printing resolution, high areal capacities were achieved. Moreover, with the 400 and 800µm spacing samples, the specific capacity is retained at faster charging rates, with only a 13% decrease in specific capacity from charging rates of C/10 to C/2. This behavior is similar to the decrease in capacity for samples printed with a 200µm nozzle and comparable ratios of lattice spacing to line width of about 2:1. The decrease in specific capacity for the lattice printed with the 200µm nozzle and a ratio of 2:1 was 15% from the C-rates C/10 to C/2.

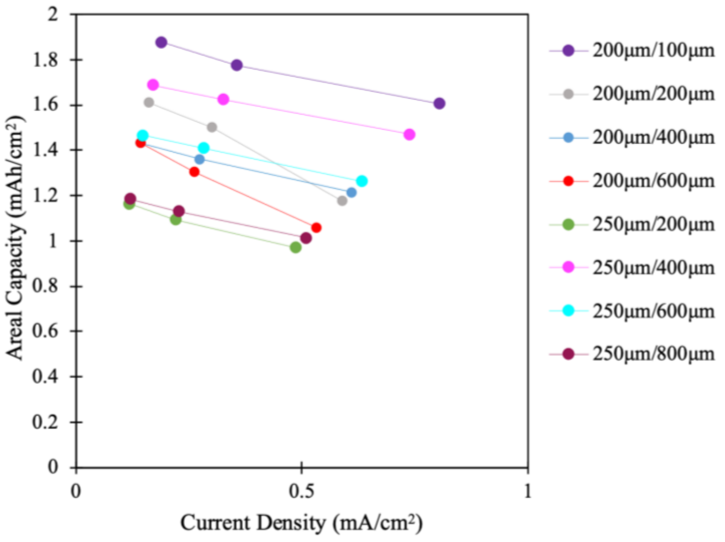

Figure 3.8. Areal Capacity as a function of applied current density for lattices printed with a 200 or 250μm nozzle, with various spacings. (The legend reads as nozzle size/lattice spacing).

All two layer lattices printed with either size nozzle can be compared by determining their areal capacities as a function of current density (Figure 3.8). For lattices of the same spacing, the lattices printed with a larger nozzle had higher areal capacities than the lattices printed with a smaller nozzle. This can be attributed to the increased loading of active material. However, when comparing increased line proportions and decreased lattice spacing, smaller lattice spacing is more effective for increasing areal capacity. Comparing the lattice with 100μm spacing and printed with a 200μm nozzle, the areal capacity is higher than any of the lattices printed with the 250μm nozzle even when charged and discharged at higher current densities (Figure 3.8). A summary of the printed 2 layer lattices is listed in Table 3.2, with ASF as the metric of comparison, since they utilize the same or similar heights as two layer lattices.

From these results and analysis, a minimum ASF of 0.25 proves beneficial for increasing and maintaining areal capacities at higher current densities. For lattices with small ASFs, an example being the lattice with 800μm spacing and 250μm nozzle with an ASF of 0.19, decreases in specific capacity were small, with as low as a 13% decrease when increasing the C-rate from C/10 to C/2. However, the areal capacities for lattices with ASFs lower than 0.25 are too low compared to those with higher ASFs because of low loading of active material. For micro battery applications the higher areal capacities are desirable because of the limited amount of available area for the power source.

Table 3.2. Summary of 2 Layer lattices, with their predicted and experimental areal capacities.

Number of Layers	**Size of Printing Nozzle (∝m)**	**Lattice Spacing (∝m)**	**Areal Solid Fraction**	**Predicted Areal Capacity (mAh/cm^2)**	**Experimental Areal Capacity (mAh/cm^2)**
2	200	100	0.54	1.13	1.12
2	200	200	0.40	0.84	0.71
2	200	400	0.26	0.56	0.55
2	200	600	0.20	0.42	0.46
2	200	800	0.16	0.34	0.51
2	250	200	0.44	1.17	1.17
2	250	400	0.30	0.81	1.67
2	250	600	0.23	0.62	1.46
2	250	800	0.19	0.50	1.18

Increasing Aspect Ratio

Beyond increasing areal capacity and loading by increasing line width, areal capacity can be increased with aspect ratio. As demonstrated in Figure 3,3 and equation 3.3, aspect ratio is the ratio of the width of the printed element to its height. The lattices already reported on have aspect ratios of 1:2 for a 2 layer lattice with a fixed line width of 200µm. In this section the studied aspect ratios will range from 1:1 for a single layer of the lattice design, up to 1:5 by printing a 5 layer lattice. To be able to predict what the areal capacities will be for the lattices printed with an increasing number of layers, density of the ink, and specific capacity can be used. The predicted loading and areal capacities for lattices printed with a 200µm nozzle using various spacings and increasing layers is shown in Figure 3.9.(a).

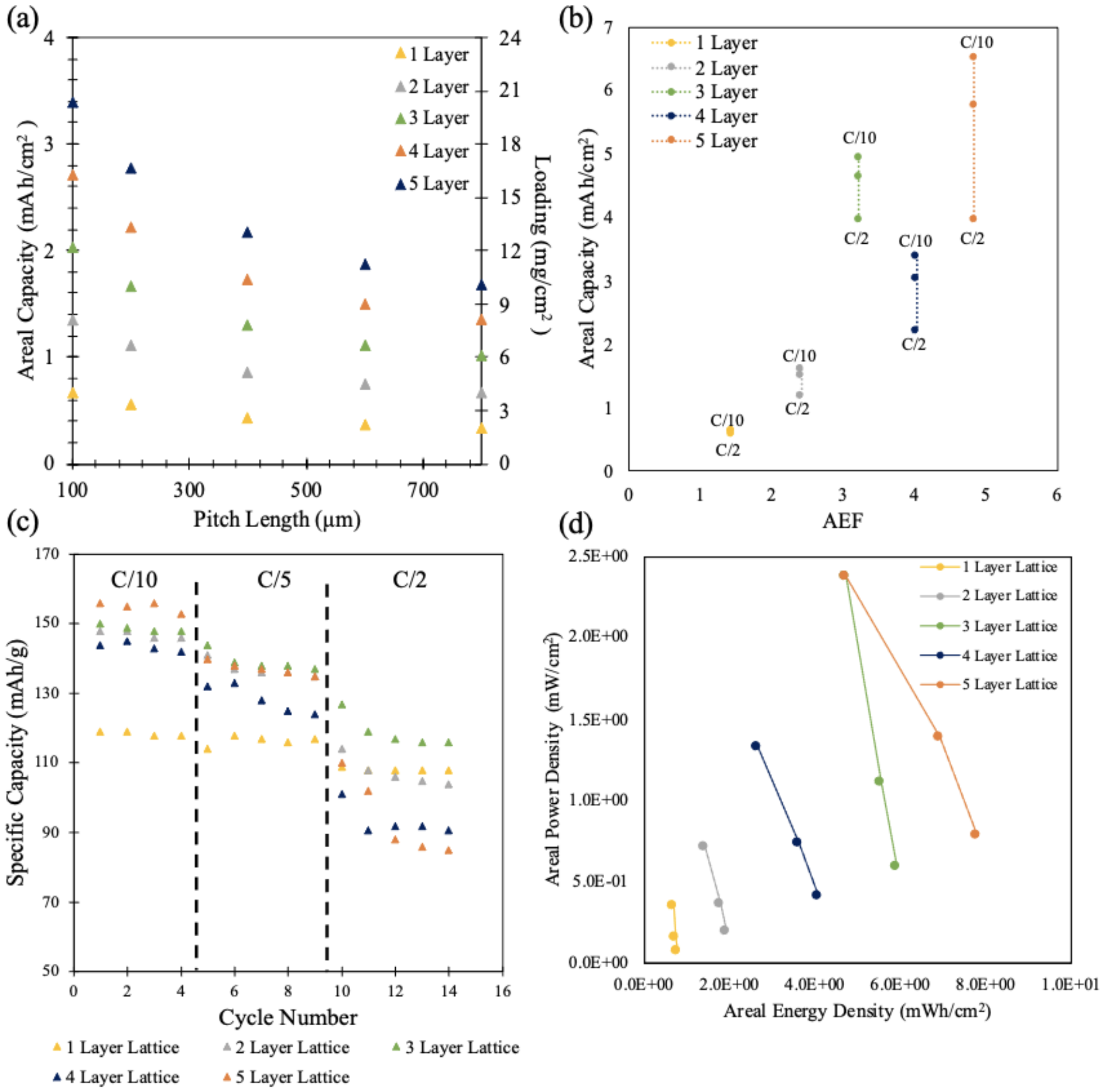

Figure 3.9. (a)Projected areal capacities and loadings for electrodes of varying pitch lengths and aspect ratios. (b) Areal capacity as a function of AEF for charging rates of C/10 to C/2, (c) specific capacity at varying charging rates, (d) areal power and energy of lattices with a fixed width (200μm), spacing (200μm) and increasing thickness (number of layers).

From the predicted values, the optimal lattice spacings and number of layers can be determined. Based on the results for the two layer lattices, the 100μm spacing lattice had the best performance metrics. However, because of ink bleeding during printing, resolution of the printed lattice could not be maintained as more layers were added. For this reason, 200μm spacing was used. In this case, all printed lattices have the same ASF due to the same lattice spacing and line width. Therefore, AEF can be used to further compare the lattices' areal capacity at multiple charging rates. Typically, AEF has been reported to have a positive correlation with improved areal capacity as well as rate capability.[22,23,28] Based on the results at rates of C/10 and C/5, the 5 and 3 layer lattices had the highest specific capacity, however, the 5 layer lattice did not maintain the capacity at the faster charging rates. Similar behavior was seen in terms of the areal energy and power density.

The decrease in specific capacity and areal capacity of the 5 layer lattice might be attributed to there being a mechanical limit to the lattice design. The 5 layer and 4 layer lattices both experience a 10% decrease in capacity when the charge rate is increased from C/10 to C/5, and an additional 30% decrease in capacity at C/2. This compares to lattices with 3 layers or less, where the initial decrease in capacity from C/10 to C/5 is approximately 6%. When increasing the rate to C/2 for the 3 layer lattice, the decrease in capacity is still less than half that of the 4 and 5 layer lattice at only 14%. Taken together these results indicate that the areal capacity is highest for a five layer lattice, but this is only at slower rates. For a fast charging application, as in the case of IoT devices, the higher aspect ratio lattice should not be used.

Lattice Recommendations

In analyzing all of the printed lattices, the most effective means of increasing areal capacity, and loading of active material was by increasing the number of layers used in the lattice design (Figure 3.10). This point is evident when considering all of the two layer lattices. All two later lattices have similar areal capacities. While AEF does increase with both the 200µm or 250µm printed lattices with different spacings, the improvement is not as clear as with the higher aspect ratio lattices.

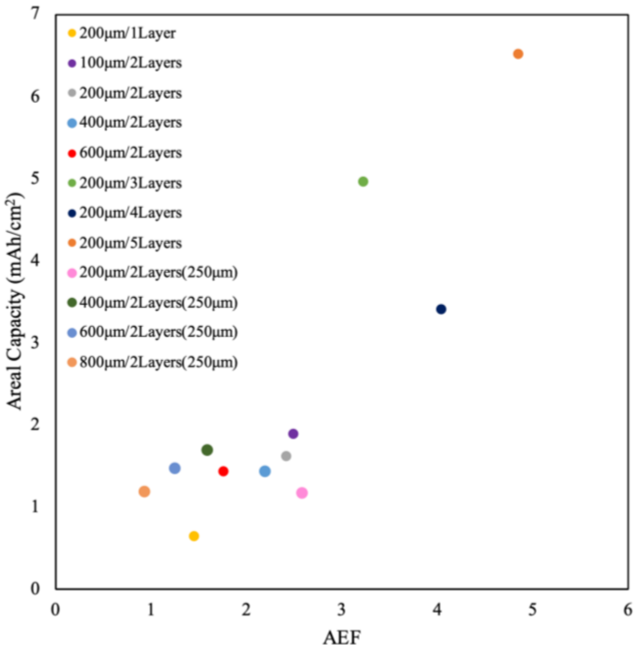

Figure 3.10. Areal Capacity as a function of Area Enhancement Factor for all lattices printed with a 200µm nozzle at C/10.

While the high AEF that came from increasing the aspect ratio had the highest areal capacities, the capacities decreased more rapidly at faster rates than lattices with aspect ratios of 1:3 or less. A summary of all lattices printed both with the 200 and 250µm is listed in Table 3.3.

Table 3.3. Summary of all printed electrode. Values for areal capacity, areal energy density and areal power density are from a charge rate of C/5.

Sample	**Thickness (μm)**	**ASF**	**AEF**	**Areal Capacity (mAh/cm^2)**	**Areal Energy Density (mWh/cm^2)**	**Areal Power Density (mW/cm^2)**
Tape Cast	15	1.00	1.00	0.29	0.35	0.07
2D Planar	150	1.00	1.00	1.76	2.11	0.42
200-200 1 Layer	200	0.49	1.45	0.63	0.76	0.15
200-100 2 Layer	400	0.73	2.48	1.78	2.13	0.43
200-200 2 Layer	400	0.60	2.41	1.50	1.80	0.36
200-400 2 Layer	400	0.47	2.19	1.36	1.63	0.33
200-600 2 Layer	400	0.40	1.76	1.31	1.57	0.31
200-200 3 layer	600	0.60	3.22	4.63	5.56	1.11
200-200 4 layer	800	0.60	4.03	3.04	3.65	0.73
200-200 5 layer	1000	0.60	4.84	5.77	6.92	1.38
250-200 2 Layer	500	0.64	2.58	1.09	1.31	0.26
250-400 2 Layer	500	0.51	1.59	1.63	1.96	0.39
250-600 2 Layer	500	0.44	1.24	1.41	1.69	0.34
250-800 2 Layer	500	0.39	0.93	1.13	1.36	0.27

2.5D Device Integration

While verification of the individual DIW electrodes is important for determining the capacity of LFP in various 3D architectures, integration of these 3D lattices into a full 2.5D solid-state battery provides important insight for the future development of 3D solid-state batteries. To integrate the lattices into a device, the lattices were first coated with a pseudo-solid electrolyte. The pseudo-solid electrolyte, known as an ionogel, uses sol-gel processing to form an insulating silica matrix which incorporates a continuous ionically conducting liquid phase. Because the ionogel is made by a solution based process, it can be coated on any geometry and maintain its microstructure.[29–31] In this case, the ionogel coating allows for a uniform surface that can be placed on a 2D planar electrode (pressed lithium metal). A similar device using a pillar cathode design was previously reported by Ashby et.al.[6]

The conducting phase of the ionogel is comprised of an Ionic Liquid Electrolyte (ILE). ILEs are known for their high chemical and thermal stability, and low volatility.[32–34] This makes them an ideal solvent to infiltrate into the silica network, because it will not evaporate from the pores unlike an alcohol-based solvent that will evaporate from the ionogel pores due to its high volatility. However, when screening different potential ILEs, it was found that there were better kinetics and higher capacity when using an organic electrolyte. A pre-cycling process was developed in which the initial ionogel that was synthesized using an ionic liquid electrolyte was subsequently immersed in a flooded cell with desired organic electrolyte (1M $LiClO_4$ in EC:DMC) to produce solvent exchange. By using this procedure, it was determined that by doing 2 to 3 charge/discharge cycles at a slow rate (C/10), solvent exchange can occur faster and was more effective in removing the majority of the ionic liquid electrolyte from the ionogel coating the LFP lattice. Using a flooded cell, longer term studies were also done to determine if pre-cycling had any major effect on the stability of the ionogel and the system as a whole (Figure 3.11). The tested pre-cycled ionogel coated lattice was shown to be stable after the initial pre-cycling process. The slight polarization in the charging curve of the sample at all rates is from the initially mixed ILE and organic electrolyte in the silica network.

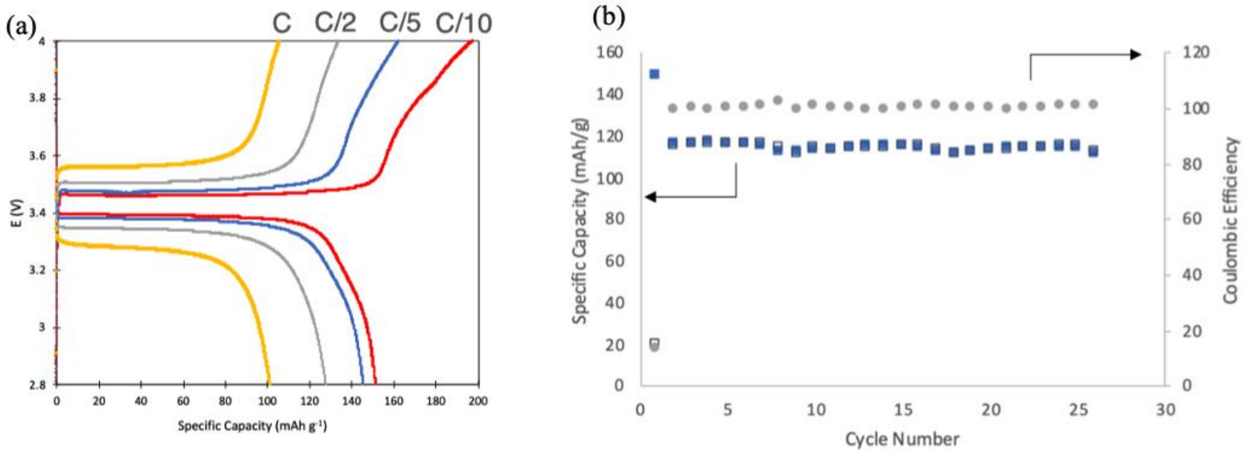

Figure 3.11. Galvanostatic Cycling for a solvent exchanged ionogel coated lattice (line width 200μm nozzle and spacing 400μm) at (a) various rates from C/10 to C, (b) discharge capacity at C/2 for 25 additional cycles. Pre-cycled sample, testing was done in a flooded 3-neck with 1M $LiClO_4$ EC:DMC electrolyte.

The pre-cycled electrodes were assembled into a full 2.5D device after the initial slow rate cycles. The fabrication process is outlined in Figure 3.12. Initially, there were contact issues between the ionogel and the lithium metal anode due to uneven coating of the gel. To help mitigate this issue, a glass fiber separator with a window cutout for the lattice was used in device fabrication. The addition of the separator helped with the contact issue and a full 2.5D battery was fabricated. The ionogel/lattice electrode underwent two pre-cycles in a flooded cell at a rate of C/10 before being integrated into the device. The full 2.5D battery underwent over 50 cycles at rates of C/10, C/5, and C/2. The discharge capacities for these cycles are shown in Figure 3.13.

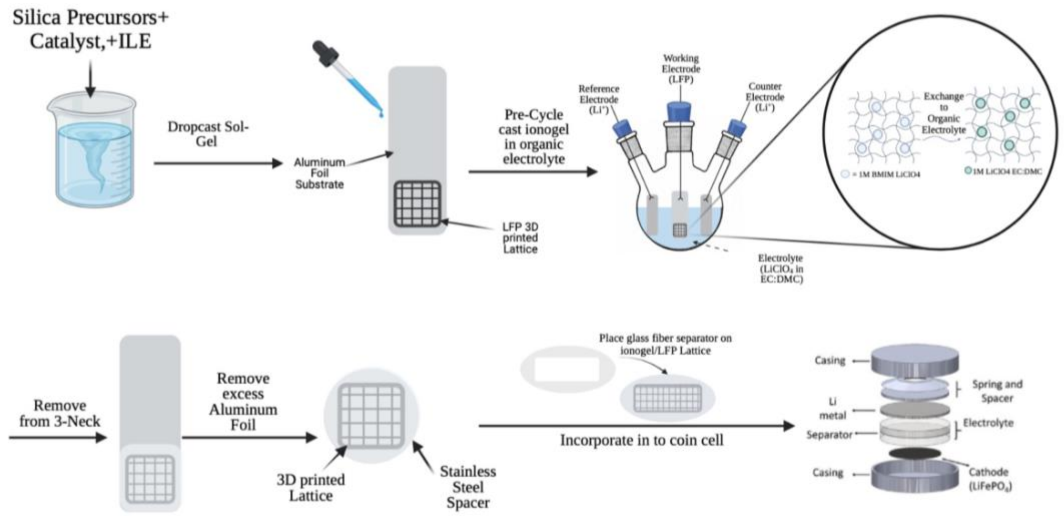

Figure 3.12. Optimized fabrication process flow for full 2.5D battery.

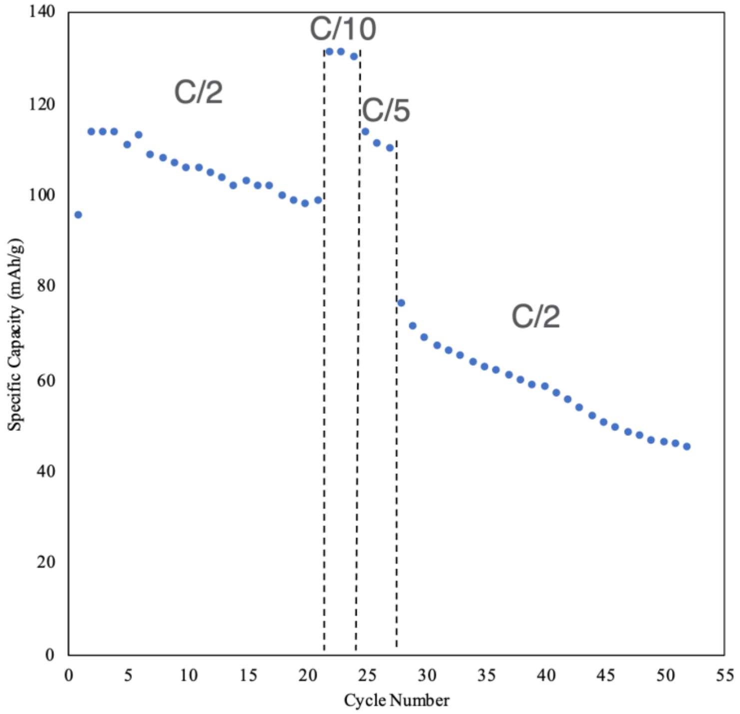

Figure 3.13. Measured discharge capacity by cycle for a full 2.5D battery at various rates. The measured discharge capacity at C/2 was approximately 105mAh/g, ~63% of the theoretical lithium capacity for LFP. Capacity did improve at slower rates of C/10 and C/5, where at C/10

the areal capacity was 1.2mAh/cm^2. The measured discharge beyond cycle 30 showed decay in the capacity.

Table 3.4. compares the current work to other reported multidimensional batteries specifically using LFP as a cathode. This shows that these results are comparable to a variety of different 3D battery designs, both for the full 2.5D device (Lattice: 200 µm nozzle, 400µm spacing, 2 layer) and for the multidimensional electrode (Lattice: 200 µm nozzle, 200µm spacing, 3 layers). Compared to the work of Ashby et. al., that used an LFP pillar array fabricated by etching to achieve 1.2mAh/cm^2 at 5mA/cm^2, all the other cited work use a 3D printing technique.[6] The work of Sun et. al., uses the same microfabrication technique (DIW) and electrolyte (1M $LiClO_4$ EC:DMC) as the current work, but with an interdigitated wall geometry. They were able to achieve 2.0mAh/cm^2 at a rate of 1C, compared to the full device in this work that was 1.2mAh/cm^2 at C/10. Further work on the full device, using the optimized 3 layer lattice will further improve the reported areal capacity. As stated previously, in a half cell arrangement, the 3 layer lattice has reported areal capacities of 4.63mAh/cm^2 at C/5.

Table 3.4. Comparison of LFP Multidimensional Electrode Devices reported in literature to the current work.

Electrode Material (Cathode/Anode)	Electrode Geometry	Microfabrication Technique	Electrolyte	Areal Capacity (mAh/cm^2)	Charging Rate	Reference
LFP/Li	Pillar Array	XeF_2 Dry Etching	Ionogel	1.2 mAh/cm^2	5 mA/cm^2	[6]
LFP(rGO)/ LTO(rGO)	Interdigitated Walls	3D Printing	1M $LiPF_6$ EC:DEC	152 mAh/g	50 mA/g	[35]
LFP/Li	Planar	Ink Jet Printing	1M $LiPF_6$ EC:DMC	80 mAh/g	9C	[36]
LFP/LTO	Interdigitated Planes	DIW	1M $LiClO_4$ EC:DMC	2.0mAh/cm^2	1C	[20]
LFP/Li	*Lattice*	*DIW*	*1M $LiClO_4$* *EC:DMC*	*4.63mAh/cm^2*	*C/5*	*This Work*
LFP/Li	*Lattice*	*DIW*	*Ionogel*	*1.2mAh/cm^2*	*C/10*	*This Work*

Chapter 3.4. Conclusions

The research in this chapter shows the development of electrode architectures based on a lattice design printed via DIW. Architecture and loading of active material play a role in the electrochemical performance and increasing metrics such as the areal enhancement factor have been shown to improve areal capacity. Overall, lattices printed using two different size nozzles and spacings ranging from 100µm to 800µm, and 1 to 5 layers were successfully fabricated and tested. Based on electrochemical measurements made in a half-cell arrangement, the optimized lattice was determined to have a high AEF and a minimum ASF of 0.25. The results also show that an aspect ratio no larger than 3 should be used to limit capacity decay. A LFP 3D lattice was successfully coated with an ionogel pseudo-solid electrolyte and integrated into a full 2.5D micro-battery device, achieving areal capacities of 1.2mAh/cm^2. The ability to identify architectural parameters that can be modified in order to achieve high areal capacities is important for improving upon current micro-batteries. For all lattices, a summary of their electrochemical performances are summarized in Table 3.3. The performance of these devices also establishes that using DIW in the fabrication of 3D battery designs with solid state architectures offers a promising direction for battery technology.

Chapter 3.5. References

(1) *Battery 2030: Resilient, Sustainable, and Circular*; McKinsey & Company. https://www.mckinsey.com/industries/automotive-and-assembly/our-insights/battery-2030-resilient-sustainable-and-circular.

(2) Li, S.; Xu, L. D.; Zhao, S. The Internet of Things: A Survey. *Inf Syst Front* **2015**, *17* (2), 243–259. https://doi.org/10.1007/s10796-014-9492-7.

(3) Xu, L. D.; He, W.; Li, S. Internet of Things in Industries: A Survey. *IEEE Trans. Ind. Inf.* **2014**, *10* (4), 2233–2243. https://doi.org/10.1109/TII.2014.2300753.

(4) Neményi, M.; Kovács, A. J.; Oláh, J.; Popp, J.; Erdei, E.; Harsányi, E.; Ambrus, B.; Teschner, G.; Nyéki, A. Challenges of Sustainable Agricultural Development with Special Regard to Internet of Things: Survey. *Progress* **2022**, *18* (1), 95–114. https://doi.org/10.1556/446.2022.00053.

(5) Shen, Z.; Jin, J.; Tan, C.; Tagami, A.; Wang, S.; Li, Q.; Zheng, Q.; Yuan, J. A Survey of Next-Generation Computing Technologies in Space-Air-Ground Integrated Networks. *ACM Comput. Surv.* **2023**, 3606018. https://doi.org/10.1145/3606018.

(6) Ashby, D. S.; Choi, C. S.; Edwards, M.; Talin, A. A.; White, H. S.; Dunn, B. S. High-Performance Solid-State Lithium-Ion Battery with Mixed 2D and 3D Electrodes. *ACS Applied Energy Materials* **2020**, *3*, 8402–8409.

(7) Hart, R. W.; White, H. S.; Dunn, B.; Rolison, D. R. 3-D Microbatteries. *Electrochemistry Communications* **2003**, *5* (2), 120–123. https://doi.org/10.1016/S1388-2481(02)00556-8.

(8) Baggetto, L.; Niessen, R. A. H.; Roozeboom, F.; Notten, P. H. L. High Energy Density All-Solid-State Batteries: A Challenging Concept Towards 3D Integration. *Adv. Funct. Mater.* **2008**, *18* (7), 1057–1066. https://doi.org/10.1002/adfm.200701245.

(9) Oudenhoven, J. F. M.; Baggetto, Loïc.; Notten, P. H. L. All-Solid-State Lithium-Ion Microbatteries: A Review of Various Three-Dimensional Concepts. *Adv. Energy Mater.* **2011**, *1* (1), 10–33. https://doi.org/10.1002/aenm.201000002.

(10) Hur, J. I.; Smith, L. C.; Dunn, B. High Areal Energy Density 3D Lithium-Ion Microbatteries. *Joule* **2018**, *2* (6), 1187–1201. https://doi.org/10.1016/j.joule.2018.04.002.

(11) Narita, K.; Saccone, M. A.; Sun, Y.; Greer, J. R. Additive Manufacturing of 3D Batteries: A Perspective. *Journal of Materials Research* **2022**, *37* (9), 1535–1546. https://doi.org/10.1557/s43578-022-00562-w.

(12) Pang, Y.; Cao, Y.; Chu, Y.; Liu, M.; Snyder, K.; MacKenzie, D.; Cao, C. Additive Manufacturing of Batteries. *Adv. Funct. Mater.* **2020**, *30* (1), 1906244. https://doi.org/10.1002/adfm.201906244.

(13) Gulzar, U.; Glynn, C.; O'Dwyer, C. Additive Manufacturing for Energy Storage: Methods, Designs and Material Selection for Customizable 3D Printed Batteries and Supercapacitors. *Current Opinion in Electrochemistry* **2020**, *20*, 46–53. https://doi.org/10.1016/j.coelec.2020.02.009.

(14) Lyu, Z.; Lim, G. J. H.; Koh, J. J.; Li, Y.; Ma, Y.; Ding, J.; Wang, J.; Hu, Z.; Wang, J.; Chen, W.; Chen, Y. Design and Manufacture of 3D-Printed Batteries. *Joule* **2021**, *5* (1), 89–114. https://doi.org/10.1016/j.joule.2020.11.010.

(15) Long, J. W.; Dunn, B.; Rolison, D. R.; White, H. S. 3D Architectures for Batteries and Electrodes. *Adv. Energy Mater.* **2020**, *10* (46), 2002457. https://doi.org/10.1002/aenm.202002457.

(16) Arthur, T. S.; Bates, D. J.; Cirigliano, N.; Johnson, D. C.; Malati, P.; Mosby, J. M.; Perre, E.; Rawls, M. T.; Prieto, A. L.; Dunn, B. Three-Dimensional Electrodes and Battery Architectures. *MRS Bull.* **2011**, *36* (7), 523–531. https://doi.org/10.1557/mrs.2011.156.

(17) Yang, L. Harnessing the Surface Structure to Enable High-Performance Cathode Materials for Lithium-Ion Batteries. *Chem Soc Rev* **2020**, 14.

(18) Dong, Y. Z.; Zhao, Y. M.; Duan, H. Crystal Structure and Lithium Electrochemical Extraction Properties of Olivine Type LiFePO4. *Materials Chemistry and Physics* **2011**, *129* (3), 756–760. https://doi.org/10.1016/j.matchemphys.2011.04.076.

(19) Zhang, W.-J. Structure and Performance of LiFePO4 Cathode Materials: A Review. *Journal of Power Sources* **2011**, *196* (6), 2962–2970. https://doi.org/10.1016/j.jpowsour.2010.11.113.

(20) Sun, K.; Wei, T.-S.; Ahn, B. Y.; Seo, J. Y.; Dillon, S. J.; Lewis, J. A. 3D Printing of Interdigitated Li-Ion Microbattery Architectures. *Adv. Mater.* **2013**, *25* (33), 4539–4543. https://doi.org/10.1002/adma.201301036.

(21) Moitzheim, S.; Put, B.; Vereecken, P. M. Advances in 3D Thin-Film Li-Ion Batteries. *Adv. Mater. Interfaces* **2019**, *6* (15), 1900805. https://doi.org/10.1002/admi.201900805.

(22) Létiche, M.; Eustache, E.; Freixas, J.; Demortière, A.; De Andrade, V.; Morgenroth, L.; Tilmant, P.; Vaurette, F.; Troadec, D.; Roussel, P.; Brousse, T.; Lethien, C. Atomic Layer Deposition of Functional Layers for on Chip 3D Li-Ion All Solid State Microbattery. *Adv. Energy Mater.* **2017**, *7* (2), 1601402. https://doi.org/10.1002/aenm.201601402.

(23) Pearse, A.; Schmitt, T.; Sahadeo, E.; Stewart, D. M.; Kozen, A.; Gerasopoulos, K.; Talin, A. A.; Lee, S. B.; Rubloff, G. W.; Gregorczyk, K. E. Three-Dimensional Solid-State Lithium-Ion

Batteries Fabricated by Conformal Vapor-Phase Chemistry. *ACS Nano* **2018**, *12* (5), 4286–4294. https://doi.org/10.1021/acsnano.7b08751.

(24) Egorov, V.; Gulzar, U.; Zhang, Y.; Breen, S.; O'Dwyer, C. Evolution of 3D Printing Methods and Materials for Electrochemical Energy Storage. *Adv. Mater.* **2020**, *32* (29), 2000556. https://doi.org/10.1002/adma.202000556.

(25) Costa, C. M.; Gonçalves, R.; Lanceros-Méndez, S. Recent Advances and Future Challenges in Printed Batteries. *Energy Storage Materials* **2020**, *28*, 216–234. https://doi.org/10.1016/j.ensm.2020.03.012.

(26) Zhao, J.; Lu, H.; Zhao, X.; Malyi, O. I.; Peng, J.; Lu, C.; Li, X.; Zhang, Y.; Zeng, Z.; Xing, G.; Tang, Y. Printable Ink Design towards Customizable Miniaturized Energy Storage Devices. *ACS Materials Lett.* **2020**, *2* (9), 1041–1056. https://doi.org/10.1021/acsmaterialslett.0c00176.

(27) Saha, B.; Goebel, K. Modeling Li-Ion Battery Capacity Depletion in a Particle Filtering Framework. **2009**.

(28) Roberts, M.; Johns, P.; Owen, J.; Brandell, D.; Edstrom, K.; El Enany, G.; Guery, C.; Golodnitsky, D.; Lacey, M.; Lecoeur, C.; Mazor, H.; Peled, E.; Perre, E.; Shaijumon, M. M.; Simon, P.; Taberna, P.-L. 3D Lithium Ion Batteries—from Fundamentals to Fabrication. *J. Mater. Chem.* **2011**, *21* (27), 9876. https://doi.org/10.1039/c0jm04396f.

(29) Ashby, D. S.; Cardenas, J.; Bhandarkar, A. S.; Cook, A. W.; Talin, A. A. Modifying Ionogel Solid-Electrolytes for Complex Electrochemical Systems. *ACS Appl. Energy Mater.* **2022**, acsaem.2c02085. https://doi.org/10.1021/acsaem.2c02085.

(30) Ashby, D. S.; DeBlock, R. H.; Lai, C.-H.; Choi, C. S.; Dunn, B. S. Patternable, Solution-Processed Ionogels for Thin-Film Lithium-Ion Electrolytes. *Joule* **2017**, *1* (2), 344–358. https://doi.org/10.1016/j.joule.2017.08.012.

(31) McNeil, P.; Guillemin, T.; Fox, M.; Le Bideau, J.; Dunn, B. Characterization of Fragility in Silica-Based Ionogels. *J. Phys. Chem. C* **2022**, acs.jpcc.2c05911. https://doi.org/10.1021/acs.jpcc.2c05911.

(32) Mitra, S.; Cerclier, C.; Berrod, Q.; Ferdeghini, F.; de Oliveira-Silva, R.; Judeinstein, P.; le Bideau, J.; Zanotti, J.-M. Ionic Liquids Confined in Silica Ionogels: Structural, Thermal, and Dynamical Behaviors. *Entropy* **2017**, *19* (4), 140. https://doi.org/10.3390/e19040140.

(33) Dai, S.; Ju, Y. H.; Gao, H. J.; Lin, J. S.; Pennycook, S. J.; Barnes, C. E. Preparation of Silica Aerogel Using Ionic Liquids as Solvents. *Chem. Commun.* **2000**, No. 3, 243–244. https://doi.org/10.1039/a907147d.

(34) Chen, N.; Zhang, H.; Li, L.; Chen, R.; Guo, S. Ionogel Electrolytes for High-Performance Lithium Batteries: A Review. *Adv. Energy Mater.* **2018**, *8* (12), 1702675. https://doi.org/10.1002/aenm.201702675.

(35) Fu, K.; Wang, Y.; Yan, C.; Yao, Y.; Chen, Y.; Dai, J.; Lacey, S.; Wang, Y.; Wan, J.; Li, T.; Wang, Z.; Xu, Y.; Hu, L. Graphene Oxide-Based Electrode Inks for 3D-Printed Lithium-Ion Batteries. *Adv. Mater.* **2016**, *28* (13), 2587–2594. https://doi.org/10.1002/adma.201505391.

(36) Delannoy, P.-E.; Riou, B.; Brousse, T.; Le Bideau, J.; Guyomard, D.; Lestriez, B. Ink-Jet Printed Porous Composite LiFePO 4 Electrode from Aqueous Suspension for Microbatteries. *Journal of Power Sources* **2015**, *287*, 261–268. https://doi.org/10.1016/j.jpowsour.2015.04.067.

Chapter 4. Ion Transport in Printed Structures

An important consideration for designing 3D battery architectures is the minor structures or building blocks that make up the larger electrode arrangement. While many aspects of the electrode design have been previously studied including proportion sizes, spacing and aspect ratios - the individual elements are less commonly expanded upon. By studying individual components of an overall electrode design, a better use of the micro-battery areal footprint can be determined and give insight into optimized electrode designs. In this chapter, four building block structures- a cross, box, line, and layer, were identified from a larger lattice structure and characterized. This study demonstrated the importance of utilizing a continuously printed structure to minimize the printed electrode inconsistencies and discontinuities within the Direct Ink Writing process.

Chapter 4.1. Introduction

With the continued rise of the Internet of Things (IoT) and the miniaturization of consumer electronics, there has been a drive to redesign their power supply.[1,2] As discussed in chapter 3, IoT technology relies on being able to continually process new information and provide communications, thus requiring a high performance power supply. Micro-batteries are a leading candidate for such power supplies due to their ability to store energy and provide a steady output of power. However, while lithium ion batteries (LIBs) have high energy densities, they do not have the power densities needed to support many consumer electronic devices. The traditional planar designs of these batteries lead to limitations in their performance metrics.[3,4]

Utilizing non-planar electrode architectures has proven to be a promising means of improving device performance by decoupling energy and power densities through use of the z-direction or height. This enables diffusion distances to be kept short, thus enabling high power. Increasing thickness leads to greater loading of active material and high energy density.[5,6] Some key features when considering 3D electrodes are the chosen material, the fabrication process, and the type of architecture. For the research reported in this chapter, Lithium Iron Phosphate (LFP) is being used as the cathode material, thus providing an extension of the work in chapter 3.

LFP is a common cathode material with a reasonable theoretical capacity (170mAh/g) and long cycle life. Its stability during charging and discharging has been shown at a variety of rates and operating conditions.[7,8] LFP is known for being a low cost material, using less critical materials than other common battery materials such as Lithium Cobalt Oxide (LCO) or Lithium Nickel Manganese Cobalt Oxide (NMC), which will help reduce the cost of the final device.[8–10] For use in a 3D architecture, another desirable quality of LFP is its low volume expansion under charging and discharging. The low volume expansion is ideal for multidimensional electrodes to minimize mechanical stress in the device during operation.[11–14]

The most common 3D electrode architectures fall into three categories- interdigitated, concentric, and aperiodic.[15,16] These terms describe specific electrode geometry and, to some degree, how the two electrode architectures fit together.[17] Each multidimensional electrode can then be described by their individual architecture such as a pillar array or 3D lattice. There are a number of considerations when designing an electrode architecture with one of the most common being the distribution of the architectural elements.[18–22] These minor architectures or building blocks can be used as a point of reference for scaling to larger areal footprints to describe limitations in the electrode design.[3]

3D electrode architectures can be fabricated through a variety of different fabrication techniques, however the technique chosen dictates the flexibility of the electrode design. Some of the more traditional microfabrication techniques include atomic layer deposition, chemical vapor deposition, photolithography, etching and templating.[3,23–25] These methods have shown the ability to closely tune electrode designs, however they can be costly to implement. Additive manufacturing methods have more recently been studied for battery microfabrication applications. Many additive manufacturing methods are considered to be a cost effective alternative for large scale battery development and are characterized by their bottom up approach.

Among the additive manufacturing techniques available, 3D printing methods have been the most easily adapted for battery materials. Some of these techniques include fused deposition modeling, stereolithography, inkjet printing and direct ink writing. There are benefits and limitations to all of these techniques, including such factors as low waste, having a range of compatible materials, printing resolution, and flexibility of design. The most versatile of the printing techniques is direct ink writing (DIW), which is the microfabrication technique of choice in this study. While there have been reports of design versatility with the DIW process, most designs normally utilize connected architectures because of the needed ink requirements for this process. However, limitations in rheological properties make the fabrication of smaller self-sustaining architectures such as pillars, difficult to achieve with these inks. Many developed battery inks have thixotropic qualities, meaning they maintain uniform viscosity under a constant shear rate, which is not conducive to having a stoppage in ink printing and limits the ability to create unique printed features.[11,17,26–28]

One of the biggest differences between traditional microfabrication techniques and additive manufacturing ones, is the ability to make self-sustaining minor structures that are continuous processes.[11,26] In the case of direct ink writing, this means that all the pieces will be connected and layered, so all of the minor architectures are important for the continuity of the electrode itself.[28] The goal of this work is to characterize the building blocks of the larger lattice geometry and determine, if any, the limitations of DIW in this printed structure.

Chapter 4.2. Experimental Methods

Materials

Lithium Iron Phosphate (American Elements), C65 carbon black (Timrex), and poly(vinylidene fluoride) (Solvay) were used as received. Lithium perchlorate, Ethylene Carbonate, and Dimethyl Carbonate (Sigma-Aldrich) were anhydrous and stored in an Argon filled glove box before use. Conductive silver paste (Ted Pella) was stored in a freezer (-18°C) until use.

Printed Cathode Structures

Ink for printing 3D electrodes was prepared from Lithium Iron Phosphate, LFP (American Elements), C65 carbon black and poly(vinylidene fluoride) (PVdF) in N-methyl-2-pyrrolidone (NMP) mixed using a Thinky Mixer. Prepared inks were loaded into a syringe with a 200µm nozzle, and electrodes printed with a Hyrel Printer. The cathode architectures were printed using dimensions from a lattice with 200µm spacing. The structures were printed onto aluminum foil or glass. All printed electrodes were dried by covering with a petri dish at ambient conditions. Once dried, printed electrodes were further dried in a vacuum oven for 1 hour at 110°C before assembling into a coin cell or flooded cell for electrochemical testing.

Microstructure Characterization of Printed Electrodes

Scanning Electron Microscopy (SEM) was done using an FEI Nova 230 Nano scanning electron microscope. Both planar and cross-section of tape cast and printed electrodes SEM images were obtained. SEM images were used to qualitatively determine the porosity of prepared electrodes using ImageJ analysis.

Electrochemical Testing

For structures printed on aluminum foil, electrochemical characterization was done in both a coin-cell and flooded cell with a lithium metal counter and reference electrode, and 1M $LiClO_4$ in EC:DMC (1:1 by volume) as the electrolyte. Testing in the flooded cell, and assembly of the coin-cells were done in an argon-filled glovebox. Cyclic voltammetry (CV) and galvanostatic charge-discharge (GV) measurements were made from 2.8 to 4V vs Li/Li^+. Galvanostatic intermittent titration technique (GITT) measurements were carried out using a VMP potentiostat/galvanostat (Bio-Logic). More details on GITT and GV can be found in chapter 2 on electrochemical characterization techniques

Electrochemical Impedance Spectroscopy (EIS) measurements were taken using a Solatron Impedance Analyzer. Silver contacts were painted onto the printed structures and copper wires were used to complete the circuit for the EIS measurement. EIS was taken both with and without electrolyte to determine the mixed ionic-electronic and electronic conductivity respectively. Several measurements were taken from varying points on the printed structures. The resistance and conductivity were then determined from the data in a Nyquist plot. Electrochemical tests used in this chapter are explained in more detail in chapter 2.

Chapter 4.3. Results and Discussion

The larger 3D lattice architecture previously studied in chapter 3, could be broken down into its building blocks and studied. The minor architectures identified are denoted as a cross, box, line and layer (Figure 4.1.(a)). These smaller architectures mimic different junctions and components that exist in the larger lattice architecture. The spacing and thickness of the printed lines is based on lattices printed with a $200\mu m$ nozzle and $200\mu m$ spacing. The lattice is comprised of overlapping single layers rotated at 90º. The layer architecture was an identified structure to understand the contribution of each layer to the overall lattice design. The cross and box are representative of the overlapping intersections of the printed layers. The cross represents the junction of two overlapping lines. Comparatively, the box is a more complex structure comprised of two overlapping crosses, and forms the repeating square present throughout the lattice structure. The line is the simplest of the building blocks showing one rotation of the printer nozzle. For a lattice with the dimensions noted above, a single layer structure is comprised of 21 line structures.

Initial electrochemical testing included cyclic voltammetry and galvanostatic charging/discharging (GV). For GV testing the capacity is reported normalized to the areal footprint of each of the printed structures (Figure 4.1).

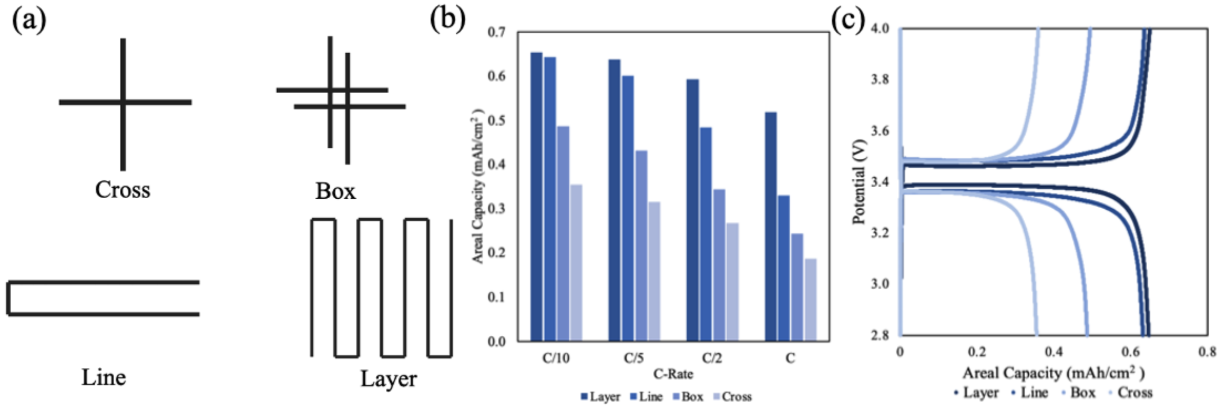

Figure 4.1. (a) Representations of tested lattice components (i.e., cross, box, line, and layer). (b) Areal capacity at various charging rates and (c) galvanostatic charge/discharge curve at a rate of C/10 for the shown lattice components.

A comparison of the areal capacity for all the structures at various C-rates (Figure 4.1.(b)) indicates that the layer and line configurations have the highest areal capacity, at just greater than 0.6mAh/cm^2. The layered structure was able to maintain more of its capacity at the faster charging rates, maintaining 79% of its capacity when going from a rate of C/10 to C. The areal capacity of the single layer lattice does scale when compared to the 2 and 4 layer lattices that had areal capacities of 1.5mAh/cm^2 and 3.0mAh.cm^2 respectively (Table 3.3). This shows that the architectural building blocks of the lattice can be used to predict the experimental performance of the larger architecture, similar to what was shown in Figure 3.9(a).[3,26] The remaining printed structures only maintained approximately 50% of their initial capacity at the faster C-rates. Lastly, the overpotential is lowest for the single layer structure compared to the other three simple structures which suggests there is less interfacial resistance in this structure compared to the others.

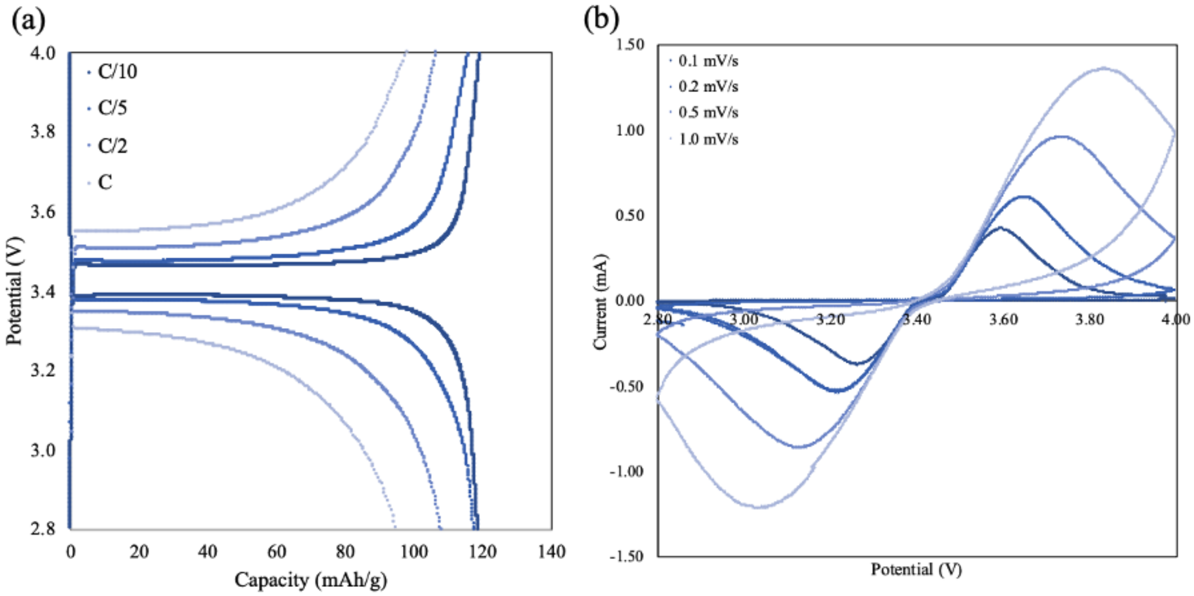

Figure 4.2. For the layer structure (a) galvanostatic charge/discharge curves and (b) cyclic voltammetry curves at various charging and scan rates respectively in the voltage window 2.8V-4V (vs. Li/Li$^+$).

In evaluating the layered structure at different C-rates, there is some polarization observed in the charging and discharging curves at higher rates, as indicated by the deviation in potential from the operating potential of LFP (3.4V vs Li/Li$^+$).[7,29,30] The polarization can be more clearly demonstrated in the GV by observing the charge/discharge curves at C-rates of C/10 and C/5, where both discharge specific capacities are the same (~120mAh/g). However, at C/5 there is a decrease in the coulombic efficiency, and an increase in the overpotential, suggesting that this increase in polarization can be attributed to internal resistance, perhaps from charge transfer resistance. This polarization is also observed in the cyclic voltammogram obtained by CV, from the increase in separation of the redox peaks at faster scan rates.[29,31]

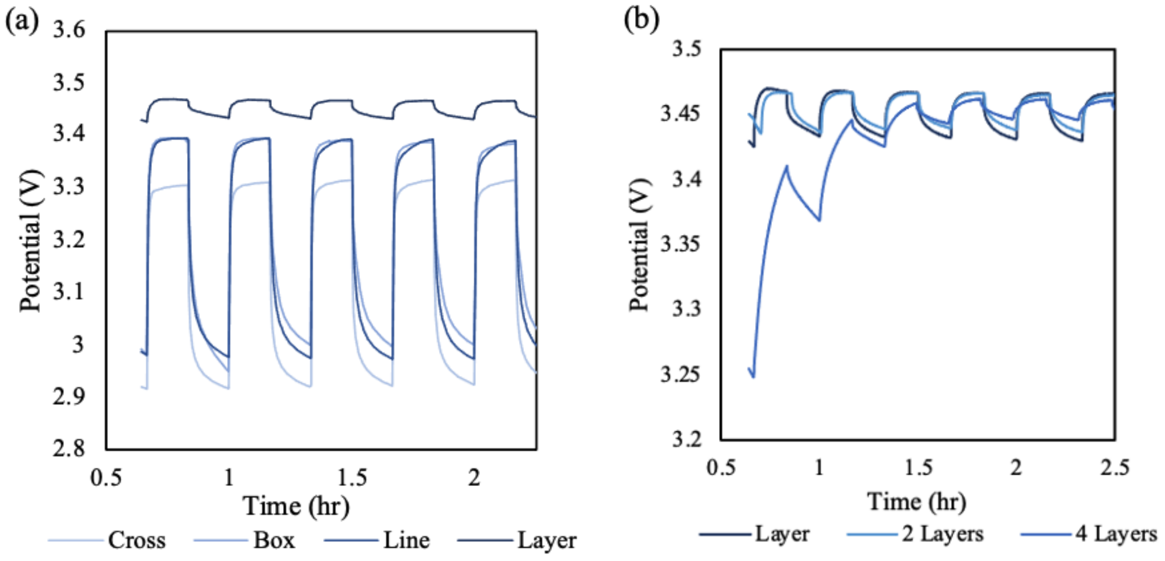

Figure 4.3. (a) Galvanostatic Intermittent Titration Technique (GITT) profiles for the different lattice building blocks, and (b) profiles for multiple layered lattices. Reported conductivity and resistivity values were calculated for the various lattice components.

The GITT in Figure 4.3 demonstrates the different voltage responses for each of the lattice building blocks and multilayer samples. As described in chapter 2, the potential drop during the relaxation period or overpotential divided by the applied current gives the internal resistance experienced at the electrode (Eqn. 2.5).[32,33] The potential drop in the layer architecture is much less than that for any of the other lattice building blocks and this resistance is also over a much larger area. Comparing the areal internal resistances for these four structures, the internal resistance for the layered structure ($1.9\text{x}10^3$ Ohm cm^{-2}) is two orders of magnitude less than for the box, layer, and line structures that had resistances on the order of 10^5-10^6 Ohm cm^{-2}.

The overpotential observed by GITT continues to decrease as the number of lattice layers is increased (Figure 4.3.(b)). Comparing the lattices with multiple layers to the single layer lattice, the 4 layer lattice had the smallest overpotential (20mV) and the single layer an overpotential of 30mV (Table 4.1.). While the single layer and 2 layer lattice had the same overpotential, the 2 layer lattice covers a greater area than the single layer resulting in a lower internal areal resistance. The calculated conductivity for the building blocks and the multilayered lattices were in the same order of magnitude (10^3 S/cm). This is a mixed conductivity value because there are contributions from the electrode and the electrolyte (1M $LiClO_4$ in EC:DMC) as the GITT testing was done using a flooded cell arrangement. The layer structure had the highest conductivity of all the building block structures at 1.52×10^{-3} S/cm. The conductivity increased in multilayered lattices where it plateaued at 2.28×10^{-3} S/cm. The calculated internal resistance and conductivity by GITT are reported in Table 4.1.

Table 4.1. Overpotential, internal areal resistance and mixed conductivity of building block structures, 2 and 4 layer lattices measured by GITT in a flooded half-cell.

Structure	**Overpotential (V)**	**Internal Areal Resistance ($\Omega\ cm^{-2}$)**	**Mixed Conductivity (S/cm)**
Cross	0.39	1.60E+06	1.35E-03
Box	0.39	7.99E+05	6.73E-04
Line	0.41	5.60E+05	1.19E-03
Layer	0.03	3.84E+03	1.52E-03
2 Layers	0.03	3.15E+03	1.52E-03
4 Layers	0.02	2.10E+03	2.28E-03

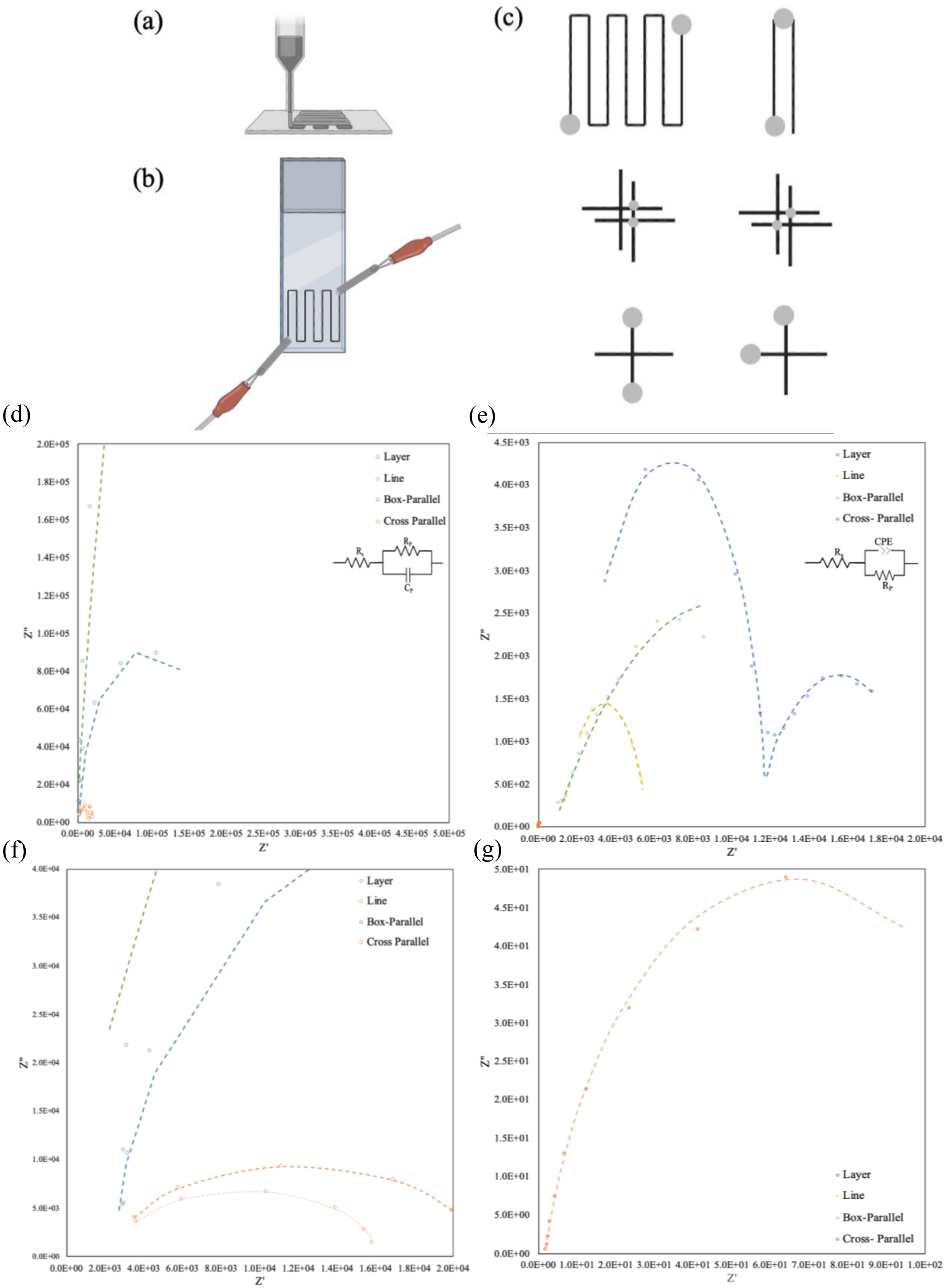
(a)
(b)
(c)
(d)
Layer
Line
Box-Parallel
Cross Parallel
R_s
R_p
C_p
Z"
Z'
2.0E+05
1.8E+05
1.6E+05
1.4E+05
1.2E+05
1.0E+05
8.0E+04
6.0E+04
4.0E+04
2.0E+04
0.0E+00
0.0E+00 5.0E+04 1.0E+05 1.5E+05 2.0E+05 2.5E+05 3.0E+05 3.5E+05 4.0E+05 4.5E+05 5.0E+05
(e)
Layer
Line
Box-Parallel
Cross- Parallel
R_s
CPE
R_p
Z"
Z'
4.5E+03
4.0E+03
3.5E+03
3.0E+03
2.5E+03
2.0E+03
1.5E+03
1.0E+03
5.0E+02
0.0E+00
0.0E+00 2.0E+03 4.0E+03 6.0E+03 8.0E+03 1.0E+04 1.2E+04 1.4E+04 1.6E+04 1.8E+04 2.0E+04
(f)
Layer
Line
Box-Parallel
Cross Parallel
Z"
Z'
4.0E+04
3.5E+04
3.0E+04
2.5E+04
2.0E+04
1.5E+04
1.0E+04
5.0E+03
0.0E+00
0.0E+00 2.0E+03 4.0E+03 6.0E+03 8.0E+03 1.0E+04 1.2E+04 1.4E+04 1.6E+04 1.8E+04 2.0E+04
(g)
Layer
Line
Box-Parallel
Cross- Parallel
Z"
Z'
5.0E+01
4.5E+01
4.0E+01
3.5E+01
3.0E+01
2.5E+01
2.0E+01
1.5E+01
1.0E+01
5.0E+00
0.0E+00
0.0E+00 1.0E+01 2.0E+01 3.0E+01 4.0E+01 5.0E+01 6.0E+01 7.0E+01 8.0E+01 9.0E+01 1.0E+02

Figure 4.4. Representation of (a) printed structures on glass and (b) an example of placement of silver contacts for impedance measurement. (c) Graphical representations, clockwise from the upper left corner, are shown of the silver contact placements for a layer, line, box (perpendicular), cross (perpendicular), cross (parallel), and box (parallel). Measured Nyquist impedance spectra of structures printed on glass, (d) without and (e) with electrolyte and view of the origin for structures (f) without and (g) with electrolyte. A fit for the Nyquist plot data was determined (dashed line) and the representative circuits are shown respectively.

As described in chapter 2.2, the Nyquist plot can be used to calculate the conductivity and resistance of the measured device (Eqn. 2.4). The Nyquist plots for all the building block architectures are shown in Figure 4.4 both with and without electrolyte. Figure 4.4(d) and 4.4(e) show the representative plots for the electronic (without electrolyte) and mixed (with electrolyte) resistance, respectively, for all of the building block structures. The samples that had a continuously printed structure (the layer and line) have smaller measured resistance over their areal footprint (Table 4.2.). EIS measurements of the two other structures, the box and the cross, involved the use of the two contact locations as shown in Figure 4.4.(c). The parallel contacts are placed on a continuously printed line, while the perpendicular contacts were placed on two discontinuously printed lines. To create the box and cross structures, the continuous DIW process is interrupted to be able to achieve that architecture. The discontinuity of the printed overlapping lines are shown in the SEM images in Figure 4.6. In doing so, there are more disconnected points of contact between the printed lines. For the cross structure the measured electronic resistance (Table 4.2.) increased by an order of magnitude compared to the measurement using parallel contacts ($4.14\text{x}10^4$ Ohm cm^{-2}) versus perpendicular contacts ($4.71\text{x}10^5$ Ohm cm^{-2}).

The representative circuit for the Nyquist plot was determined in order to achieve a better understanding of the dominating current response among the different building blocks. For both plots with and without the inclusion of electrolyte, there is an initial resistance at the higher frequencies, seen in the shift to a non-zero value on the real axis. This is followed by capacitive behavior at lower frequencies before becoming resistive again.[34–36] While there are similar capacitor like behaviors for both the electronic and mixed system, the mixed system deviates from ideal capacitor behavior. The deviation from ideal capacitor behavior is represented by a constant phase element (CPE) and the impedance value is fitted by[34,37,38]:

$$Z_{CPE} = \frac{1}{Q(i\omega)^{\alpha}} \qquad \textit{(Eqn. 2.1.)}$$

where Q is the CPE parameter, and α is the CPE exponent. CPEs have been attributed to many things including, but not limited to, the presence of a electrical double layer and the electrode geometry.[37,38]

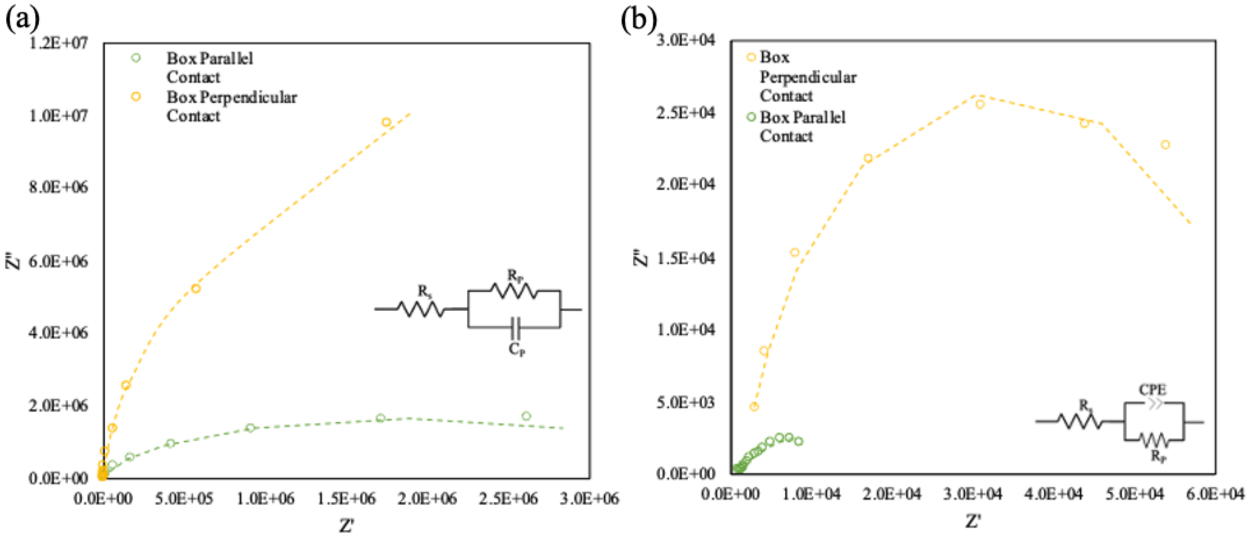

Figure 4.5. Measured impedance of the printed box structure on glass, (a) without and (b) with electrolyte. Two sets of impedance measurements were taken where the silver contacts were placed on the same printed line or side of the box (Box Parallel Contact) and on opposite printed lines or diagonal corners of the box (Box Perpendicular Contact). A fit for the impedance data was determined (dashed line) and the representative circuits are shown respectively.

Figure 4.5 shows the isolated Nyquist plots for the box structure with either the parallel or perpendicular contacts. EIS was done both without (Figure 4.5.(a)) and with (Figure 4.5(b)) electrolyte. Regardless of the electrolyte used, the perpendicularly placed contacts had a higher initial resistance compared to the parallel contacts. For the electronic resistance, the measured values were both more resistive than the other building blocks, with resistances of 1.28x10^7 Ohm cm^{-2} and 1.05x10^7 Ohm cm^{-2} for the perpendicular and parallel contacts respectively. For the calculated mixed resistance, the resistance difference based on contact placement is more pronounced. For perpendicular contact placement, the resistance was 1.23x10^6 Ohm cm^{-2} and for parallel contacts the resistance was an order of magnitude less (2.86x10^5 Ohm cm^{-2}).

The difference in measured resistances can be attributed to the distance between the contacts, overlap of the printed lines, and discontinuity of the printing. As mentioned previously, the same behavior can be observed in the printed cross structure where there is an increase in resistance over the areal footprint when comparing perpendicular to parallel points of contact. A summary of the resistance and conductivity measurements both with and without the electrolyte are recorded in Table 4.2. normalized to the areal footprint of the structure. The resistance values show that over the covered areal footprint, the layer structure has the lowest electronic and mixed resistances, followed by the line structure. The same trend was seen in the calculated interfacial resistances from GITT (Table 4.1).

While one of the reasons for the larger increase in resistance in the box and cross structure comes from the overlapping lines, the same trend is not seen as significantly with the multilayered lattices. This is because with the multilayered lattices, the structure is continuously printed and there is no disconnect between the layers. For the box and cross, the printing process is not continuous. Because of the lack of discontinuity, the printed lattices mentioned previously are a singular electronic structure.

Table 4.2. Summary of structure resistance and conductivity measurements, both electronic (without electrolyte) and mixed (with electrolyte) normalized to area.

Structure	**Contact Placement**	**Electronic Resistance (Ohm/cm^2)**	**Electronic Conductivity (S/cm)**	**Mixed Resistance (Ohm/cm^2)**	**Mixed Conductivity (S/cm)**
Layer	-	8.23E+03	3.11E-04	5.03E+03	2.59E+01
Line	-	2.01E+04	1.32E-03	5.20E+04	1.28E-02
Box	Perpendicular	1.28E+07	3.42E-06	1.23E+06	5.01E-04
	Parallel	1.05E+07	3.42E-06	2.86E+05	1.88E-03
Cross	Perpendicular	4.71E+05	1.74E-04	1.62E+06	1.26E-03
	Parallel	4.14E+04	1.98E-03	1.58E+05	1.36E-02

As stated previously, the comparison of these structures highlights the importance of having continuously printed DIW electrodes over unique features that require printing to be discontinuous. SEM images showed that the structures that required the ink flow to stop in order to finish printing the rest of the architecture exhibited inhomogeneities in the printed line thickness and the line width (figure 4.6). Having a continuous flow of ink is an important consideration for both ink development and the DIW printing process. Inks are made to have thixotropic properties, or to be able to maintain uniform flow and viscosity at a constant shear rate.[24,25] In this case, the printer uses mechanical extrusion, where the syringe plunger is set to a specific rate to help control pressure at the nozzle tip. When the flow of ink is suddenly stopped and restarted, there is an increased output of ink from the build-up of pressure at the nozzle tip.

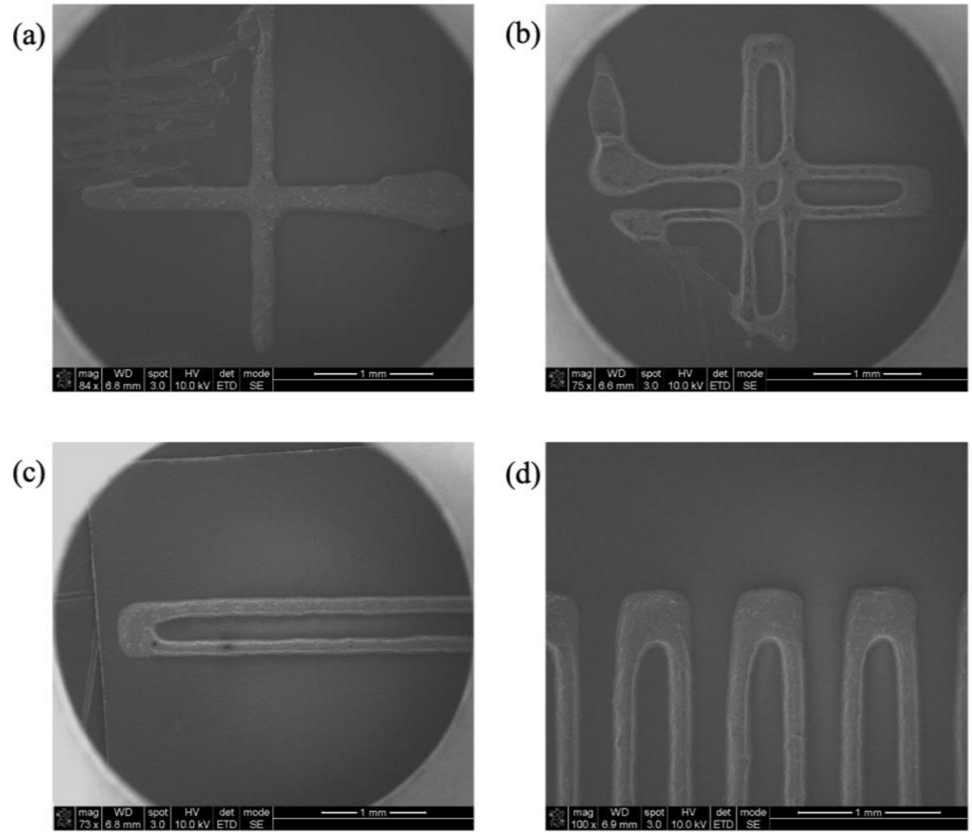

Figure 4.6. SEM of printed (a) cross, (b) box, (c) line, and (d) layer structures, scale bar 1mm.

Chapter 4.4. Conclusion

In this chapter, building block structures that make up the overall lattice architecture described in the previous chapter were identified and characterized. The layered structure demonstrated the highest areal capacities (normalized to structure areal footprint), capacity retention, conductivity, and lowest interfacial resistance compared to the other identified structures. The testing of these architectures also emphasized the importance of having a continuously printed structure when utilizing the DIW additive manufacturing process because the thixotropic characteristics of the ink are meant for continuous ink flow. This is especially clear when observing the uniformity of the printed structures by SEM, and from the increased resistances in the printed structures which were not printed continuously - the box and the cross. The performance of the complete lattice electrode depends upon the electrochemical characteristics of each of the building blocks. In future work, it should be possible to determine the electrochemical properties of the 3D lattice electrode described in Chapter 3 by summing the contributions of each of the building blocks. The initial observation on the importance of having a continuous structure that spans the allocated areal footprint provides a basis for understanding the 3D lattice architecture.

Chapter 4.5. References

(1) Li, S.; Xu, L. D.; Zhao, S. The Internet of Things: A Survey. *Inf Syst Front* **2015**, *17* (2), 243–259. https://doi.org/10.1007/s10796-014-9492-7.

(2) Xu, L. D.; He, W.; Li, S. Internet of Things in Industries: A Survey. *IEEE Trans. Ind. Inf.* **2014**, *10* (4), 2233–2243. https://doi.org/10.1109/TII.2014.2300753.

(3) Ashby, D. S.; Choi, C. S.; Edwards, M.; Talin, A. A.; White, H. S.; Dunn, B. S. High-Performance Solid-State Lithium-Ion Battery with Mixed 2D and 3D Electrodes. *ACS Applied Energy Materials* **2020**, *3*, 8402–8409.

(4) Hart, R. W.; White, H. S.; Dunn, B.; Rolison, D. R. 3-D Microbatteries. *Electrochemistry Communications* **2003**, *5* (2), 120–123. https://doi.org/10.1016/S1388-2481(02)00556-8.

(5) Baggetto, L.; Niessen, R. A. H.; Roozeboom, F.; Notten, P. H. L. High Energy Density All-Solid-State Batteries: A Challenging Concept Towards 3D Integration. *Adv. Funct. Mater.* **2008**, *18* (7), 1057–1066. https://doi.org/10.1002/adfm.200701245.

(6) Oudenhoven, J. F. M.; Baggetto, Loïc.; Notten, P. H. L. All-Solid-State Lithium-Ion Microbatteries: A Review of Various Three-Dimensional Concepts. *Adv. Energy Mater.* **2011**, *1* (1), 10–33. https://doi.org/10.1002/aenm.201000002.

(7) Erabhoina, H.; Thelakkat, M. Tuning of Composition and Morphology of LiFePO4 Cathode for Applications in All Solid-State Lithium Metal Batteries. *Sci Rep* **2022**, *12* (1), 5454. https://doi.org/10.1038/s41598-022-09244-3.

(8) Li, Z.; Zhang, D.; Yang, F. Developments of Lithium-Ion Batteries and Challenges of LiFePO4 as One Promising Cathode Material. *J Mater Sci* **2009**, *44* (10), 2435–2443. https://doi.org/10.1007/s10853-009-3316-z.

(9) *FACT SHEET: Securing a Made in America Supply Chain for Critical Minerals*; Brief; The White House, 2022. https://www.whitehouse.gov/briefing-room/statements-releases/2022/02/22/fact-sheet-securing-a-made-in-america-supply-chain-for-critical-minerals/.

(10) *CRITICAL MINERALS AND MATERIALS PROGRAM*; National Energy Technology Laboratory. https://netl.doe.gov/resource-sustainability/minerals-and-materials/program-overview/background.

(11) Lyu, Z.; Lim, G. J. H.; Koh, J. J.; Li, Y.; Ma, Y.; Ding, J.; Wang, J.; Hu, Z.; Wang, J.; Chen, W.; Chen, Y. Design and Manufacture of 3D-Printed Batteries. *Joule* **2021**, *5* (1), 89–114. https://doi.org/10.1016/j.joule.2020.11.010.

(12) Dong, Y. Z.; Zhao, Y. M.; Duan, H. Crystal Structure and Lithium Electrochemical Extraction Properties of Olivine Type LiFePO4. *Materials Chemistry and Physics* **2011**, *129* (3), 756–760. https://doi.org/10.1016/j.matchemphys.2011.04.076.

(13) Zhang, W.-J. Structure and Performance of LiFePO4 Cathode Materials: A Review. *Journal of Power Sources* **2011**, *196* (6), 2962–2970. https://doi.org/10.1016/j.jpowsour.2010.11.113.

(14) Sun, K.; Wei, T.-S.; Ahn, B. Y.; Seo, J. Y.; Dillon, S. J.; Lewis, J. A. 3D Printing of Interdigitated Li-Ion Microbattery Architectures. *Adv. Mater.* **2013**, *25* (33), 4539–4543. https://doi.org/10.1002/adma.201301036.

(15) Long, J. W.; Dunn, B.; Rolison, D. R.; White, H. S. 3D Architectures for Batteries and Electrodes. *Adv. Energy Mater.* **2020**, *10* (46), 2002457. https://doi.org/10.1002/aenm.202002457.

(16) Long, J. W.; Dunn, B.; Rolison, D. R.; White, H. S. Three-Dimensional Battery Architectures. *Chem. Rev.* **2004**, *104* (10), 4463–4492. https://doi.org/10.1021/cr020740l.

(17) Narita, K.; Saccone, M. A.; Sun, Y.; Greer, J. R. Additive Manufacturing of 3D Batteries: A Perspective. *Journal of Materials Research* **2022**, *37* (9), 1535–1546. https://doi.org/10.1557/s43578-022-00562-w.

(18) Cirigliano, N.; Sun, G.; Membreno, D.; Malati, P.; Kim, C. J.; Dunn, B. 3D Architectured Anodes for Lithium-Ion Microbatteries with Large Areal Capacity. *Energy Technology* **2014**, *2* (4), 362–369. https://doi.org/10.1002/ente.201402018.

(19) Wang, Z.; Ni, J.; Li, L.; Lu, J. Theoretical Simulation and Modeling of Three-Dimensional Batteries. *Cell Reports Physical Science* **2020**, *1* (6), 100078. https://doi.org/10.1016/j.xcrp.2020.100078.

(20) Goldin, G. M.; Colclasure, A. M.; Wiedemann, A. H.; Kee, R. J. Three-Dimensional Particle-Resolved Models of Li-Ion Batteries to Assist the Evaluation of Empirical Parameters in One-Dimensional Models. *Electrochimica Acta* **2012**, *64*, 118–129. https://doi.org/10.1016/j.electacta.2011.12.119.

(21) Liu, Z.; Yuan, X.; Zhang, S.; Wang, J.; Huang, Q.; Yu, N.; Zhu, Y.; Fu, L.; Wang, F.; Chen, Y.; Wu, Y. Three-Dimensional Ordered Porous Electrode Materials for Electrochemical Energy Storage. *NPG Asia Mater* **2019**, *11* (1), 12. https://doi.org/10.1038/s41427-019-0112-3.

(22) Nakashima, Y.; Kamiya, S. Mathematica Programs for the Analysis of Three-Dimensional Pore Connectivity and Anisotropic Tortuosity of Porous Rocks Using X-Ray Computed Tomography Image Data. *Journal of Nuclear Science and Technology* **2007**, *44* (9), 1233–1247. https://doi.org/10.1080/18811248.2007.9711367.

(23) Pearse, A.; Schmitt, T.; Sahadeo, E.; Stewart, D. M.; Kozen, A.; Gerasopoulos, K.; Talin, A. A.; Lee, S. B.; Rubloff, G. W.; Gregorczyk, K. E. Three-Dimensional Solid-State Lithium-Ion

Batteries Fabricated by Conformal Vapor-Phase Chemistry. *ACS Nano* **2018**, *12* (5), 4286–4294. https://doi.org/10.1021/acsnano.7b08751.

(24) Ashby, D. S.; DeBlock, R. H.; Lai, C.-H.; Choi, C. S.; Dunn, B. S. Patternable, Solution-Processed Ionogels for Thin-Film Lithium-Ion Electrolytes. *Joule* **2017**, *1* (2), 344–358. https://doi.org/10.1016/j.joule.2017.08.012.

(25) Zheng, S.; Shi, X.; Das, P.; Wu, Z.; Bao, X. The Road Towards Planar Microbatteries and Micro-Supercapacitors: From 2D to 3D Device Geometries. *Adv. Mater.* **2019**, *31* (50), 1900583. https://doi.org/10.1002/adma.201900583.

(26) Zhao, J.; Lu, H.; Zhao, X.; Malyi, O. I.; Peng, J.; Lu, C.; Li, X.; Zhang, Y.; Zeng, Z.; Xing, G.; Tang, Y. Printable Ink Design towards Customizable Miniaturized Energy Storage Devices. *ACS Materials Lett.* **2020**, *2* (9), 1041–1056. https://doi.org/10.1021/acsmaterialslett.0c00176.

(27) Costa, C. M.; Gonçalves, R.; Lanceros-Méndez, S. Recent Advances and Future Challenges in Printed Batteries. *Energy Storage Materials* **2020**, *28*, 216–234. https://doi.org/10.1016/j.ensm.2020.03.012.

(28) Tagliaferri, S.; Panagiotopoulos, A.; Mattevi, C. Direct Ink Writing of Energy Materials. *Materials Advances* **2021**, No. 2, 540–563. https://doi.org/10.1039/d0ma00753f.

(29) Saha, B.; Goebel, K. Modeling Li-Ion Battery Capacity Depletion in a Particle Filtering Framework. **2009**.

(30) Browne, W. *Electrochemistry*; Oxford University Press: New York, New York, 2018.

(31) Fisher, A. C. *Electrode Dynamics*; Oxford University Press, 1996.

(32) Kim, J.; Park, S.; Hwang, S.; Yoon, W.-S. Principles and Applications of Galvanostatic Intermittent Titration Technique for Lithium-Ion Batteries. *J. Electrochem. Sci. Technol* **2022**, *13* (1), 19–31. https://doi.org/10.33961/jecst.2021.00836.

(33) Schied, T.; Nickol, A.; Heubner, C.; Schneider, M.; Michaelis, A.; Bobeth, M.; Cuniberti, G. Determining the Diffusion Coefficient of Lithium Insertion Cathodes from GITT Measurements: Theoretical Analysis for Low Temperatures**. *ChemPhysChem* **2021**, *22* (9), 885–893. https://doi.org/10.1002/cphc.202001025.

(34) Hsu, C. H.; Mansfeld, F. ***Technical Note:*** Concerning the Conversion of the Constant Phase Element Parameter Y_0 into a Capacitance. *CORROSION* **2001**, *57* (9), 747–748. https://doi.org/10.5006/1.3280607.

(35) Drummond, R.; Cheng, C.; Grant, P. S.; Duncan, S. R. Modelling the Impedance Response of Graded $LiFePO_4$ Cathodes for Li-Ion Batteries. *J. Electrochem. Soc.* **2022**, *169* (1), 010528. https://doi.org/10.1149/1945-7111/ac48c6.

(36) Lazanas, A. Ch.; Prodromidis, M. I. Electrochemical Impedance Spectroscopy─A Tutorial. *ACS Meas. Sci. Au* **2023**, *3* (3), 162–193. https://doi.org/10.1021/acsmeasuresciau.2c00070.

(37) Córdoba-Torres, P.; Mesquita, T. J.; Nogueira, R. P. Relationship between the Origin of Constant-Phase Element Behavior in Electrochemical Impedance Spectroscopy and Electrode Surface Structure. *J. Phys. Chem. C* **2015**, *119* (8), 4136–4147. https://doi.org/10.1021/jp512063f.

(38) Schalenbach, M.; Durmus, Y. E.; Tempel, H.; Kungl, H.; Eichel, R.-A. Double Layer Capacitances Analysed with Impedance Spectroscopy and Cyclic Voltammetry: Validity and

Limits of the Constant Phase Element Parameterization. *Phys. Chem. Chem. Phys.* **2021**, *23* (37), 21097–21105. https://doi.org/10.1039/D1CP03381F.

Chapter 5. Graded Electrodes in Sol-Gel Derived Catholytes

Solid state lithium ion batteries have been a continued area of interest especially in the electrification of vehicles. Solid state batteries provide a potential solution to safety issues from the traditional use of organic liquid electrolytes. However, in these devices, there is a sacrifice in performance due to high resistance at the electrode/electrolyte interface. This study expands upon the work introduced with ionogels, a pseudo-solid electrolyte, which has an ionically conducting medium infiltrated throughout an insulating porous silica gel network. In this chapter, the ionogel concept is applied to a cathode system, with a redox active transition metal oxide gel network infiltrated with an ionically conducting electrolyte medium. The transition metal oxide studied in this chapter is vanadium pentoxide, in part because of the tunability of the gel synthesis and because of the range of oxidation states of vanadium that can be accessed during charging/discharging. Optimal synthesis parameters for a vanadium catholyte were identified, and the electrochemical results shown present a direction for further work on the catholyte system.

Chapter 5.1. Introduction

Lithium ion batteries (LIBs) have emerged as the principal technology for a wide range of mobile energy storage applications, from portable electronics to electric vehicles. Current battery technology is based on using organic liquid electrolytes which lead to safety concerns of high flammability and internal shorting of the device. To overcome these safety issues, research in the LIB field has moved towards developing a fully solid-state battery design.[1] Solid-state batteries substitute a non-flammable solid electrolyte for the liquid electrolyte and can be operated at higher temperatures because of the solid material's thermal stability. Solid electrolytes also minimize the formation of the solid electrolyte interphase (SEI) at the electrode/electrolyte interface.[1–3] For these reasons there has been considerable interest in the design and development of materials for solid-state batteries. Solid electrolytes in particular have received considerable attention over the past few years and much research has focused on the issue of ion transport at the electrode/electrolyte interface. For current LIB technology, this interface and the role of ionic conductivity is fairly well understood. Liquid electrolyte can penetrate the pores of the cathode material and the mobile ions in the liquid electrolyte help to promote redox reactions within the electrode. A solid-state battery has no liquid electrolyte; in this case a solid/solid interface is produced between the solid electrolyte and the cathode material, leading to high interfacial resistance. Thus, a problem in shifting to solid-state battery designs is the increased battery resistance, leading to lower power devices with generally poorer battery performance than that of current LIB technology.[4–6]

One approach that has led to the successful development of solid-state electrolytes is based on ionogels.[5,7] Ionogels make use of ionic liquids which possess such desirable electrolyte properties as thermal and electrochemical stability, reasonable levels of ionic conductivity, low vapor pressure and nonflammability.[7] Ionogel synthesis is designed to incorporate ionic liquid electrolytes (ILE) into a solid matrix that can be made from polymers or inorganic solids such as silica. In the latter case, ionogels are synthesized using a sol-gel method. The ILE is combined with appropriate sol-gel precursors so that upon hydrolysis and condensation, a mesoporous network forms which confines the ILE by capillary forces within nanoscale pores. The resulting ionogel behaves as a solid macroscopically, however, at the nanoscale it behaves as a liquid. As a result, the ionic conductivities and electrochemical stability windows of ionogels are close to those of liquid electrolytes.[5,8] The two interpenetrating phases, the ILE and the silica network, are in intimate contact, with ion transport occurring solely within the ILE phase.[9]

The concept of the ionogel can be taken and applied to cathode design. That is, this ‘ionogel-cathode’ material can be designed to mimic the same principles explored with ionogel electrolytes, only now the inorganic network will be electrochemically active instead of being insulating. An inorganic porous network, similar to that of an aerogel, can be synthesized and infiltrated with an ionic liquid. The aerogel-like structure can be compared to that of an aperiodic sponge- a porous high surface area 3D electrode structure. In this way, the porous network interacts directly with the ionic liquid, allowing for high surface area interaction while keeping the resistance at interfaces low. A transition metal oxide, specifically vanadium oxide, is a good material to consider for this application because of its ability to be formed by sol-gel methods as well as the various valence states and structures in which it can exist.[10,11]

Vanadium pentoxide (V_2O_5) is a transition metal oxide that has been of interest to the battery field for a number of years as a cathode material. In part, it is because of the range of oxidation states of vanadium that can be accessed during charging/discharging leading to high theoretical specific capacities.[6] For many decades, vanadium pentoxide xerogels were the area of focus of this material. While the xerogel material works well as an electrode material, the current research will instead use vanadium pentoxide ambigels as the cathode material. In comparing a xerogel to an ambigel, or the more commonly referenced aerogels, the difference is in their morphology and microstructure achieved by drying the material from different solvents.[12,13] Xerogels are dried from the synthesis solvent. During drying they experience high capillary pressures as the solvents have high surface tensions and vapor pressures, which results in lower overall porosities.[12,13] Aerogels on the other hand, have extremely high porosities because they are supercritically dried. In this process the material is said to experience no capillary pressure, therefore, the pores do not collapse. The ambigels, which will be further developed in this project, have porosities higher than xerogels and lower than aerogels. This is because ambigels are dried ambiently from a nonpolar drying solvent, and although surface tensions are minimized, they are still present during the drying process.[12] The microstructures of the ambigels are desirable for lithium intercalation because of their optimal pore size distributions (mesoporous sized pores). Work reported in literature has proven that these materials are good for electrode applications.[14–17]

The dried vanadium pentoxide gels are nanocrystalline or amorphous in nature, meaning they generally lack long range order. However, local V_2O_5 structures have been studied and identified. The V_2O_5 xerogel is made up of two V_2O_5 single layers of repeating square pyramidal units of VO_5 that form bilayers. These bilayers form slabs or nanoribbons, both are common ways to describe the microstructure of V_2O_5. The space between the bilayers is where ions intercalate (Figure 1). The V_2O_5 expands and contracts as ions are inserted and removed.[18,19] This is different compared to crystalline V_2O_5 because in its crystalline form, the oxide is made up of connected single layers instead of the bilayer structure. Thus, the space between the layers is smaller. The other benefit of utilizing vanadium pentoxide derived from sol-gel is the ability to fine tune the synthesis process to be able to include additives such as carbon. In traditional electrode designs, carbon additives (i.e., carbon nanotubes, carbon black, carbon nanofibers, etc.) help to create 3D electrically conducting networks within the electrode.[20] A similar concept has shown to be true when integrating carbon nanotubes into a V_2O_5 gel because the material has low electronic conductivity.[17,20]

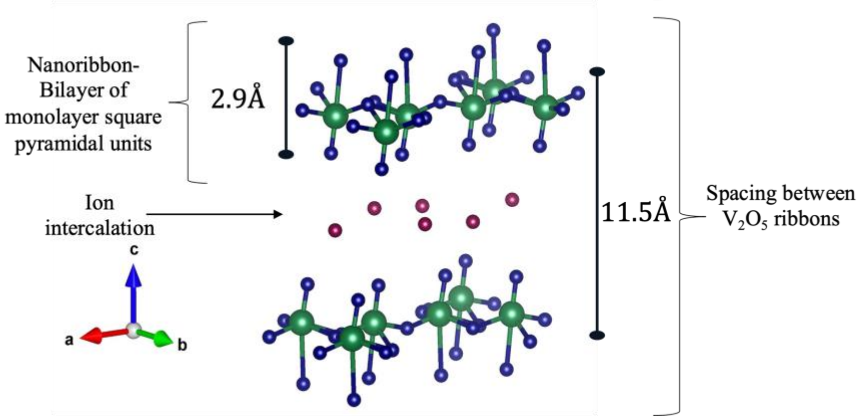

Figure 5.1. V_2O_5 xerogel structure comprised of nanoribbon-bilayers of square pyramidal units of V_2O_5, the nanoribbon double layer has interlayer spacing that allows for the intercalation of ions.[10,18]

The overarching research objective of this chapter is to adapt the previously studied V_2O_5 xerogels and develop processes so that synthesized gels can be used as free standing electrodes for lithium ion batteries. Due to the porous structure, V_2O_5 gels will be infiltrated with an ionically conducting medium, here ionic liquid electrolytes, to create a "catholyte" to be used as a cathode in a solid state battery. Infiltrating the 3D cathode with electrolyte should improve characteristics of the electrode such as rate capability and assuming that 100% of the cathode space in the cathode is infiltrated, this can also help make sure that the entire cathode is participating in the redox process.[21,22]

While cathodes with a 3D porous architecture have shown promise as cathodes in a solid state battery (SSB), SSBs face challenges when it comes to the internal and interfacial resistances, as well as the overall conductivity.[23–25] To address this issue, a graded battery system can be used where the porosity and pore size distributions of both the cathode and electrolyte are manipulated. In this case the system would be the optimized vanadium gel as the cathode and the solid electrolyte an ionogel, where there would be a continuous ionic liquid electrolyte phase throughout. Studies have been done on different levels of graded electrode systems with different numbers of layers of varying porosities. For the present case this will be a 2 layer graded system. One consideration here is that the varying layers should have a similar porosity to minimize mismatch between layers.[23,25,26] This should also minimize some of the interface effects commonly seen to help improve electrochemical properties.

Chapter 5.2. Experimental Methods

General Vanadium Aerogel Synthesis

Sol-Gel synthesis was used to create vanadium aerogels using previously reported compositions as a basis for the work.[16,27] Samples were made both with and without carbon additives. The carbon additives in this work were added by weight, 10% single walled carbon nanotubes (SWNTs) and 15% multi-walled carbon nanotubes (MWNTs) (both purchased from Sigma-Aldrich and used as received). Carbon was suspended in acetone by mixing via vortex mixer for 10 minutes. Water was then added to the acetone/carbon, or acetone solution and sonicated for 45 minutes. Once sonicated, the water/acetone mixture with and without carbon was then cooled in an ice bath for one hour to slow the rate of gelation. Vanadium (V) Triisopropoxide (purchased from Sigma-Aldrich) was mixed with the cooled solution and then the sol was cast prior to gelation. Depending on intended measurements, gels were cast to be free standing, or were cast onto a aluminum foil or stainless steel mesh substrate.

Determining effect of aging: The first set of samples considers the effect of aging time on the gel network. The synthesis followed the procedure outlined in the general vanadium aerogel synthesis, using a composition of 1:20:40 vanadium precursor to water to acetone. Once cast, the gels were sealed for 18, 24, 48 and 72 hours before undergoing solvent exchange and additional characterization.

Determining effect of synthesis: The second set of samples considers the effect of changing the synthesis conditions. The procedure outlined above was used. Four syntheses were identified based on previous work;[27] the resulting compositions being ratios of 1:20:40, 1:60:75, 1:20:75, and 1:60:100 for vanadium:water:acetone. Based on prior work, increasing water content should result in a stiffer gel and the increase in acetone, a higher surface area. Once cast, all gels were sealed for 72 hours before undergoing solvent exchange and additional characterization.

Determining effect of sol pH: The third set of samples considers the effect of changing the starting pH of the sol prior to gelation. This set included no carbon additives. Sodium bicarbonate and ammonium bicarbonate salt were added to water in order to increase the pH. The water was then added to acetone and the resulting residue was filtered out using filter paper and a Büchner funnel. After, the procedure outlined above was followed, the gels were cast and sealed for 72 hours before undergoing solvent exchange and additional characterization.

Solvent Exchange of Gels

Aged gels underwent a solvent exchange process starting in acetone, which acts as a pore fluid during the sol-gel process, to a solvent with lower surface tension, namely heptane. Samples were either dried from heptane or underwent an additional solvent exchange step of a heptane/ionic liquid mixture and then dried ambiently.

Microstructure Characterization of Vanadium Aerogels

Porosity Calculation: Total porosity of the samples was measured using Archimedes principle. Sample volumes were calculated by finding the average thickness and using ImageJ analysis for the area. The samples were then weighed after exposure in ambient air for 30 minutes and after being dried in an oven at 80°C. The porosity was then calculated using the equation:

$$\phi = 100 * \frac{\frac{\left(\frac{W_a}{W_d}\right)}{\rho}}{\left(\frac{W_a}{\rho}\right)} \qquad (Eqn.\ 5.1)$$

Where ϕ is porosity, W_a the sample weight in air, W_d the weight after drying, and ρ the density of the material (3.36 g/cm^3). The calculated porosity was then used to determine the total pore volume of the gel. This can be done by:

$$Total\ Pore\ Volume\ (V) = \frac{\phi}{\rho(1-\phi)} \qquad (Eqn.\ 5.2)$$

N_2 adsorption testing was performed using a Micromeretics ASAP 2020 instrument to characterize the micro- and mesoporous pore size distribution and surface area. Samples were heated at 110°C for two hours to remove any water before testing. BET surface areas were calculated, and BJH pore size distributions were determined from isotherm data. The volume of micropores was calculated from the adsorption-desorption isotherms using the relative pressures at p/p_o=0.2 and for the mesopores p/p_o=0.98, by converting moles of nitrogen absorbed at that pressure to the volume of nitrogen adsorbed. From here, the value of micropores and mesopores can be subtracted from the total pore volume to determine the volume of macropores.

Determining the pore size distribution: Dried gels without electrolyte, were cut into sections to determine the porosity and pore size distribution of the gel from the bottom to top. Scanning Electron Microscopy (SEM) was done using an FEI Nova 230 Nano to observe the surfaces for macropores (pores >100nm). These gel sections were then crushed and suspended in ethanol before being drop cast on a Transmission Electron Microscopy (TEM) grid. TEM was carried out using a Titan T12 instrument**.** TEM images were taken of the different gel sections to determine the distribution of pores throughout the sample.

Temperature Dependent Conductivity Testing

Conductivity of the various samples was taken with and without ionic liquid infiltration to obtain the mixed ionic-electronic and electronic conductivity, respectively. Samples were put in a polypropylene tube between two steel posts and connected to a VMP potentiostat/galvanostat (Bio-Logic) Electrochemical Impedance Spectroscopy (EIS) measurements were then taken at 10°C intervals from 20°C-80°C to determine the conductivity dependence on temperature. Impedance values were used to calculate the conductivity of the samples at each temperature using the equations below:

$$\sigma = \frac{1}{\rho} \qquad (\textit{Eqn. 5.3})$$

$$\text{where } \rho = \frac{RA}{L} \qquad (\textit{Eqn. 5.4})$$

Here, σ is conductivity (S/cm), ρ is resistivity (Ohm-cm), R resistance (Ohm), A interfacial area (cm^2), and L the length between contacts (cm). Comparison of the mixed ionic-electronic and electronic conductivity at each temperature step enables one to determine the ionic contribution to the conductivity. Additionally, the temperature dependent mixed ionic-electronic conductivity exhibits Arrhenius behavior. Because of this behavior, when inverse temperature (*1/T*) is graphed vs natural log conductivity ($ln\sigma$), the slope of the graph is the activation energy (E_a) divided by the ideal gas constant (R). This can be represented by the following relationship, and equation of a line:

$$ln\sigma \propto \frac{-E_a}{RT} \qquad (\textit{Eqn. 5.5})$$

$$ln\sigma = \left(-\frac{E_a}{R}\right)\left(\frac{1}{T}\right) + \ln A \qquad (Eqn.\ 5.6)$$

Using the information above, temperature dependent diffusion coefficients were also calculated using the equation:

$$D = A + e^{-\frac{E_a}{RT}} \qquad (Eqn.\ 5.7)$$

Electrochemical Testing

Electrochemical testing was done in a half cell arrangement with a lithium metal reference and counter electrode using coin cells, Swageloks, and flooded cells. Coin cell assembly, and all Swagelok and flooded cells were done in an argon-filled glove box. Cyclic voltammetry (CV) and galvanostatic charge-discharge (GV) measurements were made from 1.5-3.5V, using a VMP potentiostat/galvanostat (Bio-Logic) as were galvanostatic intermittent titration technique (GITT) measurements. For CV and GV, multiple scan rates and charge rates were tested to determine the reversibility and stability of the material. The GV and GITT tests are explained in more detail in chapter 2.

Chapter 5.3. Results and Discussion

While there are benefits to using the porous structure for battery electrodes because of the increase in surface area and AEF as discussed in chapter 3, there are also limiting factors when it comes to fine tuning the microstructure. Some of these limitations include the pore size distribution, the overall volume of pores, and the tortuosity of the gel. Many of these characteristics can be determined by Nitrogen Porosimetry. These influence the confinement of liquid within the pores and also contribute to higher measured resistances.[28–30] Many studies have shown that the less tortuous the porous medium is, the lower the measured resistances should be and the higher the measured conductivities.[31–35] This general concept is represented by the mathematical relationship:

$$D_{\mathrm{eff}} = \frac{D\epsilon}{\tau} \tag{\textit{Eqn. 5.8}}$$

Where D_{eff} and D are the effective and intrinsic diffusivities of the conductive phase, τ is the tortuosity of the porous network, and ϵ is the volume fraction of the conductive phase or porosity. The intrinsic diffusivity is characteristic to the material, and the effective diffusivity, determined experimentally, represents the ease with which the conductive liquid moves through the porous medium.

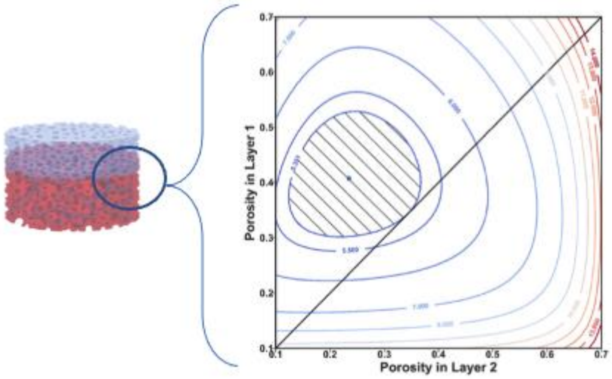

Figure 5.2. Resistance plot of a graded cathode in terms of the layer porosities [Modified from reference 26].

In order to optimize the microstructure, several variations in vanadium pentoxide gel synthesis were tested including aging time, synthesis composition, and pH of the sol. All of these parameters are used to manipulate material microstructure in the sol-gel process and have been reported on extensively.[12,13,36,37] The general gelation mechanism for vanadium triisopropoxide in the presence of water involves hydrolysis and condensation reactions which occur simultaneously, while acetone acts as the pore fluid. The reactions have been reported in literature as follows:[18,38,39]

$$(C_3H_7O)_2OV(C_3H_7) + H_2O \rightarrow (OC_3H_7)_2OV(OH) + C_3H_7OH \qquad (1)$$

$$(OC_3H_7)_2OV(OH) + (C_3H_7O)_2VO(OC_3H_7)_2 \rightarrow = (OV - O - VO) + C_3H_7OH \qquad (2)$$

The modification of the three parameters will influence the amount of cross linking, volume shrinkage, surface area, and rate of gelation.[40] All three factors were tested separately to create an optimized vanadium gel for electrode application.

The first parameter was aging time. Longer aging times have been shown to lead to higher degrees of crosslinking, resulting in a more mechanically stable dry gel. While some degree of cross linking is desirable, for handling and application, aging for too long can result in smaller surface areas. For consistency across the varying aging times, one gel composition of 1:20:40 vanadium triisoporopoxide:water:acetone was used. Samples were aged for either 18, 24, 48, or 72 hours denoted by a number 1-4 in the sample name. Aging was also done for samples both containing and not containing carbon and are denoted by A-C in the sample name- for no carbon, inclusion of SWNTs, or MWNTs respectively.

To characterize the microstructures of dried gels, porosities of each sample were calculated (Eqn. 5.1) and used to determine the total pore volume of the sample (Eqn. 5.2. Nitrogen porosimetry was measured and used to calculate the BET surface area and pore volume. Samples aged in this set for 72 hours (4A-4C), demonstrate that the surface area decreases even while the porosity remains within a similar range for these samples (high 70% to low 90%). Gels aged for 24 and 48 hours had the highest BET surface areas across all three samples, and this translated to higher ionic and electronic conductivities at room temperature, however, monoliths were not consistently obtained through the solvent exchange process. The samples aged for 72 hours on the other hand, consistently resulted in monoliths, therefore this aging time was used for all other studied compositions.

After aging, multiple compositions were identified from a previously reported study, involving high surface areas and capacity.[27] The four chosen compositions change the molar ratio of water or acetone used in the sol to the vanadium precursor. First the ratio of acetone to the other precursors was increased, changing the composition from 1:20:40 to 1:20:75. The increased acetone in the synthesis resulted in higher surface area gels after drying from heptane. One possible explanation is that less pore collapse occurred during the aging process by preventing the acetone from evaporating, minimizing capillary pressures. The process was repeated by increasing the molar ratio of water, and then both water and acetone for compositions of 1:60:75 and 1:60:100 respectively. While both resulted in dried gels with larger pores compared to the original synthesis parameters, the 1:60:100 synthesis had larger surface areas and better conductivities with and without the carbon additives compared to the 1:60:75 sample set. Based on these results, a higher molar ratio of acetone in the initial synthesis is needed for an ambiently dried high surface area gel. The smallest ratio of water to acetone (1:20:75) was determined to have the optimal microstructure for cathode application due to the high volume of mesopores, with a peak pore width of 60nm, in the pore size distribution (PSD) shown in Figure 5.3.

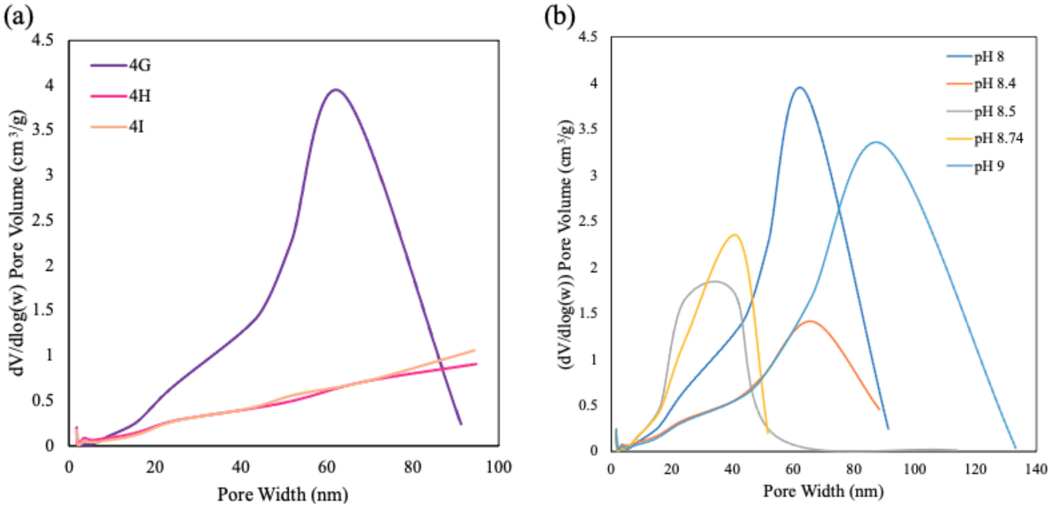

Figure 5.3. (a) Pore size distribution for samples 4G, 4H, and 4I (set 1:20:75). (b) Pore size distributions for samples with modified pH.

Finally, the rate of gelation can be controlled by changing the pH of the sol solution prior to gelling. Sol-gel processing involves competing hydrolysis and condensation reactions that are favored depending on the pH of the solution.[12,13] In order to further increase the rate of reaction and the condensation mechanism, the pH of water was increased. By increasing the rate of condensation, the resulting vanadium gel has a stiffer network that will minimize shrinkage during the aging process, helping to maintain higher surface areas and possibly improve lithium conduction. The pH was increased from 8 to a range from 8.4-9.01, using the same synthesis as that outlined for sample 4G. By increasing the pH from 8, the measured surface area was higher for all samples in this set. The vanadium gels with the highest surface areas were synthesized at a pH of 8.5 and 8.74 with surface areas above 130m^2/g. These two samples were also the only two with a peak pore size at 30nm, shifted from 60nm at a pH of 8. A peak pore size of 30nm has been reported as an optimal pore size for lithium conduction (Figure 5.3.).[1–3]

These two samples show some of the highest mixed ionic-electronic and electronic conductivities (Table 5.2.). However, for device integration, the stiffer gel matrix is too brittle for testing in a coin cell. Further optimization of synthesis pH is a promising avenue for developing V_2O_5 catholyte gels. A summary of the microstructure of all vanadium sample compositions can be found in Table 5.1. Additional characterization such as XRD and TEM was done to verify the aerogel structure. The XRD of samples 4A-4C show characteristic spectra for vanadium aerogels and the TEM displays the characteristic fiber-like microstructure of V_2O_5. The darker agglomerates are carbon nanotubes (CNTs).[10,41]

Table 5.1. Summary of Microstructure Characterization for all Dry Vanadium Gels.

Vanadium: Water: Acetone	**Aging (hr)**	**Carbon Additive**	**pH of Sol**	**Sample Name**	**Surface Area (m^2/g)**	**Total Pore Volume (Calculated)**	**BET Pore Volume (cm^3/g) <50nm pores**	**Volume of Macropores (cm^3/g) 50nm<**	**Volume of Mesopores (cm^3/g) 5nm<x<50nm**	**Volume of Micropores (cm^3/g) <5nm**	**Porosity**	**Electronic Conductivity (20°C) (S/cm)**
1:20:40	*18*	--	8	1A	79.63	1.41	0.62	0.79	0.61	0.045	0.82	2.22E-06
		SWNT	8	1B	107.44	1.79	0.88	0.91	0.88	0.047	0.86	2.95E-06
		MWNT	8	1C	37	0.95	0.28	0.66	0.28	0.015	0.76	4.70E-06
	24	--	8	2A	97.405	2.08	0.85	1.22	0.85	0.043	0.87	9.18E-06
		SWNT	8	2B	87.14	3.13	0.57	2.55	0.57	0.038	0.91	1.07E-05
		MWNT	8	2C	74.27	1.43	0.6	0.83	0.60	0.032	0.82	5.93E-06
	48	--	8	3A	79.99	2.09	0.51	1.58	0.50	0.035	0.87	3.80E-06
		SWNT	8	3B	71.25	1.44	0.49	0.95	0.49	0.032	0.83	6.75E-06
		MWNT	8	3C	78.76	1.33	0.49	0.84	0.48	0.035	0.81	6.42E-06
	72	--	8	4A	43.92	1.50	0.80	0.69	0.76	0.026	0.83	2.51E-06
		SWNT	8	4B	48.26	1.73	0.60	1.13	0.58	0.028	0.85	9.80E-06
		MWNT	8	4C	84.10	1.67	0.71	0.96	0.70	0.038	0.85	1.18E-05
1:60:75	*72*	--	8	4D	71.978	1.49	0.51	0.98	0.50	0.031	0.83	2.24E-06
		SWNT	8	4E	75.10	1.31	0.50	0.80	0.49	0.033	0.81	2.48E-05
		MWNT	8	4F	87.08	1.91	0.45	1.46	0.42	0.037	0.86	1.62E-05
01:20:75	*72*	--	8	4G	118.29	2.02	1.25	0.77	1.22	0.050	0.87	3.49E-06
		SWNT	8	4H	91.39	1.45	0.64	0.82	0.62	0.038	0.83	1.30E-05
		MWNT	8	4I	77.45	1.18	0.62	0.56	0.60	0.033	0.80	1.36E-04
01:60:100	*72*	--	8	4J	92.64	1.58	0.71	0.88	0.69	0.039	0.84	1.52E-05
		SWNT	8	4K	94.89	2.31	0.64	1.67	0.62	0.040	0.88	5.06E-05
		MWNT	8	4L	90.09	2.22	0.60	1.62	0.58	0.038	0.88	3.37E-05
1:20:75	*72*	--	8.4	--	109.89	2.24	0.90	1.33	0.878	0.047	0.88	3.29E-06
		--	8.5	--	138.78	1.27	0.79	0.48	0.755	0.059	0.81	2.91E-06
		--	8.74	--	131.93	1.34	0.80	0.54	0.773	0.056	0.82	1.04E-05
		--	9.01	--	107.07	2.00	1.09	0.91	1.064	0.046	0.87	2.40E-06

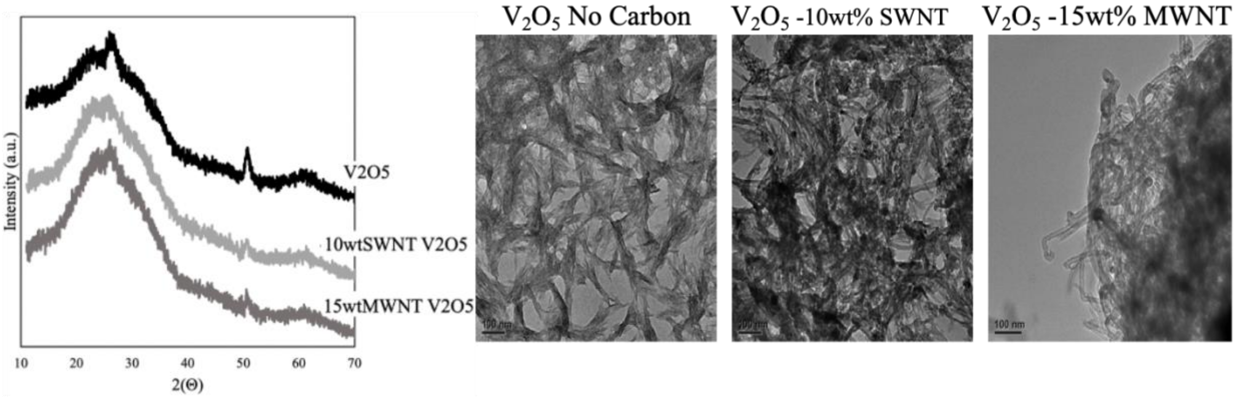

Figure 5.4. XRD and TEM of V2O5 Dry Gels with no carbon, SWNTs, and MWNTs (samples 4A-4C). The scale bar on the TEM images is 100nm.

To further characterize the gel microstructure, TEM was taken on sections of dried V_2O_5 (Figure 5.5). From the BET data, it was determined that the majority of the pores present in each sample are in the mesoporous regime, and the TEM was used to resolve them. In addition to understanding the pore regimes present, their distribution is important to achieving the gradient electrode/electrolyte interface.[42–44] Having a continuous pore structure throughout the entire gel volume would be advantageous to increasing volumetric energy and power density and ensuring that the conductive ionic liquid phase is infiltrated throughout. Because the vanadium gel will be integrated with a silica ionogel, a high volume of pores should exist closer to the surface of the vanadium gel. This will help to create the graded structure between the electrode and the electrolyte. The graded design should have an increasing volume of pores towards the surface of the electrode (vanadium gel) that will share an interface with the electrolyte (silica ionogel).[4–6] Having higher porosities in the electrode and electrolyte is ideal because it minimizes the chance of porosity mismatch between the layers and minimizes interfacial resistance.[5]

Vanadium ambigel samples were prepared as normal, then cut into thirds using a sharp blade and prepared for TEM. The three sections are denoted as top, middle and bottom. Based on the TEM images, it can be determined that the majority of the porosity exists at the top of the sample, which is consistent with the theory of drying developed by Scherer. When solvent is evaporated from a porous medium, the drying process is divided into three stages.[40,45] The initial conditions before evaporation begins is the first stage of drying followed by a constant rate period of steady state evaporation. Here, evaporation from the surface occurs and the gel shrinks uniformly until it reaches a critical point where the pores themselves can begin to empty, with solvent diffusing to the surface to dry. From there, the gel enters the falling rate period where pores empty and solvent is evaporated.[45] When pores begin to empty and shrink, capillary pressure increases which can lead to pore collapse. Some of the capillary pressure is mitigated through decreasing the Good-Girifalco interaction parameter by using a low surface tension non-polar drying solvent similar to heptane.[46]

The samples are dried in containers where only the top of the vanadium gel is exposed. Thus, the rate of evaporation is uneven from the top and the bottom. Due to the uneven drying, the majority of solvent evaporation is going to happen from the top of the gel while the middle and bottom of the gel will be denser than the top because of their higher capillary pressures. This is qualitatively supported in the TEM images where there is a high volume of pores shown in the top portion of the vanadium gel, but in the middle and bottom portion the presence of pores is limited or not evident. For this application, the top portion of the vanadium gel is still the most crucial to having a high volume of pores, however, the lack of pores in the middle region of the gel means that the ionic liquid will not be able to penetrate the whole volume of the V_2O_5. When a solid electrolyte interphase (SEI) layer begins to form, the volume accessed will be even more limited leading to capacity fade. To mitigate this dense middle layer, thinner V_2O_5 gels were made by drop casting the sol onto a stainless steel mesh or aluminum foil current collector. By minimizing gel thickness and increasing the cast area, the gel will shrink less during the first stages of drying because the starting volume is smaller. When drying enters the falling rate period and the pores begin to empty, the pressure is minimized because the distance to diffuse to the surface is shorter and solvent is more readily evaporated. Making thinner samples should help the resulting dry gels be less dense in the middle.

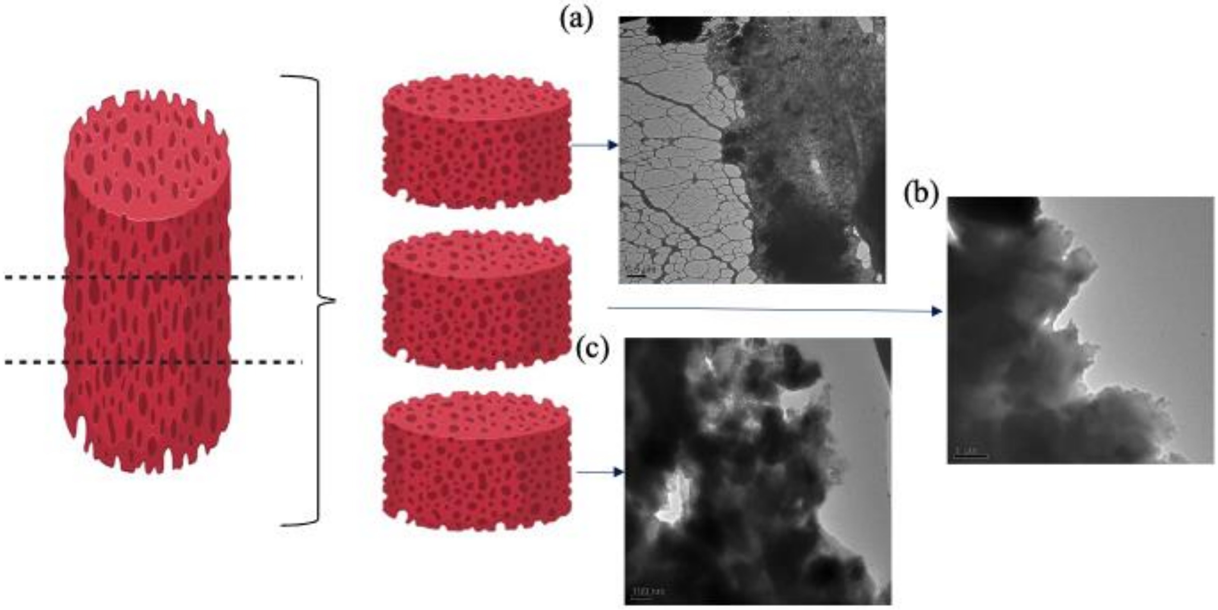

Figure 5.5. V2O5 gel was prepared using the 1:20:75 synthesis (sample 4G), and dried from heptane. The dried gel was cut into 3 sections and TEM images were taken of the (a)top, (b)middle, and (c)bottom section of the gel.

Once it was evident that pores were not continuous throughout the entire volume, additional characterization was done to determine the complexity of the pore structure via calculation of the mass fractal dimension from the BET isotherm.[47,48] Fractal dimension discusses the complexity of volume on a scale from 1-3, where 1 represents a less complex system where volume is distributed in one dimension, and then values of 2 and 3 represent more complex systems where mass is distributed in two and three dimensions. This value can be calculated by the nitrogen adsorption isotherm, where the slope of the linear regime from the plot of natural log of the nitrogen gas adsorbed versus natural log of pressure represents 3 minus the surface fractal dimension which is directly related to the mass fractal dimension.[47,48] This calculation was done for all samples, and the values ranged between 2.4-2.6, where there was no real variation between conductivities (Figure 5.9.). As such, all samples were deemed to have similar complexity. This was further confirmed by the calculated diffusion coefficient for the ionic liquid electrolyte in the confined vanadium gel matrix being similar values, on the same order of magnitude with one another (Table 5.2). If the tortuosities of the samples were drastically different, the extrinsic diffusion values calculated for the ionic liquid ([EMIM][TFSI]), would have also had to be different because the intrinsic diffusion coefficient of the [EMIM][TFSI] should not change regardless of microstructure (eqn. 5.8.).[31–35]

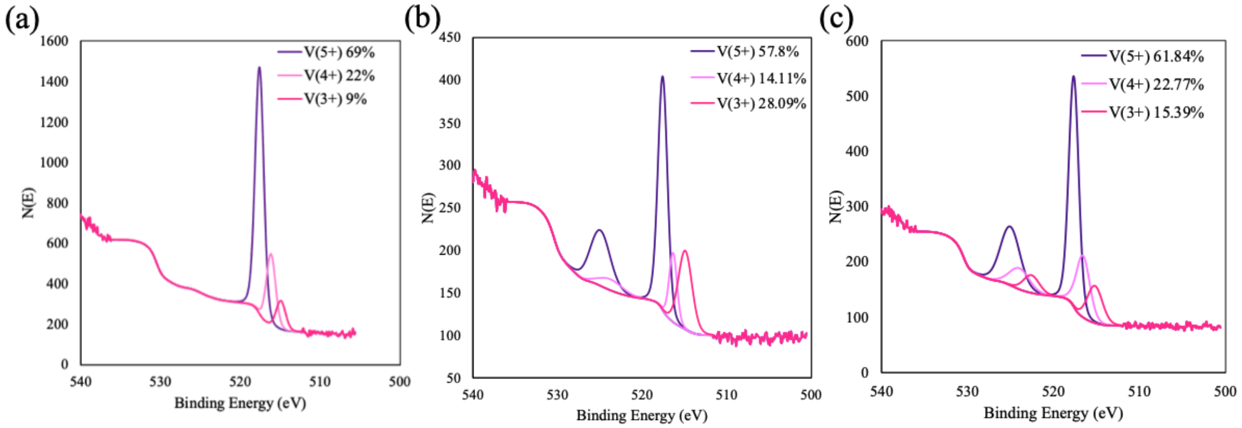

Figure 5.6. XPS of sample set 1:20:75 sample set, (a) sample 4G, (b) sample 4H, and (c) sample 4I. Similar ratios of V^{5+}, V^{4+}, and V^{3+} were obtained for all samples.

X-ray photoelectron spectroscopy (XPS) was used to detect the presence of V^{5+}, V^{4+}, and V^{3+}. Their respective contents are listed in Figure 5.6. The average oxidation state for the three samples are similar with G, H and I being $V^{4.6+}$, $V^{4.3+}$, and $V^{4.46+}$ respectively. All samples have similar average oxidation states with V^{5+} being the most abundant.

The electrochemical properties of the as-synthesized gels were measured on vanadium dry gels and vanadium ionogels in order to determine the effect of ionic liquid infiltration. The first step was to determine what percent of the infiltrated gels was filled with ionic liquid (Figure 5.7.). To do this, neat ionic liquid electrolyte ([EMI][TFSI]) was dripped onto the samples in increments of $5\mu L$. Vacuum was pulled on these samples for 10 minutes, the excess electrolyte was removed, and the samples were then weighed. Comparing samples G and H, (Figure 5.7. (b)), the electrolyte intake was around 22% and 30% which equates to about 15 μL and 16 μL of electrolyte respectively. This correlates to their similar measured conductivities as reported in Figure 5.9. For the vanadium gels without carbon (4A, D, G, and J) shown in Figure 5.7., the higher uptake of electrolyte seen for 4D and 4J is most likely due to their higher volume of macropores compared to 4A and 4G.

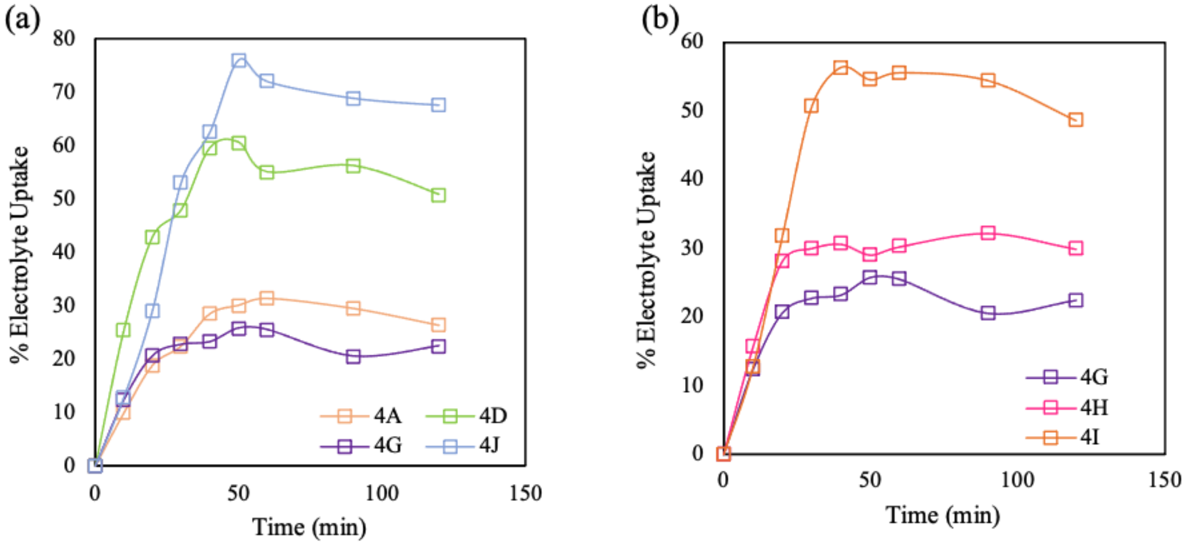

Figure 5.7. Weight percent uptake of electrolyte in samples aged for 72 hours for (a) all syntheses without carbon and (b) 1:20:75 sample set.

Impedance was measured for all samples from 20ºC to 80ºC both with ILE infiltration (neat [EMIM][TFSI]) and without infiltration. All of the impedance data was fitted to determine a representative circuit and calculate the conductivity. An example of this fit of the impedance data for both with and without ILE is shown in Figure 5.8. Both the electronic and mixed ionic-electronic Nyquist plots were fit with the same equivalent circuit using two time constants- a resistor in series with a resistor and constant phase element in parallel.[24] The constant phase element is representative of capacitor-like behavior without being an ideal capacitor—giving the impedance spectra the imperfect semicircle shape.

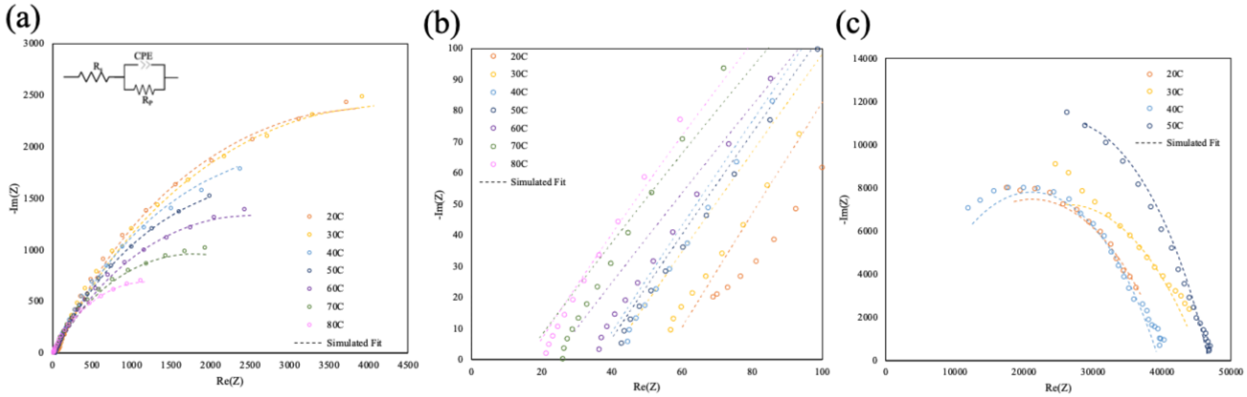

Figure 5.8. Impedance data for sample 4H, (a)ionogel (mixed conductivity), (b) the origin of the Nyquist plot, (c) dry gel (electronic conductivity) from 20ºC to 80ºC. Nyquist spectra are shown with a simulated equivalent circuit.

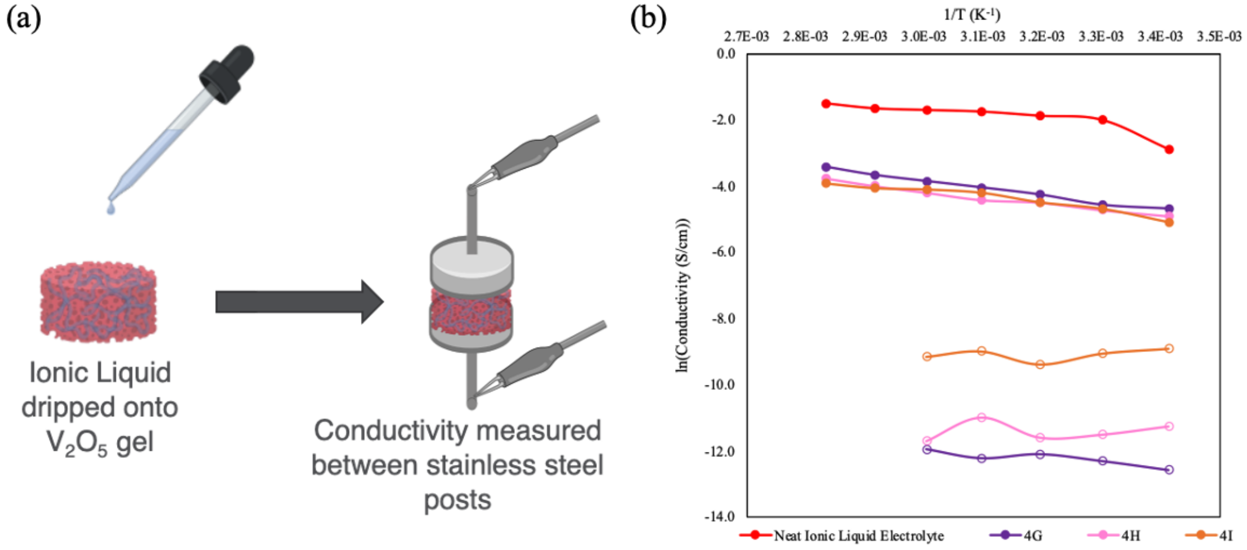

Figure 5.9. (a) Schematic of conductivity measurement procedure. (b) Plot of the conductivity versus inverse temperature for set 1:20:75. Mixed conductivity (vanadium ionogels) is shown with closed circles, the electronic conductivity (dry gels) with open circles.

The calculated conductivity values for the samples G-I were plotted as a function of inverse temperature to determine the temperature dependence of the sample conductivity. The conductivity (Figure 5.9) shows an Arrhenius relationship, and the data was used to calculate values such as the activation energy (in eV) and the diffusion coefficient for each sample. The mixed ionic-electronic and electronic conductivities are shown alongside the conductivity of the neat ILE ([EMI][TFSI]). Being that the unconfined neat ILE and neat ILE confined in the vanadium matrix are only two orders of magnitude different, this suggests that there is good infiltration of the neat ILE throughout a majority of the vanadium matrix and that these samples are suitable for cathode application. The differences in the electronic conductivity come from absence (sample G) or addition of CNTs (samples H and I). The SWNTs were used in a smaller weight percent than the MWNTs and this is seen in the increased conductivity of sample I over sample H.

As mentioned previously, the mixed ionic-electronic and electronic conductivities were measured by EIS over a range of temperatures (20ºC to 80ºC) on a vanadium ionogel and a dry vanadium gel, respectively. The vanadium gels are known to have low electronic conductivities, which is why carbon additives are being used to help improve this metric. This is shown in Figure 5.9, where the dry gels are shown to be resistive with low conductivities on the order of 10^{-5}-10^{-6} S/cm. Sample 4G (no carbon additives) had an electronic conductivity of 3.49×10^{-6} S/cm and sample 4H (SWNTs) had an electronic conductivity of 1.30×10^{-5} S/cm. The vanadium ionogels, on the other hand, are expected to and did have a more conductive mixed ionic-electronic conductivities due to infiltration of the ILE. Sample 4G and 4H had mixed conductivities of 9.26×10^{-3} S/cm and 7.43×10^{-3} S/cm respectively. The ionic contribution for all samples was determined by subtracting the electronic conductivity from the mixed ionic-electronic conductivity. The ionic conductivity contribution was used to calculate the diffusion coefficient at room temperature. This diffusion coefficient is representative of the diffusion of the electrolyte [EMIM][TFSI] in the confined vanadium gel matrix. Vanadium gels with the highest reported ionic contribution had higher diffusion values. All values calculated from the temperature dependent impedance testing are shown in Table 5.2.

Table 5.2. Conductivity, and Ionic Contribution of V2O5, Activation Energy, and Diffusion Coefficient of tested V2O5 ionogels.

Vanadium: Water: Acetone	Sample Name	pH	Mixed Ionic-Electronic Conductivity (20°C) (S/cm)	Ionic Contribution (20°C) (S/cm)	Activation Energy (eV)	Diffusion Coefficient (20°C) ($cm^2 s^{-1}$)
1:20:40	1A	8	6.55E-03	6.55E-03	2.46E-03	1.20E-04
	1B	8	4.39E-03	4.38E-03	3.97E-03	8.02E-05
	1C	8	5.16E-03	5.14E-03	5.91E-03	9.40E-05
	2A	8	1.20E-02	1.20E-02	4.37E-03	2.20E-04
	2B	8	1.27E-02	1.27E-02	4.52E-03	2.33E-04
	2C	8	1.50E-03	1.49E-03	6.07E-03	2.72E-05
	3A	8	1.05E-02	1.05E-02	4.05E-03	2.51E-04
	3B	8	4.55E-03	4.54E-03	4.00E-03	8.31E-05
	3C	8	1.38E-02	1.37E-02	4.04E-03	1.92E-04
	4A	8	4.61E-03	4.15E-03	2.80E-03	8.43E-05
	4B	8	9.61E-03	8.40E-03	4.09E-03	1.76E-04
	4C	8	4.30E-03	6.14E-03	2.50E-03	7.85E-05
1:60:75	4D	8	4.43E-03	6.33E-03	2.30E-03	1.16E-04
	4E	8	7.38E-03	7.36E-03	2.53E-03	1.35E-04
	4F	8	6.23E-03	4.83E-03	2.83E-03	8.83E-05
01:20:75	4G	8	9.26E-03	9.26E-03	2.76E-03	1.69E-04
	4H	8	7.43E-03	7.41E-03	2.38E-03	1.36E-04
	4I	8	6.19E-03	6.05E-03	2.42E-03	1.11E-04
01:60:100	4J	8	4.86E-03	4.84E-03	3.25E-03	8.85E-05
	4K	8	6.75E-03	6.70E-03	2.83E-03	1.23E-04
	4L	8	4.11E-03	4.07E-03	3.12E-03	7.45E-05
1:20:75	--	8.4	5.08E-03	5.93E-03	3.26E-03	9.26E-05
	--	8.5	6.78E-03	6.77E-03	3.72E-03	1.71E-04
	--	8.74	1.35E-02	1.35E-02	3.67E-03	2.46E-04
	--	9.01	5.94E-03	5.06E-03	3.42E-03	1.08E-04

Based on the conductivity results, initial cyclic voltammetry data, and ease of gel processing, sample H was determined to have the most desirable characteristics from the previously identified sample set using the 1:20:75 synthesis. Both the SWNTs and MWNTs were determined to improve the performance of the V_2O_5 gel in terms of their conductivity, however, the addition of SWNTs was favored over MWNTs because the SWNTs were easier to disperse throughout the gel during the synthesis (Figure 5.4.) and monoliths were more successfully obtained. Additionally, SWNTs have been previously shown to help keep the structural integrity of V_2O_5 xerogels and prevent capacity fade.[10,15]

Sample H was deposited in a thin layer onto an aluminum foil substrate, infiltrated with ILE during the solvent exchange process and then dried. The "dried" infiltrated gel was then assembled into a coin cell versus lithium. The material was then cycled at various charging rates from C/20 to C/5 (Figure 5.10.). The discharge curves have the representative shape of a vanadium pentoxide xerogel as previously reported by Livage with a gradual slope and slight knee at faster rates.[38] At a rate of C/20, the specific capacity of the gel was 100 mAh/g, 70% of the theoretical capacity of V_2O_5 with one electron redox. Previous work using V_2O_5 aerogels have shown higher than one electron redox with higher specific capacities, which is attributed to capacitive contributions due to the aerogel materials having higher surface areas on the order of 200-400 m^2/g instead of about $90m^2/g$ of sample H.[14–17]

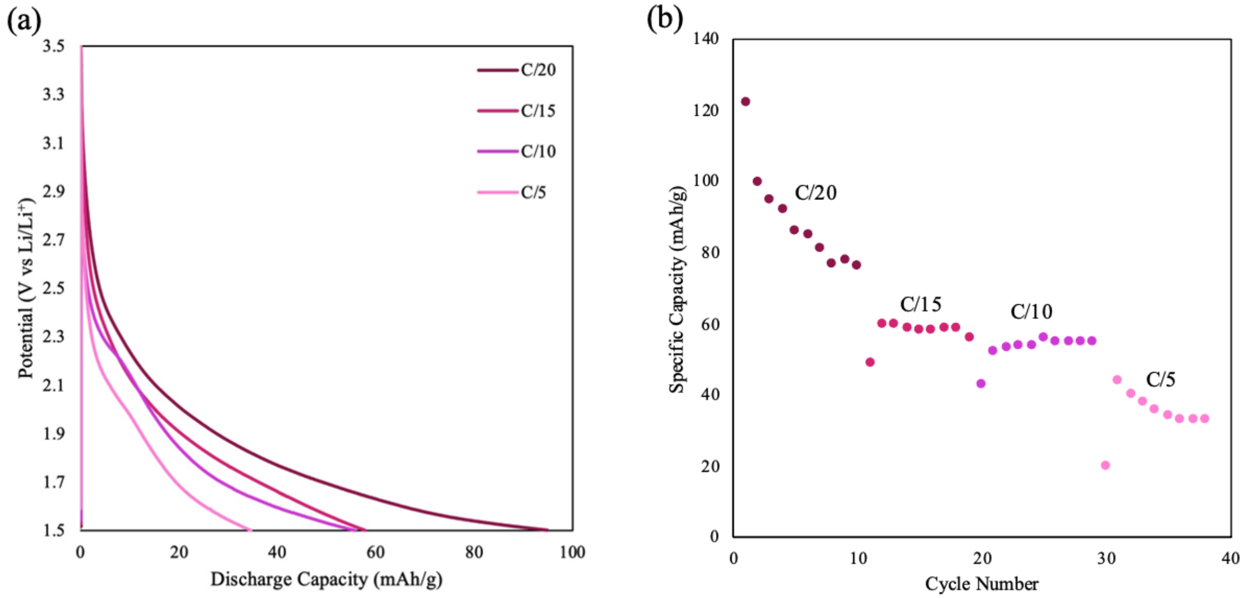

Figure 5.10. (a) Fifth cycle discharge capacity and (b) specific capacity by cycle at rates of C/20, C/15, C/10, and C/5. All data shown is in a coin-cell with sample H in a half-cell arrangement; the electrolyte used was 1M $LiClO_4$ in [EMI][TFSI].

The capacities at higher scan rates of C/15 and C/10 do show a leveling off of the capacity per cycle and an overall improved coulombic efficiency. The decrease observed at C/5 can most likely be attributed to the discontinuous pore structure of the vanadium gels leading to localized current hotspots, commonly reported in 3D architectures, leading to inconsistent charging and discharging. Because of the complexity of the pore structure, with fractal dimensions between 2.4-2.6 and their discontinuity, some of the open V_2O_5 volume is inaccessible at faster charging rates.[7,8] The capacity levels off at C/15 and C/10 because of the finite volume of the V_2O_5 gel being utilized. The voltage window was also shortened from 1.5-4V to 1.5-3.5V (versus Li/Li^+) because there was an irreversible reaction happening between 3.5-4V. While some of the capacity is lost by shortening the voltage window, the capacity was decreasing more than 50% during cycling at the slowest charging rate with the expanded voltage window.

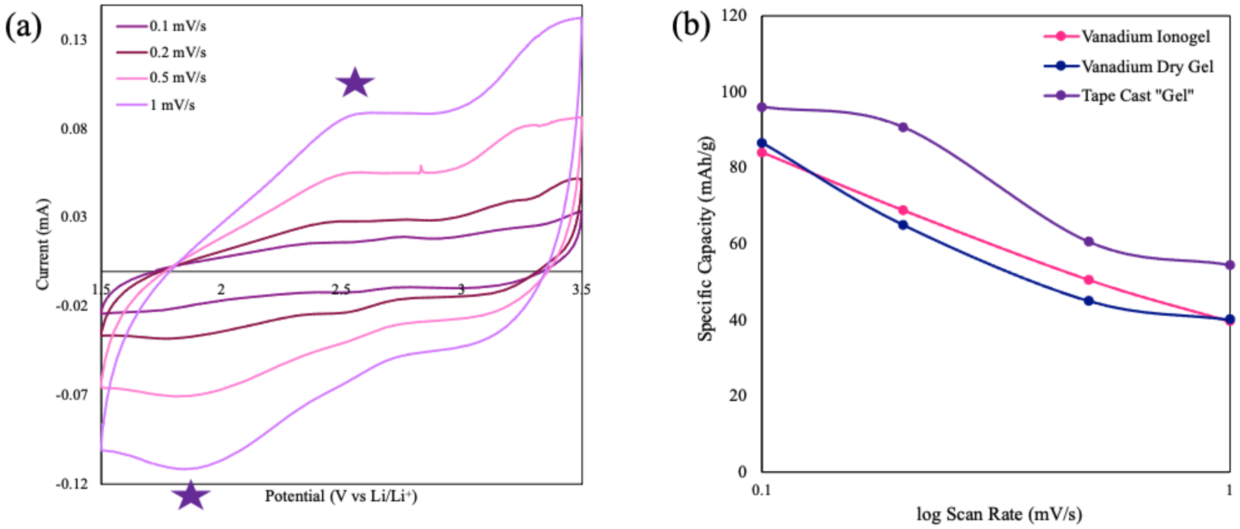

Figure 5.11. (a) Cyclic Voltammogram of a vanadium ionogel (sample 4H); and (b) calculated capacity for a vanadium ionogel, a vanadium dry gel, and a tape cast gel in a flooded three neck using 1M LiClO4 in PC at scan rates of 0.1mV/s, 0.2mV/s, 0.5mV/s, and 1mV/s. The two peaks marked on the cyclic voltammogram were analyzed with b-value analysis for values of 0.74 and 0.73 on the oxidation and reduction scans respectively.

Cyclic voltammetry (CV) was done on the vanadium ionogel, vanadium dry gel and a tape cast vanadium gel. The tape cast gel was made by creating a suspension of crushed dry vanadium gel and recasting it using the traditional tape cast method on an aluminum foil current collector. In the CV experiment, the relationship of current response to sweep rate can be used to determine the dominating charge storage mechanism by a power-law relationship:

$$i(v) = av^b \qquad (Eqn.\ 5.9)$$

here, *a* is a constant, *v* the scan rate, and *b* the power-law exponent. The *b*-value can be determined by graphing the log of the peak current versus the log of the scan rate for both reduction and oxidation scans.[49] The *b*=0.5 value is indicative of a diffusion controlled process and is representative of the charge storage mechanism in battery-like materials. For a b-value of *b*=1, this is representative of capacitive storage or surface-controlled mechanism as seen in pseudocapacitive materials.[49] For the anodic and cathodic sweeps of the vanadium ionogel 4H, the b-value was 0.74 and 0.73 respectively suggesting a mixed storage mechanism of diffusion and surface controlled. The specific capacity as a function of scan rate is comparable for all three vanadium gels- the ionogel, dry gel, and tape cast gel. Thus, the capacity is not largely affected by the infiltration of the ILE. This suggests that there is no negative impact on the electrochemical properties of the vanadium gel regardless of whether it is infiltrated with electrolyte or not, which is important for device development.

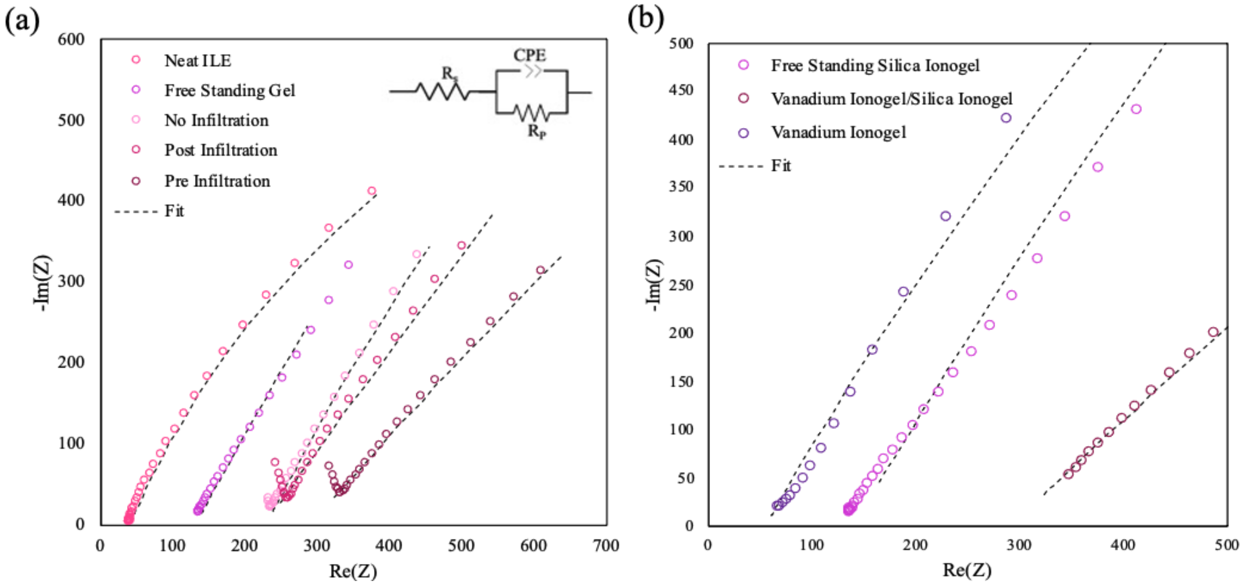

Figure 5.12. (a)Comparison of Nyquist Impedance for neat ILE, free standing ionogel and an ionogel drop cast on sample H that was not infiltrated with ILE during solvent exchange (No

Infiltration), was infiltrated with ILE after drying from heptane (Post Infiltration), and was infiltrated with ILE during solvent exchange (Pre Infiltration). (b) Nyquist impedance for a free standing ionogel, vanadium ionogel/silica ionogel (Pre Infiltration in (a)), and vanadium ionogel (sample 4H). The ILE used for all samples is [EMI][TFSI]. A simulated fit for the best representative circuit is shown for all samples.

To create the graded vanadium interface, the vanadium gels (both ionogel and dry gels) had an ionogel deposited on the porous cathode surface via drop-casting. The gels were aged, and then electrochemical impedance spectroscopy measurements were done on a freestanding ionogel, the graded dry gel/ionogel (no infiltration), a infiltrated dry gel/ionogel (post infiltration), and a vanadium ionogel/ionogel system. The EIS measurements were done at room temperature and the Nyquist impedance with its simulated circuit is shown in Figure 5.12. The highest calculated conductivities were for the neat ILE and free standing gel. The free standing silica ionogel has a measured ionic conductivity of $5.24\text{x}10^{-3}$ S/cm, one order of magnitude less than the reported ionic conductivity of unconfined [EMIM][TFSI] ($5.60\text{x}10^{-2}$ S/cm).[9]

Table 5.3. Resistance and conductivity of vanadium/silica ionogel samples.

Sample	Resistance (Ω)	Conductivity (S cm^{-1})
Neat ILE	38.6	5.60E-02
Free Standing Gel	121.6	5.24E-03
No Infiltration	228.8	2.23E-03
Post- Drying Infiltration	227.3	2.26E-03
Pre-Infiltration	286.3	3.11E-03

The addition of the silica ionogel did improve the conductivity of the dry gel with and without infiltration. The vanadium that was infiltrated with electrolyte post drying has almost the same conductivity as the vanadium that was not infiltrated with the electrolyte at all when tested with the silica ionogel. Because these vanadium dry gel layers can be made thinner, they are more brittle, and the dominating part of the conductivity here can be attributed to the ionogel. On the other hand, the pre-infiltrated gel had the highest conductivity in the graded vanadium ionogel/silica ionogel system at 3.11×10^{-3}S/cm. The pre-infiltrated system did have a small increase in the measured resistance after the addition of the ionogel of about 200Ω. The initial measured resistances of the vanadium ionogel and the silica ionogel on their own were 65Ω and 110Ω, respectively. All measured resistances and conductivities are reported in Table 5.3. Full cells were assembled with and without the use of the silica ionogel as the pseudo-solid electrolyte and separator. Charging and discharging experiments were done on these two full devices at a variety of different current densities ranging from $0.1 mA/cm^2$ to $1.0 mA/cm^2$, and within the voltage range of 1.5V to 3.5V. The exchange current was calculated by using the Butler-Volmer relationship between overpotential and current.[50–52] Similar exchange currents of

$58.1 \pm 3.1\ \mu$A and $55.3 \pm 3.9\ \mu$A were observed for both the vanadium ionogel were observed for both the vanadium ionogel with or without the silica ionogel protection layer, suggesting the electrode/electrolyte interface isn't affected changed with the addition of the ionogel.

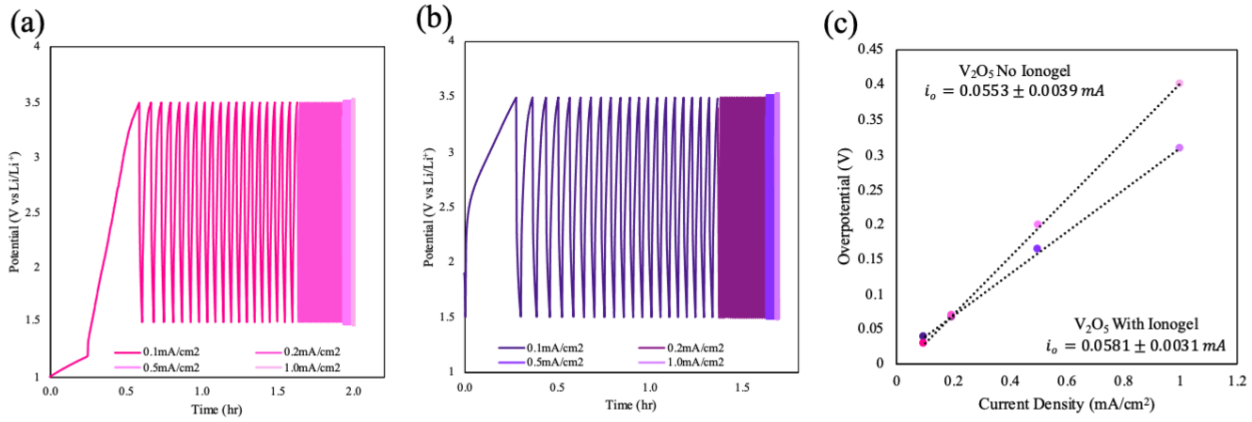

Figure 5.13. The charge/discharge experiments of V2O¬5 half-cell (a) without and (b) with ionogel, and the (c) calculated exchange current density.

Chapter 5.4. Conclusion

In this chapter, sol-gel processing was successfully used to demonstrate a vanadium pentoxide gel as an infiltrated cathode or catholyte. Modifying the parameters used in the sol-gel process – aging, composition, and pH, changed the resulting microstructure of the gels. For gels where aging time was increased, the available surface area measured by nitrogen porosimetry decreased. Increasing pH, improved condensation of the gel network, resulting in stiffer gels with higher measured surface areas. Lastly, when modifying composition, increasing the molar ratio of acetone increases the total available surface area leading to improvements in measured conductivity for both dry vanadium gels and vanadium ionogels. Key results are reported in Tables 5.1 and 5.2. Vanadium gels were then successfully infiltrated with ionic liquid electrolyte, and it was determined based on the cyclic voltammetry data that the infiltrated electrolyte does not affect the chemical properties of the gel. Lastly a silica ionogel, pseudo-solid electrolyte was used to coat the vanadium ionogel and create a graded electrode/electrolyte interface. EIS measurements show minimal increase in resistance across the electrode/electrolyte interface and full device integration shows successful charging and discharging with the porous electrode/electrolyte system. This work shows a promising development of using an ionically conductive porous network as an infiltrated cathode in a pseudo-solid state battery system.

Chapter 5.5. References

(1) Manthiram, A.; Yu, X.; Wang, S. Lithium Battery Chemistries Enabled by Solid-State Electrolytes. *Nat Rev Mater* **2017**, *2* (4), 16103. https://doi.org/10.1038/natrevmats.2016.103.

(2) Tatsumisago, M.; Nagao, M.; Hayashi, A. Recent Development of Sulfide Solid Electrolytes and Interfacial Modification for All-Solid-State Rechargeable Lithium Batteries. *Journal of Asian Ceramic Societies* **2013**, *1* (1), 17–25. https://doi.org/10.1016/j.jascer.2013.03.005.

(3) Richards, W. D.; Miara, L. J.; Wang, Y.; Kim, J. C.; Ceder, G. Interface Stability in Solid-State Batteries. *Chem. Mater.* **2016**, *28* (1), 266–273. https://doi.org/10.1021/acs.chemmater.5b04082.

(4) Chen, R.; Li, Q.; Yu, X.; Chen, L.; Li, H. Approaching Practically Accessible Solid-State Batteries: Stability Issues Related to Solid Electrolytes and Interfaces. *Chem. Rev.* **2020**, *120* (14), 6820–6877. https://doi.org/10.1021/acs.chemrev.9b00268.

(5) Zhao, X.; Wang, C.; Liu, H.; Liang, Y.; Fan, L. A Review of Polymer-based Solid-State Electrolytes for Lithium-Metal Batteries: Structure, Kinetic, Interface Stability, and Application. *Batteries & Supercaps* **2023**, *6* (4), e202200502. https://doi.org/10.1002/batt.202200502.

(6) Zheng, F.; Kotobuki, M.; Song, S.; Lai, M. O.; Lu, L. Review on Solid Electrolytes for All-Solid-State Lithium-Ion Batteries. *Journal of Power Sources* **2018**, *389*, 198–213. https://doi.org/10.1016/j.jpowsour.2018.04.022.

(7) Chen, N.; Zhang, H.; Li, L.; Chen, R.; Guo, S. Ionogel Electrolytes for High-Performance Lithium Batteries: A Review. *Adv. Energy Mater.* **2018**, *8* (12), 1702675. https://doi.org/10.1002/aenm.201702675.

(8) Ashby, D. S.; DeBlock, R. H.; Lai, C.-H.; Choi, C. S.; Dunn, B. S. Patternable, Solution-Processed Ionogels for Thin-Film Lithium-Ion Electrolytes. *Joule* **2017**, *1* (2), 344–358. https://doi.org/10.1016/j.joule.2017.08.012.

(9) Ashby, D. S.; DeBlock, R. H.; Choi, C. S.; Sugimoto, W.; Dunn, B. Electrochemical and Spectroscopic Analysis of the Ionogel–Electrode Interface. *ACS Appl. Mater. Interfaces* **2019**, *11* (12), 12088–12097. https://doi.org/10.1021/acsami.9b00093.

(10) Augustyn, V.; Dunn, B. Vanadium Oxide Aerogels: Nanostructured Materials for Enhanced Energy Storage. *Comptes Rendus Chimie* **2010**, *13* (1–2), 130–141. https://doi.org/10.1016/j.crci.2009.05.002.

(11) Wei, Q.; DeBlock, R. H.; Butts, D. M.; Choi, C.; Dunn, B. Pseudocapacitive Vanadium-based Materials toward High-Rate Sodium-Ion Storage. *Energy & Environ Materials* **2020**, *3* (3), 221–234. https://doi.org/10.1002/eem2.12131.

(12) Brinker, J.C., S., G. W. *Sol-Gel Science: The Physics and Chemistry of Sol-Gel Processing*; Academic Press, Inc., 1990.

(13) Levy, D., Z., M. *The Sol-Gel Handbook: Synthesis, Characterization, and Applications*; Wiley-VCH: Weinheim, Germany, 2015.

(14) Sakamoto, J. S.; Dunn, B. Vanadium Oxide-Carbon Nanotube Composite Electrodes for Use in Secondary Lithium Batteries. *J. Electrochem. Soc.* **2002**, *149* (1), A26. https://doi.org/10.1149/1.1425791.

(15) Augustyn, V.; Come, J.; Lowe, M. A.; Kim, J. W.; Taberna, P.-L.; Tolbert, S. H.; Abruña, H. D.; Simon, P.; Dunn, B. High-Rate Electrochemical Energy Storage through Li+ Intercalation Pseudocapacitance. *Nature Mater* **2013**, *12* (6), 518–522. https://doi.org/10.1038/nmat3601.

(16) Dong, W.; Rolison, D. R.; Dunn, B. Electrochemical Properties of High Surface Area Vanadium Oxide Aerogels. **2000**, 4.

(17) Dong, W.; Sakamoto, J. S.; Dunn, B. Electrochemical Properties of Vanadium Oxide Aerogels. *Science and Technology of Advanced Materials* **2003**, *4* (1), 3–11. https://doi.org/10.1016/S1468-6996(03)00012-3.

(18) Livage, J. Optical and Electrical Properties of Vanadium Oxides Synthesized from Alkoxides. *Coordination Chemistry Reviews* **1999**, *190–192*, 391–403. https://doi.org/10.1016/S0010-8545(99)00096-X.

(19) Petkov, V.; Trikalitis, P. N.; Bozin, E. S.; Billinge, S. J. L.; Vogt, T.; Kanatzidis, M. G. Structure of $V_2O_5 \cdot nH_2O$ Xerogel Solved by the Atomic Pair Distribution Function Technique. *J. Am. Chem. Soc.* **2002**, *124* (34), 10157–10162. https://doi.org/10.1021/ja026143y.

(20) Liu, X.-Y.; Peng, H.-J.; Zhang, Q.; Huang, J.-Q.; Liu, X.-F.; Wang, L.; He, X.; Zhu, W.; Wei, F. Hierarchical Carbon Nanotube/Carbon Black Scaffolds as Short- and Long-Range Electron Pathways with Superior Li-Ion Storage Performance. *ACS Sustainable Chem. Eng.* **2014**, *2* (2), 200–206. https://doi.org/10.1021/sc400239u.

(21) Long, J. W.; Dunn, B.; Rolison, D. R.; White, H. S. 3D Architectures for Batteries and Electrodes. *Adv. Energy Mater.* **2020**, *10* (46), 2002457. https://doi.org/10.1002/aenm.202002457.

(22) Kim, D. H.; Oh, D. Y.; Park, K. H.; Choi, Y. E.; Nam, Y. J.; Lee, H. A.; Lee, S.-M.; Jung, Y. S. Infiltration of Solution-Processable Solid Electrolytes into Conventional Li-Ion-Battery Electrodes for All-Solid-State Li-Ion Batteries. *Nano Lett.* **2017**, *17* (5), 3013–3020. https://doi.org/10.1021/acs.nanolett.7b00330.

(23) Adany Putra Afauly, R.; Faiz Habibi, M.; Arief Budiman, B. Review on Manufacturing Methods of Functionally Graded Material of Solid-State Batteries. In *2021 3rd International Symposium on Material and Electrical Engineering Conference (ISMEE)*; IEEE: Bandung, Indonesia, 2021; pp 236–241. https://doi.org/10.1109/ISMEE54273.2021.9774272.

(24) Drummond, R.; Cheng, C.; Grant, P. S.; Duncan, S. R. Modelling the Impedance Response of Graded $LiFePO_4$ Cathodes for Li-Ion Batteries. *J. Electrochem. Soc.* **2022**, *169* (1), 010528. https://doi.org/10.1149/1945-7111/ac48c6.

(25) Dai, Y.; Srinivasan, V. On Graded Electrode Porosity as a Design Tool for Improving the Energy Density of Batteries. *J. Electrochem. Soc.* **2016**, *163* (3), A406–A416. https://doi.org/10.1149/2.0301603jes.

(26) Qi, Y.; Jang, T.; Ramadesigan, V.; Schwartz, D. T.; Subramanian, V. R. Is There a Benefit in Employing Graded Electrodes for Lithium-Ion Batteries? *J. Electrochem. Soc.* **2017**, *164* (13), A3196–A3207. https://doi.org/10.1149/2.1051713jes.

(27) Chaput, F.; Dunn, B.; Fuqua, P.; Salloux, K. Synthesis and Characterization of Vanadium Oxide Aerogels. *Journal of Non-Crystalline Solids* **1995**, *188* (1–2), 11–18. https://doi.org/10.1016/0022-3093(95)00026-7.

(28) Ghanbarian, B.; Hunt, A. G.; Ewing, R. P.; Sahimi, M. Tortuosity in Porous Media: A Critical Review. *Soil Science Society of America Journal* **2013**, *77* (5), 1461–1477. https://doi.org/10.2136/sssaj2012.0435.

(29) Chen-Wiegart, Y. K.; DeMike, R.; Erdonmez, C.; Thornton, K.; Barnett, S. A.; Wang, J. Tortuosity Characterization of 3D Microstructure at Nano-Scale for Energy Storage and Conversion Materials. *Journal of Power Sources* **2014**, *249*, 349–356. https://doi.org/10.1016/j.jpowsour.2013.10.026.

(30) Zhang, Y.; Malyi, O. I.; Tang, Y.; Wei, J.; Zhu, Z.; Xia, H.; Li, W.; Guo, J.; Zhou, X.; Chen, Z.; Persson, C.; Chen, X. Reducing the Charge Carrier Transport Barrier in Functionally Layer-Graded Electrodes. *Angew. Chem.* **2017**, *129* (47), 15043–15048. https://doi.org/10.1002/ange.201707883.

(31) Thorat, I. V.; Stephenson, D. E.; Zacharias, N. A.; Zaghib, K.; Harb, J. N.; Wheeler, D. R. Quantifying Tortuosity in Porous Li-Ion Battery Materials. *Journal of Power Sources* **2009**, *188* (2), 592–600. https://doi.org/10.1016/j.jpowsour.2008.12.032.

(32) Zacharias, N. A.; Nevers, D. R.; Skelton, C.; Knackstedt, K.; Stephenson, D. E.; Wheeler, D. R. Direct Measurements of Effective Ionic Transport in Porous Li-Ion Electrodes. *J. Electrochem. Soc.* **2013**, *160* (2), A306–A311. https://doi.org/10.1149/2.062302jes.

(33) Kehrwald, D.; Shearing, P. R.; Brandon, N. P.; Sinha, P. K.; Harris, S. J. Local Tortuosity Inhomogeneities in a Lithium Battery Composite Electrode. *J. Electrochem. Soc.* **2011**, *158* (12), A1393. https://doi.org/10.1149/2.079112jes.

(34) Nakashima, Y.; Kamiya, S. Mathematica Programs for the Analysis of Three-Dimensional Pore Connectivity and Anisotropic Tortuosity of Porous Rocks Using X-Ray Computed Tomography Image Data. *Journal of Nuclear Science and Technology* **2007**, *44* (9), 1233–1247. https://doi.org/10.1080/18811248.2007.9711367.

(35) Pouraghajan, F.; Knight, H.; Wray, M.; Mazzeo, B.; Subbaraman, R.; Christensen, J.; Wheeler, D. Quantifying Tortuosity of Porous Li-Ion Battery Electrodes: Comparing Polarization-Interrupt and Blocking-Electrolyte Methods. *J. Electrochem. Soc.* **2018**, *165* (11), A2644–A2653. https://doi.org/10.1149/2.0611811jes.

(36) Butts, D. M.; McNeil, P. E.; Marszewski, M.; Lan, E.; Galy, T.; Li, M.; Kang, J. S.; Ashby, D.; King, S.; Tolbert, S. H.; Hu, Y.; Pilon, L.; Dunn, B. S. Engineering Mesoporous Silica

for Superior Optical and Thermal Properties. *MRS Energy & Sustainability* **2020**, *7* (1), 39. https://doi.org/10.1557/mre.2020.40.

(37) McNeil, P.; Guillemin, T.; Fox, M.; Le Bideau, J.; Dunn, B. Characterization of Fragility in Silica-Based Ionogels. *J. Phys. Chem. C* **2022**, acs.jpcc.2c05911. https://doi.org/10.1021/acs.jpcc.2c05911.

(38) Livage, J. Vanadium Pentoxide Gels. *Chemistry of Materials* **1991**, *3*, 578–593.

(39) Grayli, S. V.; Leach, G. W.; Bahreyni, B. Sol-Gel Deposition and Characterization of Vanadium Pentoxide Thin Films with High TCR. *Sensors and Actuators A: Physical* **2018**, *279*, 630–637. https://doi.org/10.1016/j.sna.2018.07.002.

(40) Scherer, G. W. Aging and Drying of Gels. *Journal of Non-Crystalline Solids* **1988**, *100* (1–3), 77–92. https://doi.org/10.1016/0022-3093(88)90008-7.

(41) Katz, B.; Liu, W.; Salloux, K.; Chaput, F.; Dunn, B.; Farrington, G. C. MorphÒlogy and Properties of Vanadium Oxide Xerogels and Aerogels. *MRS Proc.* **1994**, *369*, 211. https://doi.org/10.1557/PROC-369-211.

(42) Li, L.; Li, R.; Huang, Z.; Yang, H.; Liu, M.; Xiang, J.; Hussain, S.; Shen, X.; Jing, M. A Multifunctional Gradient Solid Electrolyte Remarkably Improving Interface Compatibility and Ion Transport in Solid-State Lithium Battery. *ACS Appl. Mater. Interfaces* **2022**, *14* (27), 30786–30795. https://doi.org/10.1021/acsami.2c05578.

(43) Zhang, R.; Chen, B.; Ma, Y.; Li, Y.; Sha, J.; Ma, L.; Shi, C.; Zhao, N. Armoring Lithium Metal Anode with Soft–Rigid Gradient Interphase toward High-Capacity and Long-Life All-Solid-State Battery. *Green Energy & Environment* **2023**, S2468025723000304. https://doi.org/10.1016/j.gee.2023.02.006.

(44) Liu, F.; Cheng, Y.; Zuo, X.; Chen, R.; Zhang, J.; Mai, L.; Xu, L. Gradient Trilayer Solid-State Electrolyte with Excellent Interface Compatibility for High-Voltage Lithium Batteries. *Chemical Engineering Journal* **2022**, *441*, 136077. https://doi.org/10.1016/j.cej.2022.136077.

(45) Scherer, G. W. Theory of Drying. *J American Ceramic Society* **1990**, *73* (1), 3–14. https://doi.org/10.1111/j.1151-2916.1990.tb05082.x.

(46) Makkonen, L.; Kurkela, J. Another Look at the Interfacial Interaction Parameter. *Journal of Colloid and Interface Science* **2018**, *529*, 243–246. https://doi.org/10.1016/j.jcis.2018.06.015.

(47) Emmerling, A.; Fricke, J. Scaling Properties and Structure of Aerogels. *J Sol-Gel Sci Technol* **1997**, *8* (1–3), 781–788. https://doi.org/10.1007/BF02436938.

(48) Emmerling, A.; Fricke, J. Small Angle Scattering and the Structure of Aerogels. *Journal of Non-Crystalline Solids* **1992**, *145*, 113–120. https://doi.org/10.1016/S0022-3093(05)80439-9.

(49) Bard, A. J.; Faulkner, L. R.; White, H. S. *Electrochemical Methods: Fundamentals and Applications*, Third.; Wiley-VCH, 2022.

(50) Choi, C.; Ashby, D. S.; Butts, D. M.; DeBlock, R. H.; Wei, Q.; Lau, J.; Dunn, B. Achieving High Energy Density and High Power Density with Pseudocapacitive Materials. *Nat Rev Mater* **2020**, *5* (1), 5–19. https://doi.org/10.1038/s41578-019-0142-z.

(51) Dickinson, E. J. F.; Wain, A. J. The Butler-Volmer Equation in Electrochemical Theory: Origins, Value, and Practical Application. *Journal of Electroanalytical Chemistry* **2020**, *872*, 114145. https://doi.org/10.1016/j.jelechem.2020.114145.

(52) Liu, Y.; Xu, X.; Sadd, M.; Kapitanova, O. O.; Krivchenko, V. A.; Ban, J.; Wang, J.; Jiao, X.; Song, Z.; Song, J.; Xiong, S.; Matic, A. Insight into the Critical Role of Exchange Current Density on Electrodeposition Behavior of Lithium Metal. *Advanced Science* **2021**, *8* (5), 2003301. https://doi.org/10.1002/advs.202003301.

(53) Gao, J.; Shi, S.-Q.; Li, H. Brief Overview of Electrochemical Potential in Lithium Ion Batteries. *Chinese Phys. B* **2016**, *25* (1), 018210. https://doi.org/10.1088/1674-1056/25/1/018210.

Chapter 6. Conclusions

The projected continued growth of the Internet of Things and the miniaturization of consumer electronics have driven the development of current battery and micro-battery technology. While progress has been made in optimizing micro-power sources, specifically micro-batteries, there are limits to the improvements due to the constraints of the current device designs, specifically at the electrodes. The use of non-planar electrodes to create 3D batteries has shown improvements in energy and power density, however traditional microfabrication techniques are expensive and during device integration there are issues with aspects such as electrode alignment. To address these issues, the work here uses two different methods to create non-planar electrodes, alongside a solution processable pseudo-solid ionogel electrolyte to create 2.5D devices. With the 2.5D device, the one multidimensional electrode increases the electrode/electrolyte interface, and the planar electrode eliminates the need for an alignment step in device integration helping with ease of manufacturing.

Direct Ink Writing (DIW), a material accessible and affordable additive manufacturing process compared to other traditional microfabrication techniques, was used to develop a 3D lattice architecture. Here the role of architecture and loading of active material was studied by modifying various aspects of the lattice architecture such as lattice spacing, thickness, and aspect ratio. The results for both the half-cell arrangement and full 2.5D device show that although increasing geometric features such as areal enhancement factor are essential to the improvement of device metrics, there are limitations depending on the ink and its resolution of pitch spacing and achievable aspect ratio. The ability to identify architectural parameters that can be modified in order to achieve high areal capacities is important for improving upon current micro-batteries. A summary of electrochemical performances appears in Table 3.3. The electrode results are generally comparable to other multidimensional devices. The performance of these devices also establishes that using DIW in the fabrication of 3D battery designs with solid state architectures offers a promising direction for battery technology.

The next chapter more closely studied the building blocks that made up the larger lattice architectures to understand where there might be areas of higher resistance or improved conductivity. It was determined that with the DIW process, due to the thixotropic characteristics of the ink, having a constant flow of ink is important to achieve uniformity of the electrodes and leads to improvements with areal capacity, capacity retention and interfacial resistance. This is demonstrated by the results of the layer structure versus the other architectures, where the layer structure was the only one that used a continuous ink flow and spanned the allocated areal footprint. This point is especially significant when increasing height or aspect ratio of a printed architecture, that the layers should be connected. This will be a key area of consideration in optimizing not only the lattice design but for projects that want to utilize two multidimensional electrodes for a 3D micro-battery instead of the one for a 2.5D battery.

The other studied fabrication technique was the use of sol-gel processing to demonstrate a cathode of vanadium pentoxide ionogel. This is a vanadium pentoxide ambigel infiltrated with a conducting medium similar to the concept of a silica ionogel typically used as an electrolyte. Various parameters of the sol-gel process were modified, and the resulting gel structures were characterized to determine what the key conditions were to develop this aperiodic spongelike structure. Key results are reported in tables 5.1 and 5.2. A significant finding was that the infiltration of ionic liquid does not affect the electrochemical properties of the gel. The vanadium ionogels were used alongside a silica ionogel electrolyte to create a graded electrode/electrolyte interface and low resistances were measured across the interface. This work shows a promising development of using an ionically conductive porous network as an infiltrated cathode in a pseudo-solid state battery system. Further work should be continued on device development, optimization of the ionogel electrolyte and the stability of the vanadium ionogel pore structure.

The goal of this work was to show multiple avenues of fabrication to make multidimensional electrodes for improved micro-battery performance. The initial reported results in chapters 3 and 4 show comparable electrode performance to other multidimensional devices and the device integration leaves room for additional optimization to improve battery life. Chapter 5, shows the proof of concept for a graded electrode/electrolyte system with vanadium and silica ionogels. Being able to demonstrate even initial device integration is important for the future development of pseudo-solid battery systems. While the stated goal of this work was achieved, there is still future work that needs to be done to further optimize the energy and power density, especially for the vanadium system, and achieving appropriate device performance for integration with IoT technology.